PERFORMANCE EVALUATION OF A LOW ENERGY PULSED PLASMA THRUSTER

LEE HONG CHUN

FACULTY OF SCIENCE UNIVERSITI MALAYA KUALA LUMPUR

2024

PERFORMANCE EVALUATION OF A LOW ENERGY PULSED PLASMA THRUSTER

LEE HONG CHUN

THESIS SUBMITTED IN FULFILMENT OF THE REQUIREMENTS FOR THE DEGREE OF DOCTOR OF PHILOSOPHY

DEPARTMENT OF PHYSICS FACULTY OF SCIENCE UNIVERSITI MALAYA KUALA LUMPUR

2024

UNIVERSITI MALAYA ORIGINAL LITERARY WORK DECLARATION

Name of Candidate: LEE HONG CHUN

Matric No: 17050940

Name of Degree: DOCTOR OF PHILOSOPHY

Title of Thesis ("this Work"):

PERFORMANCE EVALUATION OF A LOW ENERGY PULSED PLASMA

THRUSTER

Field of Study:

PHYSICS

I do solemnly and sincerely declare that:

- (1) I am the sole author/writer of this Work;
- (2) This Work is original;
- (3) Any use of any work in which copyright exists was done by way of fair dealing and for permitted purposes and any excerpt or extract from, or reference to or reproduction of any copyright work has been disclosed expressly and sufficiently and the title of the Work and its authorship have been acknowledged in this Work;
- (4) I do not have any actual knowledge nor do I ought reasonably to know that the making of this work constitutes an infringement of any copyright work;
- (5) I hereby assign all and every rights in the copyright to this Work to the University of Malaya ("UM"), who henceforth shall be owner of the copyright in this Work and that any reproduction or use in any form or by any means whatsoever is prohibited without the written consent of UM having been first had and obtained;
- (6) I am fully aware that if in the course of making this Work I have infringed any copyright whether intentionally or otherwise, I may be subject to legal action or any other action as may be determined by UM.

Candidate's Signature

Date: 9/8/2024

Subscribed and solemnly declared before,

Witness's Signature

Date: 9/8/24

PERFORMANCE EVALUATION OF A LOW ENERGY PULSED PLASMA THRUSTER

ABSTRACT

Pulsed Plasma Thruster (PPT) is an established electric propulsion system with low cost and simple design. The research on PPT has grown a lot recently due to the demand and increasing interest in low cost and miniature sized satellites. In the PPT, plasma is produced through the surface breakdown of solid PTFE propellant, with the resulting selfinduced Lorentz force propelling the plasma to generate thrust. In this work, the performance of a side-fed, tongue-flared PPT operated at a range of lower discharge energy of 0.5 to 2.5 J has been investigated. The tongue-flared electrode geometry and side-fed polytetrafluoroethylene (PTFE) solid propellant configuration are used as these have been known to produce excellent thrust efficiency. The impulse bit (I_{bit}) , specific impulse (I_{sp}) , mass bit (m_{bit}) and thrust efficiency (η) are measured by a torsional thrust stand and these performance parameters are compared to those reported in other PPTs of similar range of discharge energy. Degradation of the solid PTFE propellant is evaluated from the Field Effect Scanning Electron Microscopy (FESEM) imaging and Energy Dispersive X-Ray (EDX) analysis of the PTFE bars after 10,000 discharges. It is found that at discharge energy around 2 J and above, the performance parameters are consistent with those in other PPT systems of similar configuration. Discrepancy observed at energies below 2 J is attributed to the low mass bit related to the discharge behaviour. Triple Langmuir probe is used to measure the spatial distribution of the plasma characteristics, such as electron temperature, T_e and electron density, n_e . These measurements were carried out up to 30 degrees angle from the centreline. The velocity of plasma ions was determined by calculating transit times from the point of initial surface

discharge on the PTFE surface to the probe locations. It showed non-symmetry behaviour in the perpendicular plane, this afforded us a better overall view on how the plasma plume expanded and could facilitate further model simulations of PPT. Comparison with other PPT systems which were operated at a wide range of energies validated this low energy PPT. The measured values of T_e and n_e were consistent with those reported for other PPTs within the same order of energy range.

Keywords: Pulsed plasma thruster, low discharge energy, performance parameters

PRESTASI PENDORONG PLASMA BERTENAGA RENDAH

ABSTRAK

Pemacu Plasma Denyutan (PPT) adalah sistem pemacuan elektrik yang telah mapan dengan kos rendah dan reka bentuk yang mudah. Kajian ke atas PPT telah berkembang pesat baru-baru ini disebabkan permintaan dan minat yang meningkat terhadap satelit bersaiz kecil dan kos rendah. Plasma dalam PPT dihasilkan dalam pemecahan permukaan propelan pepejal politetrafluoroethylene (PTFE); dan daya Lorentz yang dihasilkan sendiri mempercepatkan plasma untuk mencipta daya dorong. Dalam kajian ini, prestasi PPT berbentuk sisi, berlidah, dan berkelip digunakan pada julat tenaga pelepasan rendah 0.5 hingga 2.5 J telah disiasat. Geometri elektrod berlidah berkelip dan konfigurasi propelan pepejal PTFE berkelip digunakan kerana diketahui dapat menghasilkan kecekapan daya dorong yang sangat baik. Impulse bit (I_{bit}) , specific impulse (I_{sp}) , mass bit (m_{bit}) dan kecekapan tujahan (η) diukur oleh tunggul dorong torsi, dan parameter prestasi ini dibandingkan dengan PPT lain yang melibatkan julat tenaga pelepasan serupa. Penurunan propelan PTFE pepejal dinilai dari imej FESEM dan EDX pada palang PTFE selepas 10,000 pelepasan atau tembakan. Didapati bahawa pada tenaga pelepasan kirakira 2 J dan ke atas, parameter prestasi adalah konsisten dengan sistem PPT lain yang mempunyai konfigurasi serupa. Perbezaan yang diperhatikan pada tenaga di bawah 2 J dikaitkan dengan impuls jisim rendah berkaitan dengan tingkah laku pelepasan. Pengesan Langmuir digunakan untuk mengukur taburan spatial ciri-ciri plasma, iaitu suhu elektron, $T_{\rm e}$ dan kepadatan elektron, $n_{\rm e}$. Pengukuran ini dilakukan sehingga sudut 30 darjah dari garis pusat. Halaju ion diira dari masa perjalanan plasma dari sasaran PTFE di mana pelepasan permukaan pertama kali dimulakan ke kedudukan sonde. Ia menunjukkan tingkah laku bukan simetri dalam satah tegak lurus, ini memberikan pandangan

keseluruhan yang lebih baik tentang bagaimana awan plasma berkembang dan dapat memudahkan simulasi model lanjut bagi PPT. Perbandingan dengan sistem PPT lain yang beroperasi pada julat tenaga yang luas mengesahkan PPT tenaga rendah ini. Nilai-nilai yang diukur $T_{\rm e}$ dan $n_{\rm e}$ adalah konsisten dengan yang dilaporkan untuk PPT lain dalam julat tenaga yang sama.

Katakunci: pemacu plasma berdenyut, bertenaga rendah, ciri-ciri prestasi.

ACKNOWLEDGEMENT

Firstly, I want to express my sincere appreciation to Associate Professor Dr. Chin Oi Hoong, for her unwavering guidance and the invaluable opportunity to conduct my research at the low temperature plasma lab, University of Malaya. A special note of appreciation goes to her for forcing me to participate in the 3-Minute Thesis (3MT) competition that greatly enhanced my public speaking skills.

Next, I would like to express my heartfelt thanks to my supervisor Dr. Woo Haw Jiunn for the continuous encouragement and the thoughtful use of interesting metaphors and stories that have played an important role in reassuring me along my academic journey. I would also like to extend my gratitude to my supervisor Dr Goh Boon Tong for the generous provision of the vacuum pump and pressure meter, as well as for the invaluable assistance provided during the process of acquiring FESEM image and EDX data.

I also would like to express my deepest gratitude to my co-supervisor Mr Lim Chie Haw for imparting invaluable knowledge on high-voltage concepts and techniques. Our shared experiences in the lab, including the memorable times when we broke countless capacitors and electrical components have left an indelible mark on my learning journey.

Furthermore, I would like to express my sincere thanks to my fellow lab mates: the late Dr. Kanesh Jayapalan, Dr. Lau Yen Theng and Ms Raihaletchumy Anpalagan and final year project students. Their companionship has been an invaluable part of my journey in the laboratory. Whether engaged in thoughtful discussions about ongoing projects or deciding what to have for lunch. Their presence has made the lab environment warm and enjoyable.

Lastly, I would like to express my wholehearted thanks to my immediate family and cousins for their support throughout my academic journey. Their encouragement and understanding have been pillars of strength, enabling me to focus on my studies and pursue my goals with determination.

TABLE OF CONTENTS

ABS	STRAC	Т	iii
ABS	STRAK		V
ACI	KNOW	LEDGEMENT	vii
TAI	BLE OI	F CONTENTS	viii
LIS	T OF F	TIGURES	X
LIS	T OF T	TABLES	xvii
LIS	T OF S	YMBOLS AND ABBREVIATIONS	xviii
LIS	T OF	APPENDICES	XX
СН	APTER	2 1: INTRODUCTION	1
1.1	Introd	uction and motivations	1
1.2	Objec	tives	3
1.3	Thesis	outline	4
СН	APTER	2: LITERATURE REVIEWS	5
2.1	Gener	al Pulsed Plasma Thrusters (PPT) Overview	5
2.2	Work	ing principle of Pulsed Plasma Thrusters	8
	2.2.1	Pulsed Plasma Thruster discharge process	8
	2.2.2	Ablation of propellant	9
	2.2.3	Plasma propagation	10
	2.2.4	Late time ablation (LTA)	11
2.3	Thrust	dynamics and measurement	12
	2.3.1	Mass bit measurements	13
	2.3.2	Impulse bit measurements	13

2.4	Plasm	a properties and diagnostic	17
	2.4.1	Probe diagnostic	18
	2.4.2	Optical emission spectroscopy	20
2.5	Optin	nization of Pulsed Plasma Thrusters	22
	2.5.1	Electrode geometry	22
	2.5.2	Alternative propellant	25
		2.5.2.1 Polytetrafluoroethylene (PTFE) variation	25
		2.5.2.2 Solid chemical propellant	26
		2.5.2.3 Liquid propellant	27
	2.5.3	Electrical circuit optimization	28
2.6	Lifetir	me limiting factor of Pulsed Plasma Thrusters	30
	2.6.1	Carbonization issue.	30
	2.6.2	Spark plug system	31
2.7	Resea	rch development in Pulsed Plasma Thrusters	32
CH	APTER	R 3: EXPERIMENTAL METHOD	36
3.1	Design	n and fabrication of tongue-shape electrode plasma thruster system	36
	3.1.1	Pulsed Plasma Thrusters design	36
	3.1.2	Pulsed electronics system	39
	3.1.3	Vacuum system	47
3.2	Thrust	t measurement and plasma diagnostics	49
	3.2.1	Thrust measurement	49
	3.2.2	Discharge voltage-current measurement	58
	3.2.3	Triple Langmuir probe measurements	58
	3.2.4	Triple Langmuir probe cleaning	63

	3.2.5 Optical emission spectroscopy	64						
3.3	Surface erosion study	66						
CH	APTER 4: THRUST AND PROPULSION OF PPT	67						
4.1	Introduction							
4.2	Performance comparison of different capacitor	67						
4.3	Impulse characteristics	75						
	4.3.1 Impulse bit	75						
	4.3.2 Mass bit measurement	80						
	4.3.3 Specific impulse	82						
	4.3.4 Mean exhaust velocity	84						
	4.3.5 'Fastest' ion velocity	85						
	4.3.6 Thrust efficiency calculation	88						
4.4	Surface erosion and fuel consumption	90						
4.5	Comparison with other pulsed plasma thruster (PPTs)	94						
4.6	Summary	99						
CH	APTER 5: PLASMA CHARACTERIZATION OF PPT	100						
5.1	Introduction	100						
5.2	Electrical characteristic of Pulsed Plasma Thruster	100						
5.3	Plasma temperature and density	103						
	5.3.1 Electron temperature and density along the center axis	103						
	5.3.2 Radial profiles- Parallel plane	107						
	5.3.3 Radial profiles- Perpendicular plane	111						
5.4	Plasma species identifications	116						
5.5	Comparison to different plasma thruster	122						

5.6	Summary	123
CH	APTER 6: CONCLUSION	124
6.1	Conclusion	124
	6.1.1 Thrust and propulsion	124
	6.1.2 Plasma characterization	125
6.2	Suggestions for further work	126
REI	FERENCES	127
LIS	T OF PUBLICATIONS AND PAPER PRESENTED	135
LIS	T OF CONFERENCE PRESENTATIONS	135
LIS	T OF APPENDICES	136

LIST OF FIGURES

Figure 2.1	:	Schematic of the main processes that occur during plasma discharge of Pulsed Plasma Thruster.	8
Figure 2.2	:	Three main configurations for the pendulum thrust stand	14
Figure 2.3	:	Schematic of the (a) Triple Langmuir probe and (b) quadruple	19
Figure 2.4	:	Schematic diagram of (a) OES and (b) Faraday cup	21
Figure 2.5	:	Example of electrode configuration	24
Figure 2.6	:	Number of CubeSat launches for the last 25 years	32
Figure 3.1	:	Schematic diagram of the PPT system	36
Figure 3.2	:	(a) Diagram and (b) Photograph of electrode arrangement of a	36
		side-fed, tongue-flared plasma thruster	
Figure 3.3	:	Exterior and interior views of the PPT unit	38
Figure 3.4	:	Schematic diagram of charging and trigger circuit design for the PPT	39
Figure 3.5	:	Illustrations of the signal waveforms for the different components in the circuit	40
Figure 3.6	:	(a) Basic Astable 555 oscillator circuit, and (b) Improved Astable 555 oscillator circuit and their respective output pulses	41
Figure 3.7	:	Schematic diagram of the MOSFET push-pull circuit	43
Figure 3.8	:	Schematic diagram of voltage multiplier	43
Figure 3.9	:	PCB design for PPT system	44
Figure 3.10	:	Schematic of the improved design for the PCB	45
Figure 3.11	:	(a) Circuit diagram of capacitor charging controller using LT3750, and (b) the assembled circuit	46
Figure 3.12	:	Vacuum chamber and pump system for the experiment	48
Figure 3.13	:	(a) Schematic (top view) showing the response when a thrust is applied to one arm of the thrust stand, and (b) photograph of the torsional thrust stand system	49

Figure 3.14	:	Set up of magnetic damper	51
Figure 3.15	:	Anti-vibration mounts for the base plate	52
Figure 3.16	:	Schematic of torsional thrust stand for equation derivation of force and displacement measurement	52
Figure 3.17	:	Set up for the force calibration measurement	54
Figure 3.18	:	Graph of calibration of force measurement	55
Figure 3.19	:	Installation of permanent magnet on torsional thrust stand	55
Figure 3.20	:	Example of Fourier Transform used to evaluate the natural oscillation frequency	56
Figure 3.21	:	Electromagnetic calibration curve for impulsive force measurement	57
Figure 3.22	:	Actual setup for impulse bit measurement for the pulsed plasma thruster	57
Figure 3.23	:	Setup for voltage and current measurement	58
Figure 3.24	:	Diagram of electric potential of triple Langmuir probe	59
Figure 3.25	:	Typical V ₁₃ signal from the triple probe (a) unfiltered and (b) after noise filtering	61
Figure 3.26	:	The perpendicular plane with marked positions (black dots) where Langmuir probe measurements are made	62
Figure 3.27	:	The parallel plane with marked positions (black dots) where Langmuir probe measurements are made	62
Figure 3.28	:	Aluminium base plate with different drill holes	62
Figure 3.29	:	Setup of the plasma jet cleaning system	63
Figure 3.30	:	Condition of a probe tip before (left) and after (right) cleaning	64
Figure 4.1	:	Capacitor used in preliminary test	68
Figure 4.2	:	Electrical discharge voltage and current waveforms of ceramic capacitor	69
Figure 4.3	:	Discharge current against number of shots of ceramic capacitor	69
Figure 4.4	:	Electrical discharge voltage and current waveforms of polypropylene film capacitor (105J)	70

Figure 4.5	:	Discharge current against number of shots of polypropylene film capacitor (105J)	70
Figure 4.6	:	Electrical discharge voltage and current waveforms of polypropylene film capacitor (225J)	71
Figure 4.7	:	Discharge current against number of shots of polypropylene film capacitor (225J)	71
Figure 4.8	:	Electrical discharge voltage and current waveforms of KEMET capacitor	72
Figure 4.9	:	Discharge current against number of shots of KEMET capacitor	72
Figure 4.10	:	Impulse bit as a function of discharge energy. <i>I</i> _{bit} from similar flared electrodes, side fed PPTs (¹ Tran et al., ² Clark et al., ³ Ciaralli et al.) are included for comparison	77
Figure 4.11	:	Current parameter (ψ) as a function of discharge energy	78
Figure 4.12	:	Percentage of $I_{\text{bit-em}}$ to total I_{bit} as a function of discharge energy for two different values of L '. For comparison, data (hollow circles) from Ref. [¹Clark et al] are included	79
Figure 4.13	:	Mass bit (m_{bit}) as a function of (a) discharge energy and (b) charging voltage. Data from similar flared electrodes, side-fed PPTs (1 Tran et al., 2 Clark et al., 3 Ciaralli et al., 4Schönherr et al., 5Gessini & Paccani) are included for comparison	81
Figure 4.14	:	Specific impulse (I_{sp}) as a function of discharge energy/exposed area of propellant. Isp from flared electrodes, side-fed PPTs [1 Tran et al., 2 Clark et al., 3 Ciaralli et al] are included for comparison	83
Figure 4.15	:	Mean exhaust velocity (c_e) as a function of discharge energy determined from equations (4.5) and (4.6). [¹ Tran et al., ² Clark et al., ³ Ciaralli et al] are included for comparison	84
Figure 4.16	:	'Fastest' ion velocity at (a) different distance from PTFE surface, and (b) at different discharge energy	86
Figure 4.17	:	Thrust efficiency η of PPT for discharge energy from 0.5 to 2.5 J. η from similar PPTs of flared electrodes, side-fed propellants are included for comparison. [¹Tran et al., ²Clark et al., ³Ciaralli et al] are included for comparison	89

Figure 4.18 :		Discharge-induced surface erosion on the PTFE propellant bar after 1,000 shots fired at (a) 0.5 J, (b) 2.5 J, and (c) Placement of the propellant bar (only the right side is drawn) with respect to the electrodes				
Figure 4.19	:	FESEM image of PTFE propellant surface at different regions after 1000 shots fired at 0.5 J and 2.5 J. The respective eroded and charred regions for 2.5 J are marked as (1) and (2), while (3) marks the charred region for 0.5 J	91			
Figure 4.20	:	FESEM EDX spectra measured at the sampled regions (a) '1' and (b) '2' and (c) '3' of Figure 4.19	91			
Figure 4.21		Figure 4.21: FESEM image of PTFE propellant surface at the boundary between the charred and eroded areas	93			
Figure 4.22 : Plots of (a) Impulse bit, (b) specific impulse, and (c) thrusefficiency with respect to discharge energies for the PPTs in Table 4.2			96			
Figure 5.1	:	(a) Discharge voltage measured across the electrodes, and (b) discharge current for different discharge energies. Inset shows plot of current maximum (first current peak) versus the square root of discharge energy	100			
Figure 5.2	:	Images of PPT discharge	102			
Figure 5.3	:	Time-varying electron temperature, $T_{\rm e}$ measured at different points along the center axis (angle = 0°) for discharge energy of 0.5 and 2.5 J	103			
Figure 5.4	:	Time-varying electron temperature, n_e measured at different points along the center axis (angle = 0°) for discharge energy of 0.5 and 2.5 J	104			
Figure 5.5	:	Peak electron temperatures as a function of distance (center axis) from the PTFE surface at discharge energy of $0.5 - 2.5 \text{ J}$.	105			
Figure 5.6	:	Peak electron density as a function of distance (center axis) from the PTFE surface at discharge energy of $0.5-2.5\mathrm{J}$	105			
Figure 5.7	:	(a) Parallel plane measurement of peak electron temperature, T_e and (b) peak electron density, n_e at various distance from angle -30° to 30° for 0.5 J	108			
Figure 5.8	:	(a) Parallel plane measurement of peak electron temperature, T_e and (b) peak electron density, n_e at various distance from angle -30° to 30° for 1.5 J	109			

Figure 5.9	:	(a) Parallel plane measurement of peak electron temperature, T_e and (b) peak electron density, n_e at various distance from angle -30° to 30° for 2.5 J	110
Figure 5.10	:	(a) Perpendicular plane measurement of peak electron temperature, T_e and (b) peak electron density, n_e at various distance from angle -20° to 20° for 0.5 J	112
Figure 5.11	:	(a) Perpendicular plane measurement of peak electron temperature, T_e and (b) peak electron density, n_e at various distance from angle -20° to 20° for 1.5 J	113
Figure 5.12	:	(a) Perpendicular plane measurement of peak electron temperature, T_e and (b) peak electron density, n_e at various distance from angle -20° to 20° for 2.5 J	115
Figure 5.13	:	Setup of OES system	116
Figure 5.14	:	Emission spectral of plasma at discharge energy at (a) 0.5 J, and (b) 2.5 J	116
Figure 5.15	:	Voigt fit for C II 426.7nm line	119
Figure 5.16	:	Boltzmann plot for C II lines at discharge energy of 0.5 – 2.5 J.	120
Figure 5.17	:	Electron temperature, T_e as a function of discharge energy	121

LIST OF TABLES

Table 2.1	:	Performance parameters of selected electric propulsion flight systems	6
Table 2.2	:	Comparison of performances of various propellants	28
Table 2.3	:	A list of several PPT developed	34
Table 3.1	:	PPT parameters	37
Table 4.1	:	Results comparison between capacitors for preliminary test	73
Table 4.2	:	Known source of error for uncertainty analysis	75
Table 4.3	:	Comparison of the performance parameters of various PPTs. n/s means not stated	95
Table 5.1	:	C II spectral lines and the parameters	118
Table 5.3	:	Comparison with other Pulsed Plasma Thrusters (PPTs)	123

LIST OF SYMBOLS AND ABBREVIATIONS

 A_p : cross section area of the probe

 $A_{\rm mn}$: transition probability from the upper state m to the lower state n

B : magnetic field strength

 $\Delta \bar{L}(x)$: mean change in inductance

e : electron charge

 ε_0 : permittivity of free space

 E_0 : discharge energy

 E_m : energy of upper state

 $f_{\rm nat}$: natural frequency of the torsional thrust stand

 g_0 : acceleration due to gravity, 9.81 m/s^2

 $g_{\rm m}$: degeneracy of the upper state

 $I_{\rm bit}$: impulse bit

 I_{bitem} : impulse bit (electromagnetism)

 I_{i} : current collected by the probe (i=1,2,3)

 $I_{\rm mn}$: relative intensity

 $I_{\rm sp}$: specific impulse

 λ_{D} : Debye wavelength

 λ_{mn} : wavelength

k : Boltzmann constant

L' inductance variation per unit length of electrode

 m_e : mass of electron

 m_{bit} : mass bit

 n_e : electron density

 η : thrust efficiency

N : total number density

 ψ : current parameter

 r_p : radius of the Langmuir probe

 T_e : electron temperature

 μ_0 : permeability of vacuum

 V_i : voltage of the probe(i=1,2,3)

 V_f : floating potential

 V_s : space potential

 V_{12} : Potential difference between probe 1 and 2

 V_{13} : Potential difference between probe 1 and 3

Z : Partition function

EDX : Energy Dispersive X-ray

ESL : Equivalent series inductance

ESP : Electric solid propellant

ESR : Equivalent series resistance

ETFE : Ethylene tetrafluoroethylene

FESEM : Field effect scanning electron microscope

HAN : Hydroxyl-ammonium-nitrate

HTPM-AP : Hydroxyl-terminated polybutadiene-Ammonium perchlorate

LTA : Late time ablation

OES : Optical emission spectroscopy

PPT : Pulsed Plasma Thruster

PFPF : Perfluoropolyether

PTFE : Polytetrafluoroethylene

LIST OF APPENDICES

Appendix A	:	LT3750 datasheet	13	6
Appendix B	:	KEMET capacitor datasheet	13	8

CHAPTER 1: INTRODUCTION

1.1 Introduction and motivations

Research on space exploration is recently a hot topic since NASA confirmed the discovery of seven Earth-like planets which are 40 light years away from us. Therefore, there arises the need for more and more satellites and spacecrafts need to be sent to carry out space exploration; and hence suitable propulsion system is also required for these systems. Other than the conventional chemical propulsion system, electric propulsion system is an alternative and promising candidate due to its long lifetime and large impulse (total change of momentum) over the chemical propulsion system. Thus, different types of electric propulsion had been invented. Pulsed Plasma Thruster (PPT) device is one of the popular electric thrusters still being studied since the first PPT invented in 1964 by researchers in the Soviet Union. This is because PPT has a robust and low-cost design while providing a high specific impulse. One of the well-known applications using PPT is the CubeSats, a $10 \times 10 \times 10$ cm³ miniaturized satellite. By using the PPT, a precise and controllable thrust can be performed and thus, it can be used in satellite for altitude controlling purpose. Though it is an established system in use, the low efficiency of the PPT remains a significant challenge requiring attention.

Pulsed Plasma Thrusters (PPT) have gained significant attention as a propulsion technology for small spacecraft, particularly the CubeSats. Most of the CubeSats currently in orbit do not have a propulsion system. With a proper propulsion system, it can extend the satellite's mission time in space, assist with space debris avoidance manoeuvres, coordinate constellation orbits, and facilitate a timely and controlled re-entry at the end of the mission. These compact satellites require efficient and reliable propulsion systems that can operate at low energy levels. There is an abundance of research focusing on plasma characteristics of PPT at high energy ranges exceeding 20 J. But as the size of

satellites is scaled down, it is necessary to study the performance of PPT at the lower energy range (2 J and below) and determine its consistency and reliability.

The increasing interest in CubeSats as cost-effective platforms for various space missions has prompted the need for low-energy PPT that can provide reliable propulsion. To address the challenges associated with working at low energy levels, this research work aims to design and develop a PPT system. By mitigating this problem, the accurate characterization of plasma properties becomes feasible, leading to a deeper understanding of the low-energy PPT's behaviour and performance.

1.2 Objectives

In this work, dependence of the performance of PPT on the electrical discharge energy (or storage energy in the capacitor) in the low range of 0.5 to 2.5 J is studied. The tongue-flared electrode geometry and side-fed PTFE solid propellant are used as these have been known to produce excellent thrust efficiency. The impulse bit (I_{bit}), specific impulse (I_{sp}), mass bit (m_{bit}) and thrust efficiency (η) are measured by a torsional thrust stand and the performance is compared to other PPTs of similar range of discharge energy. Degradation of the solid PTFE propellant is evaluated from the Field Effect Scanning Electron Microscopy (FESEM) imaging and Energy Dispersive X-Ray (EDX) analysis of the PTFE bars after 1,000 discharges or shots.

The objectives of the research work are:

- 1. To develop Pulsed Plasma Thruster featuring a side-fed, tongue-flared electrode configuration that operates at low energy.
- 2. To characterize the Thrust, Propulsion, Impulse Characteristics, and Ablation/Charring patterns of the PTFE propellant surface.
- 3. To evaluate key plasma characteristics of the PPT including temperature, density, and species identification.

1.3 Thesis outline

This thesis is divided into six chapters. The previous sections of this chapter have introduced the research topic, along with the motivations and objectives. Chapter 2 contains the general overview of PPT, optimization of PPT and the research and development in PPT. Chapter 3 covers the methodology with detailed description of the experimental setup of the pulsed plasma thruster system. Diagnostic methods and the characterization technique employed in studying surface erosion also included in this chapter. The results are presented and discussed in Chapters 4 and 5. Chapter 4 covers discussion of the impulse characteristics of pulsed plasma thruster, such as impulse bit (I_{bit}), specific impulse (I_{sp}), mass bit (m_{bit}), and thrust efficiency (η). Surface erosion and fuel consumption related to PTFE also discussed in this chapter. The thruster performance of this PPT is compared with findings from others published research. Chapter 5 discusses about the electrical characteristics of PPT and includes data on electron temperature (T_e) and density (n_e), which were obtained using a triple Langmuir probe. The results obtained in Chapters 4 and 5 are summarized and concluded in Chapter 6.

CHAPTER 2: LITERATURE REVIEW

2.1 General Pulsed Plasma Thrusters (PPT) overview

The Pulsed Plasma Thruster (PPT) first made its debut in space travel aboard the Zond-2 Russian spacecraft back in 1964. Since then, it has found applications on numerous spacecraft such as the *LES-6* satellite, *Earth Observertion 1* satellite (*EO-1*) and *Dawgstar*. The renewed emphasis on low-cost propulsion systems for the next generation of satellites and the development of CubeSat concept made researchers regain focus and interest on PPT.

The advantages of PPT are simple, robust, small, low power consumed, with decent Specific impulse (I_{sp}) and low impulse bit (I_{bit}). Specific impulse (I_{sp}) is a measure of propellant utilisation and signifies how much impulse is produced divided by the (propellant) weight that the spacecraft spends. The higher the specific impulse, the less mass needs to be expelled to produce a given amount of thrust, so the less massive the spacecraft must be.

However, as shown in the table 2.1 (Scharlemann et al, 2003), the specific impulse of PPT is not as high compared to other propulsion systems such as the Hall and ion thrusters. But the input power of PPT is the smallest. It shows that PPT is suitable for small satellite where the power supply is not sufficiently large for other types of thrusters. While the low I_{bit} means there is only little change in momentum per pulse, it is perfect for fine and precise control. Larger order of motion is achievable by adjusting the frequency of the pulses.

Table 2.1: Performance parameters of selected electric propulsion flight systems

Concept	Specific impulse (s)	Input power (kW)	Thrust/power ratio (mN/kW)	Specific mass (kg/kW)	Propellent
Dosistaiat	269	0.5	743	1.6	N_2H_4
Resistojet	299	0.9	905	1	N_2H_4
	480	0.85	135	3.5	NH ₃
Amaint	502	1.8	138	2.5	N_2H_4
Arcjet	>580	2.17	113	2.5	N_2H_4
	800	26	N/A	N/A	NH_3
PPT	847	< 0.03	20.8	195	PTFE
PFI	1200	< 0.02	16.1	85	PTFE
	1600	1.5	55	7	Xenon
Hall	1638	1.4	N/A	N/A	Xenon
	2042	4.5	55.4	6	Xenon
	2585	0.5	35.7	23.6	Xenon
	2906	0.74	37.3	22	Xenon
Ion	3250	0.6	30	25	Xenon
	3280	2.5	41	9.1	Xenon
	3400	0.6	25.7	23.7	Xenon

The PTFE used as a solid propellant in PPT is non-toxic and retains its solid form at low pressure. Therefore, it does not need any complex gas feeding system. It can retain the simplicity of PPT. These characteristics make PPT suitable for tasks such as attitude control, station-keeping, orbit raising or insertion, orbit control, and end-of-life deorbiting manoeuvres for satellites.

The nanosatellite revolution has been steadily gaining momentum over the years. Introducing the CubeSat concept has played a pivotal role in making nanosatellite production more affordable and accessible. A CubeSat is a satellite measuring 10cm × 10cm × 10cm, referred to as a '1 Unit' CubeSat or '1U'. CubeSats can vary in size, denoted by the number of units, such as 2U, 4U, 6U, and so forth. This standardized CubeSat

framework allows research institutions to concentrate on developing individual modules, knowing that these modules, if adhering to the standard, can be widely utilized, marketed, and integrated into various CubeSat missions. The standardized of CubeSats also contributes to lower hardware costs compared to traditional commercial satellites. With a proper propulsion system, CubeSats deployed in low Earth orbits (LEO) possess the capability to counter atmospheric drag, thus effectively extending their lifespan in space. One common challenge faced by satellite mission is the risk of collisions with space debris. Additionally, CubeSat thrusters capable of delivering precise impulse bits offer an alternative solution for attitude control, serving as viable substitutes for reaction wheels and magnetorquers.

One of the biggest challenges in designing a propulsion system for CubeSat is the restricted power availability from the small photo-voltaic panels and the limited battery capacity and limited space available on-board the spacecraft. Thrusters that required a big propellant tank size such as cold gas and chemical thruster are not suitable due to limit in mass and volume. PPT is one of the suitable candidates for CubeSat propulsion because of its lower limit in mass, volume, and power. Furthermore, PPT does not contain any highly pressurized tanks and pyrotechnics. It will reduce potential risks to the launch vehicle. Moreover, the ability of PPT to actively change the orbit of the CubeSat fulfils the new legislation that required that satellite re-entry into atmosphere, to reduce the total amount of space debris that orbit around the Earth.

2.2 Working principle of Pulsed Plasma Thruster

2.2.1 Pulsed Plasma Thruster discharge process

In summary, a pulsed plasma thruster consists of power supply unit, capacitor that act as energy storage device, a pair of electrodes and the solid propellant PTFE positioned between the electrodes. The discharge process is described in figure 2.1. Firstly, the power supply unit charge up the capacitor to the desired voltage, up to few kilovolts. Once the capacitors were fully charged, it is ready to be discharged. A sparkplug is used to initiate a main discharge between the electrode by electron avalanche through the surface layers (Figure 2.1 (a)). The energy provided by the spark plug is much smaller than the energy stored in capacitors. After the discharge is initiated, a discharge current of few kilo amperes begins to flow between the electrodes through the surface of the solid propellant PTFE. (figure 2.1 (b)). This large discharge current induced a strong magnetic field around the electrode.

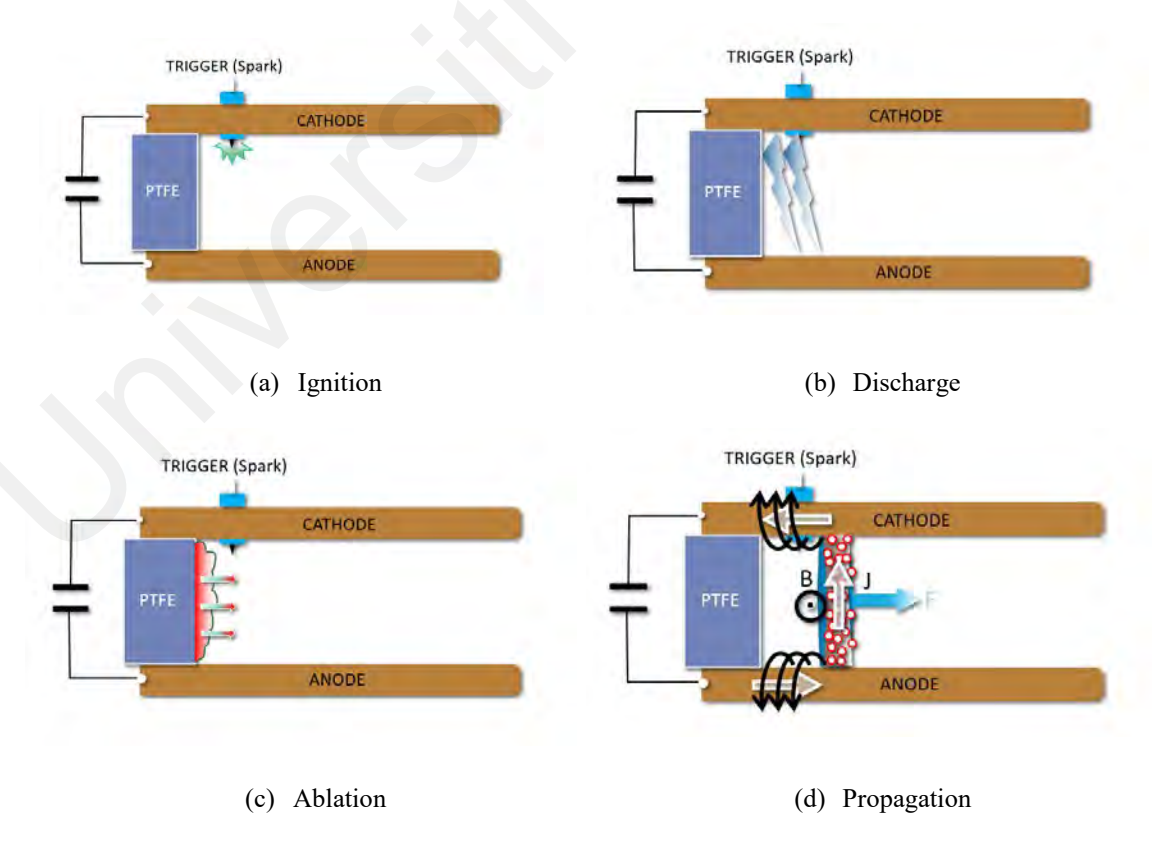


Figure 2.1: Schematic diagram of the main processes that occur during plasma discharge of Pulsed Plasma Thruster.

As the energy stored in capacitors is converted into electrical energy and to form the magnetic field, the potential difference between the electrode drops to zero. However, the current will continue to flow because the electrode act like inductor that will resist the change in the flow of current. This current is driven by the magnetic field and will charge the capacitor with a voltage of opposite polarity. The current will stop when the magnetic field is diminished. The capacitor is now charged again, and the cycle begins again, but the current now flowing in opposite directions. The energy oscillates back and forth between the capacitor, current and magnetic fields and eventually dies out. Hence, a typical discharge voltage graph will show an underdamped oscillation pattern. By changing the shape and size of electrode (flaring angle, aspect ratio), it will have an impact on the performance of PPT because it affects the inductance and the formation of magnetic fields.

2.2.2 Ablation of propellant

Figure 2.1 (c) shows the ablation process. This is an important process as it affects the mass bit and hence affect the performance of the PPT. The discharge process previously described causes the ablation of propellant, where the solid propellant undergoes sublimation before ionization, leading to plasma formation. Berkeley & Choueiri (2013) shows that the distribution of current across the electrode is not linear, maximum current density is found near the cathode. This is evidenced by the erosion of the PTFE propellant bar, indicating greater erosion of PTFE propellant near the cathode area. The higher the discharge energy, more propellant will be eroded. This relationship has been demonstrated in numerous experiments, where the erosion of PTFE mass was directly correlated with the applied discharge energy. Research indicates that electrodes undergo erosion during discharge as well. The presence of a non-zero trend line, as observed in the work of Koizumi et al. (2003), suggests the generation of impulse bit even in the

absence of propellant. Keidar et al. (2004) introduced a model for ablation comprising three layers: the Knudsen layer, the Hydrodynamic layer, and the plasma bulk layer. The Knudsen layer, being only a few mean free paths thick, is characterized by kinetic nonequilibrium. In contrast, the Hydrodynamic layer is dominated by collisions and lacks equilibrium. The outermost layer, the plasma bulk layer, assumes thermal equilibrium among ions, electrons, and neutral particles. This model can be used to estimate the ablation rate of PPT, provided that the surface temperature of PTFE, the density and temperature in the plasma can be obtained in the research. Gatsonis et al. (2007) determine the mathematical relationships that governing the PTFE ablation, and these relationships are implemented numerically using an innovative non-uniform grid with adaptation and explicit finite-difference techniques. Yang et al. (2010) utilized an electromechanical model to analyse parallel PPTs. Their study involved the development of an idealized, quasi-steady analytical model incorporating the ablation process. This model could predict the impact of various electrical parameters such as discharge voltage, circuit resistance, and electron temperature on ablation mass. Yang et al. (2016) proposed a modified model capable of demonstrating how thermochemical reactions influence the ablation properties of PPTs.

2.2.3 Plasma propagation

When current passes through the electrodes, it generates magnetic fields. The interaction between the current flow through the plasma and these magnetic fields produces the Lorentz force. This force, perpendicular to both the magnetic field and the current flow, accelerates the plasma along and out of the discharge chamber. High-speed photography conducted by Nawaz et al. (2007) demonstrates a significant canting of the plasma plume from the cathode towards the anode. The ablated PTFE moves perpendicular to the propellant surface, propelled by the Lorentz force. Another process

involves a force originating from the cathode and directed towards the anode. The combination of this force with the Lorentz force may contribute to the canting of the plasma plume. Neutral particles are also generated during the discharge process; however, they are not accelerated by the Lorentz force and therefore move at significantly slower speeds. This phenomenon is demonstrated in the work of Koizumi et al. (2007), utilizing high-speed photography and magnetic field measurements. Their findings reveal that only a portion of the gas ablated by the discharge engages in plasma formation and electromagnetic acceleration. This suggests that only a minor fraction of the mass ablated during a discharge pulse contributes to electromagnetic acceleration. Neutral particles extract energy from high-velocity ions through collisions, resulting in inefficiencies in propellant utilization.

2.2.4 Late time ablation (LTA)

After the plasma discharge process is finished and the capacitor's energy is fully drained, subsequent processes take place. Only a fraction of the total discharged energy is utilized for accelerating ion particles. Some energy dissipates as radiation and heat during the discharge. Some of the heat energy lost is transferred to the surface of the PTFE propellant. If the energy is significant enough, it induces a phase transition on PTFE, causing the propellant surface to sublimate, resulting in the formation of small and large particles. These neutral particles are propelled out of the discharge chamber by gaseous pressure forces at a velocity ranging from 200 to 300 meters per second. Solbes & Vondra (1973) were the first to identify the LTA phenomenon. They utilized an interferometer system alongside a broadband high-speed imaging system to detect neutral particles emitted from the PPT. Their observations revealed that the vaporization of PTFE persisted for a minimum of 300 µs, attributed to the surface temperature higher than the PTFE sublimation temperature. In 2001, Keidar et al. examined the charring of the PTFE

surface in a micro-PPT. Their analysis led to the conclusion that the charred region primarily consisted of carbon, formed due to carbon flux returning from the plasma rather than incomplete decomposition of PTFE. In 2007, Montag et al. (2007) demonstrated through experimentation the feasibility of preventing charring by designing an ablation area featuring a high specific energy. Li & Royer (2019) uses second stage electrode to accelerate the LTA particles and hence increase the thrust. Given that the late time ablation is widely acknowledged as a primary cause to propellant utilization inefficiencies in PPT, minimizing and fully study the LTA effect will lead to a substantial enhancement in efficiency.

2.3 Thrust dynamics and measurement

The impulse bit (I_{bit}), specific impulse (I_{sp}), and thrust efficiency (η) are key parameters for characterizing the performance of a PPTs. I_{bit} is the impulse produced by a single firing of the thruster. A high I_{bit} is usually an important selection criterion for PPTs but in some applications, it requires small change in momentum to pinpoint the location of satellite to sub-millimeter, then the minimum impulse bit capability can be a deciding factor. On the other hand, I_{sp} is a measure of propellant utilization, and it is determined by how much impulse is produced per unit of ablated mass of propellant. A higher specific impulse means less mass of propellant being expelled to produce a given amount of thrust. The thrust efficiency (η) is calculated from the conversion of the electrical energy stored in capacitor into the kinetic energy.

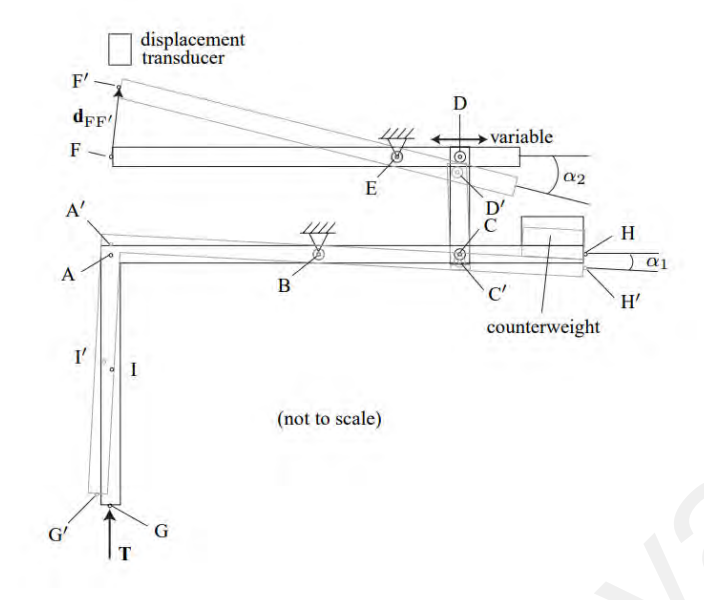
2.3.1 Mass bit measurements (mbit)

Mass bit is the mass of propellant consumed or ablated in single firing of the thruster. It represents the amount of propellant material that is ablated due to the plasma discharges.

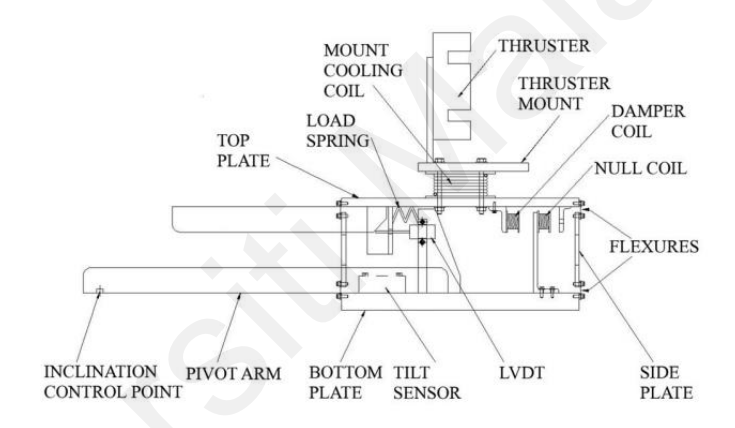
mbit is a critical parameter in evaluating the performance and efficiency of PPT, it is needed in the calculation of specific impulse and thrust efficiency. The determination of mass bits in Pulsed Plasma Thrusters (PPTs) involves using an electronic balance, and the measurements are typically averaged over many discharges due to the extremely small magnitude of mass loss due to single discharge.
mbit is usually expressed in milligrams (mg) or micrograms (μg). In the discharge PPT, the propellant undergoes processes of ablation, ionization, and acceleration by Lorentz's force. Subsequently, the carbon back flux effect will cause the carbon to be deposited back to the PTFE surface. To obtain an accurate measurement of mbit, an electronic balance with high resolution, typically ranging between 0.01–0.001 mg, is utilized. This precision allows for the precise determination of mass loss after a significant large number of shots, typically ranging from 100 to 1000 discharges.

2.3.2 Impulse bit measurements

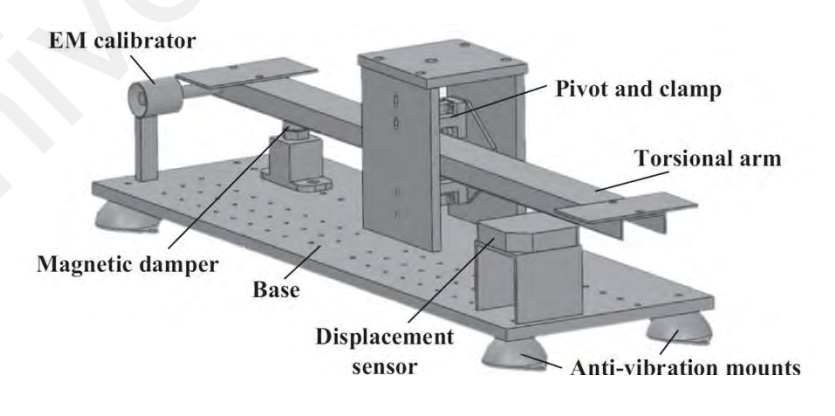
Impulse bit refers to the momentum transferred to a satellite through a single firing of the thruster. It is a key performance parameter for Pulsed Plasma Thrusters (PPTs). PPT generate very small low impulse bit, usually in the order of micronewton seconds. The precise measurement of these forces requires the use of highly sensitive measuring device such as a pendulum thrust stand, it essentially operates as a mass-spring-damper system. In this setup, a structure that holds the thruster is attached to a torsional spring. As forces are applied, the structure undergoes oscillation. Through the analysis of these oscillations, it is possible to determine the impulse bit produced by the thruster.



a) hanging



b) inverted



c) torsional

Figure 2.2: Three main configurations for the pendulum thrust stand. (a Moeller et al, b Xu et al., c Lam et al.)

There are three main configurations for the pendulum thrust stand: hanging, inverted, and torsional as shown in Figure 2.2. Each configuration has its own set of advantages and limitations. The choice of configuration depends on the specific requirements of the experiment or evaluation being conducted. In all these cases, the application of thrust stand results in a displacement which is a function of the impulse bit. The displacement is commonly measured with a laser interferometer or a linear differential voltage transformer (LDVT). Beiting (1999) utilized a pendulum to measure the thrust of a MEMS propulsion system. This approach allowed for the precise assessment of the thrust generated by the MEMS device during its operation. Wilson et al. (1997) designed a compact pendulum with the aim of achieving a longer periodic oscillation time. This modification was intended to measure the average thrust when an PPT is operated in repetitive mode, involving consecutive periodic discharges. The extended oscillation time provided a more accurate means of capturing the average thrust over multiple discharges. Emhoff et al. (2007) introduced a unique method by presented an innovative approach involving the design of a metal flexure that reacts to thruster ignition. The impulse bit could then be derived from the vibrational displacement of this flexure. This approach offered an alternative way to measure impulse bit by capturing the thruster's impact on a flexure. In recent developments, Hicks et al. (2013) employed a levitated stand to measure micro-newton-level thrust. This innovative method involves suspending the measurement apparatus, reducing frictional effects, and allowing for highly sensitive thrust measurements. While various approaches have been explored, a torsional thrust, as demonstrated by researchers like Haag (1997), Gamero (2003), and Koizumi et al. (2004), has been identified as one of the most effective methods for measuring the impulse bit of a PPT. Torsional thrust stands provide a robust and reliable means of capturing the thrust produced by the thruster during operation.

To ensure the data obtained from thrust stands is accurate, a calibration method is required. Tang et al (2011) introduced an electromagnetic calibration technique, which proved effective in achieving precise non-contact calibration for a torsional thrust stand. They used a permanent magnet setup to generate a consistent magnetic field. Adjustments to the electromagnetic calibration force for pulsed thrust measurements were made by varying the coil current. The amount of attraction or repulsion force produced is used to calibrate the thrust stand.

An alternative method for measuring the impulse bit involves the utilization of a piezo pressure probe. A pressure probe is a high-speed instrument engineered to capture the axial distribution of the total pressure within the plasma plume generated by the thruster. The primary focus is on the integrated total pressure value, which essentially reflects the kinetic energy output of the PPT during a single discharge cycle. Given the extremely short discharge time of the PPT, typically around 10 microseconds, it is necessary that the pressure probe's response time is sufficiently fast to capture the actual signal produced during the discharge. The rapid response requirement, coupled with the transient nature of the PPT's operation, makes it demanding to design and implement pressure probes with the necessary sensitivity and speed. Scharlemann & York (2006) conducted measurements within the brief and highly turbulent plume of a PPT.

2.4 Plasma properties and diagnostic

The study of PPT plume characteristics primarily revolves around the plasma discharge and its expansion from the propellant surface. The plasma generated includes neutral particles and ions, primarily produced from the ablation process of PTFE solid propellant, and some material from electrode erosion. Plasma diagnostics employed for analysing plumes generally categorize into two main categories: contact and non-contact measurement techniques. These methodologies serve to explore and characterize the properties and behaviour of the plasma in propulsion systems.

Contact measurements involve the use of probes placed directly into the plasma plume to gather details of plasma. Examples of such probes include a Faraday cup, Langmuir probe (refer to figure 2.3 (b)), and retarding potential analyser. These tools can acquire data on plasma parameters such as electron density, electron temperature, ion energy distribution, and electron energy distribution function.

Non-contact measurements include techniques like optical emission spectroscopy (figure 2.4 (a)), interferometry, and electromagnetic induction methods. Emission spectroscopy and interferometric methods are optical approaches utilizing emission and excitation wavelengths to analyse the plasma plume. Electromagnetic induction methods are grounded in the alternating current-induced electromotive potential of an PPT and are employed to acquire local current density, as seen in tools like magnetic probes or Rogowski coils.

2.4.1 Probe diagnostic

Among the various methods for diagnosing plasma plumes, the utilization of a Langmuir probe stands out as one of the simplest and most direct approaches for determining crucial plasma parameters like electron temperature (T_e), electron density (n_e). However, conventional single Langmuir probes are typically used with stationary plasmas. In order to gather measurements, it is necessary to apply a swept voltage to obtain current–voltage characteristic curves. For PPT, the transient nature of their plasma plumes demands nearly instantaneous signal capture, making a single Langmuir probe less suitable. To address this challenge, Chen & Sekiguchi (1965) introduced a triple Langmuir probe method that doesn't rely on a steady-state plasma plume or the acquisition of a scanned current–voltage characteristic curve. This innovative method allows for the calculation of instantaneous T_e and n_e of the plasma plume in a very short time, typically less than 1 microsecond. As a result, it is highly suitable for the plume diagnostics of PPT.

The triple Langmuir probe method has been extensively employed for plasma diagnostics in PPT. In a series of experiments conducted by Eckman et al. (2001), he focused on measuring electron temperature and density within the plume of an PPT, exploring various downstream distances, different angles (10°–45°) with respect to the center of the PTFE surface, different measurement planes (parallel and perpendicular) and various energy levels (5, 20, and 40 J). The results indicated that the electron temperature ranged from 2 to 4.5 eV for all discharge energies, while the electron density varied from approximately 10¹⁹ to 10²¹ m⁻³, transitioning from low to high discharge energy (5–40 J). The measurements with a large polar divergence angle (10°–45°) confirmed the non-symmetric nature of the PPT plume, carrying significant implications for spacecraft plume interaction studies.

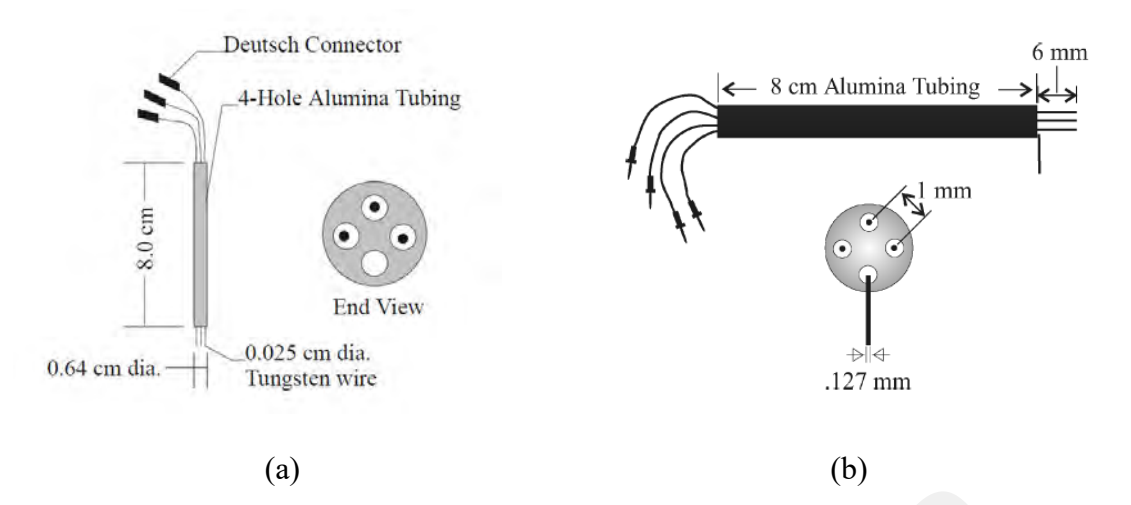


Figure 2.3: Schematic of the (a) triple Langmuir probe (Eckman et al.) and (b) quadruple Langmuir probe (Gatsonis et al.)

Zhang et al. (2011) also conducted plasma plume measurements using 4 J and 20 J PPTs. Analysis of the temporal profiles of electron temperature and density unveiled 3–4 peaks, suggesting the existence of various ion species exhibiting distinct velocities.

Gatsonis et al. (2004) achieved success in measuring plasma plume parameters using a current-mode quadruple Langmuir probe. This probe enabled the determination of T_e , n_e , and the ratio of ion speed to the most probable thermal speed. The measurements encompassed a broad expanse of the plasma plume, spanning from 10 to 20 cm downstream of the propellant surface and covering angular positions ranging from 0° to 40° off the centerline on planes perpendicular and parallel to the thruster's electrodes. It was determined that electrons with temperatures reaching up to 18 eV were detected at the peak current of the discharge. The estimated speeds of ions at different distances along the centerline decreased throughout the pulse, suggesting an unsteady acceleration mechanism within the PPT channel.

In 2017, the plasma plume characteristics of a solid propellant PPT were investigated using a triple Langmuir probe by Glascock et al. (2017). The study revealed a plume consisting of weakly ionized gas with high-temperature electrons, low-temperature ions,

and neutrals, indicating that the acceleration mechanism is dominated by electrothermal energy. Despite having a stored energy of 40 J, thermal inefficiency was identified for the electric solid propellant relative to PTFE plasma plumes.

2.4.2 Optical emission spectroscopy (OES)

Optical emission spectroscopy (figure 2.4 (a)) plays a vital role in diagnosing and measuring plasma parameters. This spectroscopic diagnostic method is non-contact, ensuring minimal interference with the plasma. Optical Emission Spectroscopy (OES) stands out as one of the frequently utilized plasma diagnostic methods for PPT. The plasma spectrum is intricately linked to the radiative transition process occurring within the plasma particles. When atoms or ions undergo thermal or electrical excitation, the outer electrons acquire a specific amount of energy. Subsequently, these electrons undergo a transition from a lower energy level to a higher one, placing the atom or ion in an excited state. An excited state is inherently unstable, prompting the particle to transition back to a ground state or a relatively stable, lower energy level. During this transition, excess energy is released in the form of light, giving rise to an emission spectrum. The emitted light, characterized by different wavelengths, constitutes spectral lines unique to the particles undergoing transitions between distinct energy levels. By analysing the wavelength information of these spectral lines allows for the extraction of valuable characteristics about the plasma.

Thomassen & Vondra (1972) used OES and faraday cups (figure 2.4 (b)) to measure plasma parameters. They found that around 90% of the plasma plume is neutral particles. Markusic et al. (1997) discover that no new ions species are formed even though they increase the discharge energy. Koizumi et al. (2007) used emission spectroscopy to perform plasma diagnosis on the discharge channel of PPT, they conclude that ablated neutral gas stayed near the surface of the propellant, only a fraction of it is transformed

into plasma and accelerated by electromagnetic force. In 2013, Schönherr et al. used emission spectroscopy to analyse the changes in the plasma characteristics of the discharge channel of PPT over time, space, and discharge energy. It is found that the electron temperature is between 1.7-3.1 eV, and it is not uniform and asymmetric across the discharge channel. Ling et al. (2019) used emission spectroscopy to study the plasma parameters of asymmetric PPT with different anode length.

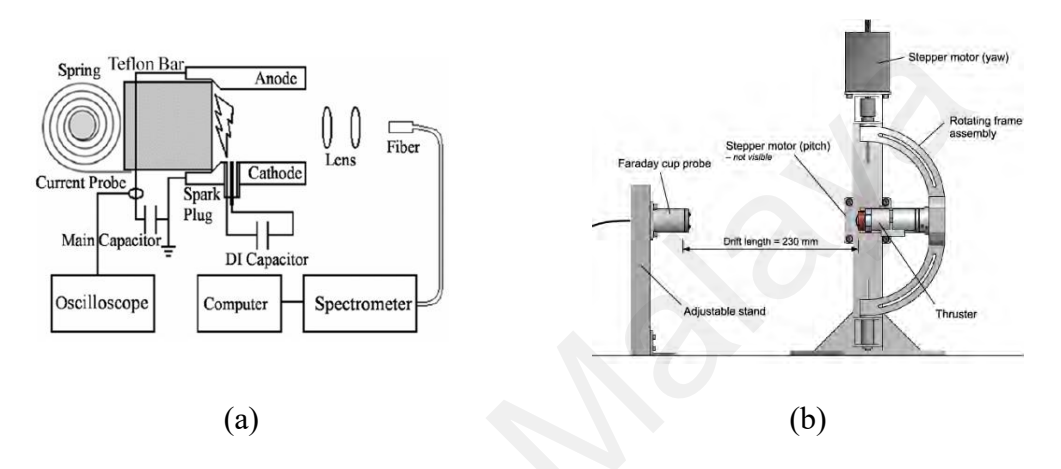


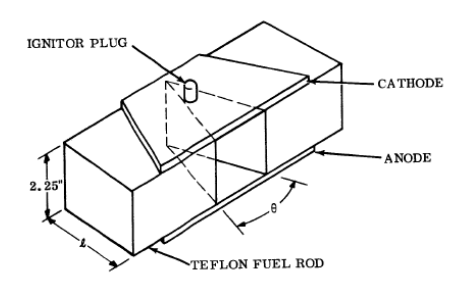
Figure 2.4: Schematic diagram of (a) OES (Wang et al.) and (b) Faraday cup (Lun et al.)

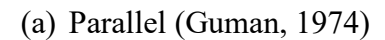
2.5 Optimization of Pulsed Plasma Thrusters

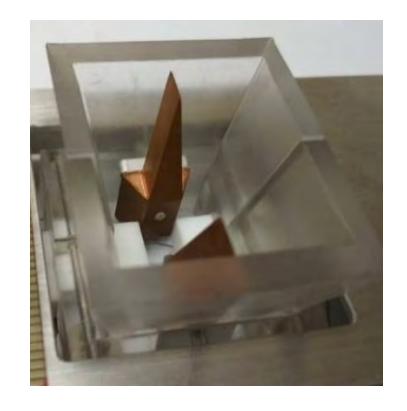
Considering the optimization of thruster design and its associated performance is crucial. Extensive research has been conducted on enhancing the performance of PPTs through adjustments in parameters like thruster geometry, propellant choice, and electrical circuitry.

2.5.1 Electrode geometry

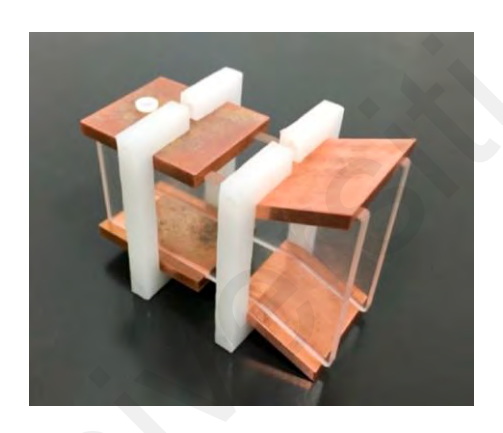
Parameters such as the flaring angle of the electrode, spacing between electrodes, and width ratio of the electrode are crucial factors that significantly impact the performance of Pulsed Plasma Thrusters (PPTs). Adjusting these parameters can influence the efficiency, thrust, and overall effectiveness of the propulsion system. Researchers often explore and optimize these parameters to enhance the PPT's performance for specific mission requirements. Palumbo & Guman (1976) found that optimum flare angle for electrode is 20°, they also found that decreasing the spacing of electrode resulted in more oscillatory discharge and hence reduce the efficiency. Various electrode configurations have been tested for PPT, including the traditional parallel plate electrode (Figure 2.5 (a)), coaxial electrode (figure 2.5 (b)), tongue-flared electrode (Figure 2.5 (c)), Z-pinch adaptation, dual stage electrode and segmented electrode. In terms of thrust efficiency, Antropov et al. (2003) reported an up to 10% increase when using a tongue-shaped electrode compared to a rectangular electrode. In the work conducted by Coletti et al. (2009), a two-stage Pulsed Plasma Thruster was developed as a solution to address the late-time ablation issue. The approach involved triggering a secondary discharge after the main discharge to accelerate the propellant ablated during the late stages, thereby increasing the overall efficiency of the PPT up to 60% compared to single stage PPT. Li & Royer (2019) (figure 2.5 (e)) employed a secondary electrode stage to enhance the acceleration of late-time ablation particles (LTA) by contributing a second burst of energy from a second capacitor to increase thrust efficiency. The exhaust velocity exhibited a significant increase in comparison to that of the single-stage PPT. Additionally, Schönherr et al. (2009) achieved an increase in impulse bit and thrust efficiency by 35% by incorporating a flare angle of 20° for the tongue-shaped electrode. Zhang et al. (2018) introduced an asymmetric electrode configuration with a segmented anode (figure 2.5 (f)). Their study demonstrated that the segmented anode PPT resulted in an improvement in impulse bit of up to 28% when compared with conventional symmetric PPTs. Furthermore, the thrust efficiency was enhanced by 49%. This suggests that the proposed asymmetric electrode configuration can lead to significant performance improvements in PPT systems.



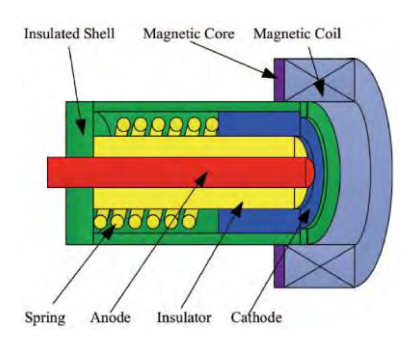




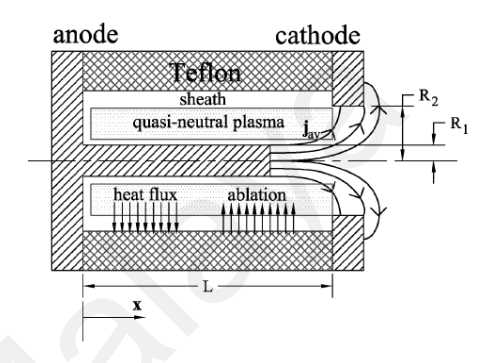
(c) Tongue-flared (Lee et al, 2021)



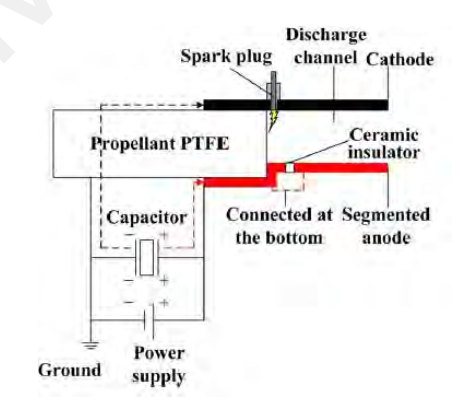
(e) Second stage (Li & Royer, 2019)



(b) Coaxial (Keidar et al, 2004)



(d) Z-pinch (Markusic et al, 2005)



(f) Segmented (Zhang et al, 2017)

Figure 2.5: Example of different electrode configuration

2.5.2 Alternative propellant

Many PPTs commonly utilize Polytetrafluoroethylene (PTFE) as a solid propellant due to its simplicity, robustness, high reliability, and adaptability for scaling down to smaller dimensions. However, PTFE has its drawbacks, such as the charring effect, where layers of carbon deposition on the PTFE surface may result in short circuits and reduce the lifespan of the thruster. Additionally, the late-time ablation effect can lead to a decrease in propellant utilization efficiency (Spanjers et al., 1998). To enhance the performance and characteristics of PPTs, various alternative propellants have been explored. Numerous research studies have investigated a wide range of gaseous, liquid, and solid propellants to improve PPT behaviour and efficiency.

2.5.2.1 Polytetrafluoroethylene (PTFE) variations

Given the advanced research status of PTFE in comparison to other propellants, numerous previous studies have explored the composition of PTFE propellant with various other materials. For examples, As an illustration, Palumbo & Guman (1976) mixed PTFE with 10%–30% of LiOH and InBr. The peak current was noted to decrease with an increase in the number of discharges. This is due to the deposition of a high-resistance compound on the electrodes, leading to decreases in efficiency. The impregnation of PTFE with 2% carbon by weight was examined by NASA Glenn Research Center (Kamhawi et al., 2002). The specific impulse increased by 75%, and efficiency doubled. However, the presence of increased carbon deposition between the electrodes makes it unsuitable for miniaturized PPT, as it leads to a reduction in the thruster's lifetime. Leiweke et al. (1995) explored PTFE propellant laminated with High-Density Polyethylene (HDPE) to achieve an overall weight less than pure PTFE. The study revealed a 26% increase in impulse bit with a similar specific impulse, but the issue of carbon coverage was observed. Ou et al (2019) blended PTFE with Si, Al and Al₂O₃,

resulting in an increase in specific impulse (2675s) and improved efficiency (11.15%). Nevertheless, these additives led to a decrease in plasma density, causing the plasma plume to slow down. Additionally, these fillings were found to deposit on the surface, potentially compromising the long-term performance of the system. Operating at low discharge energy levels tends to decrease the mass bit while enhancing specific impulse and efficiency. However, as the discharge energy increases, the mass bit also increases, leading to a deterioration in the overall performance of the system.

2.5.2.2 Solid chemical propellant

Hydroxyl-Terminated Polybutadiene-Ammonium Perchlorate (HTPB-AP)-based propellant was subjected to testing at Kyushu Institute of Technology in Japan (Hideto et al., 2006). This solid chemical propellant demonstrated an impulse bit increase of over 10% compared to PTFE, accompanied by a lower mass bit, consequently boosting thrust efficiency. The introduction of aluminium further enhanced the specific impulse by approximately 80% and doubled the overall efficiency. Zhou et al. (2017) conducted tests using HTPB and observed that the mass bit was half that of PTFE. In terms of plasma parameters, HTPB exhibited a lower electron temperature but twice the electron density, indicating a distinct ablation mechanism compared to PTFE.

Electric Solid Propellant (ESP) is an energetic material based on Hydroxyl-Ammonium-Nitrate (HAN), presenting itself as an alternative candidate to replace PTFE. ESP undergoes exothermic decomposition upon ignition and ceases when the power is removed. However, studies (Glascock et al, 2019) indicate inconsistent impulse bit production, varying from pulse to pulse. The primary acceleration mechanism is predominantly electrothermal, with a mass bit approximately one order higher than PTFE, while the electron temperature and density are lower than those of PTFE.

Palumbo & Guman (1976) examination of ethylene tetrafluoroethylene (ETFE) as an alternative fuel revealed that the specific impulse was 60% higher than that of PTFE. However, the thrust-to-power ratio was not comparable to PTFE in their experiments. Tahara et al. (2007) investigated ethylene tetrafluoroethylene (ETFE) at 15 J of discharge energy, revealing that the specific impulse and efficiency were significantly higher than those achieved with PTFE. Another alternative to PTFE that has been investigated is sulphur. The thrust produced is few times higher than PTFE but with slower plasma velocity (Northway et al., 2017).

2.5.2.3 Liquid propellant

Liquid propellants have also undergone examination for use in PPT primarily motivated by addressing challenges related to low propellant utilization, late-time ablation, and carbon charring effect. Several liquid propellants have been studied, including Perfluoropolyether (PFPE). PFPE is non-hazardous, chemically stable, and exhibits very low vapor pressure. It has almost negligible evaporation in vacuum at temperatures of up to 100 to 150 °C. This characteristic eliminates the need for a pressurization tank, making it feasible to scale down Pulsed Plasma Thrusters (PPT). In their study, Zhang et al. (2022) utilized Perfluoropolyether (PFPE) impregnated into a porous ceramic with various pore diameters as a propellant. A comparison with PTFE revealed that the PFPE-based propellant exhibited a higher mass bit and impulse bit. However, it demonstrated a lower specific impulse and efficiency. The findings presented by Ling et al. (2017) indicate that liquid Perfluoropolyether (PFPE) displayed no carbon deposition, this confirmation suggests that the utilization of liquid PFPE as a propellant eliminates one of the major failure issues in PPT.

The most suitable propellant for a Pulsed Plasma Thruster (PPT) system will depend on the specific mission requirements, each having its own set of advantages and disadvantages. Table 2 provides a list of some of the propellants discussed in this context. In this work, PTFE was chosen as the propellant due to its simplicity and ability to produce a decent impulse. Future studies will focus on alternative propellants to study the effect of propellant on the lifetime of PPT.

Table 2.2: Comparison of performances of various propellants

Propellant	Discharge energy (J)	Specific impulse (s)	Thrust efficiency (%)
PTFE	10	200	2.5
PTFE with 2% C	10	375	4.54
PFPE	1.05	N -O	-
ETFE	14.6	570	17.2
HTPB-AP	20	460	2.2
HTPB-AP/Al	5	1200	20
ESP	40	200	-
Sulphur	20	1200	25

2.5.3 Electrical circuit optimization

The electrical setup of PPTs can be conceptually represented as an LCR (inductor-capacitor-resistor) circuit, a simplification that has proven effective in previous studies for analyzing their electrical characteristics (Guman & Williams 1974). However, these simplifications lead to a disconnection between modelled trends and actual data, thereby reducing the practical utility of such models. The inductance and resistance of a PPT fluctuate over time due to the time-varying properties of the plasma component within the circuit. The discharge in a PPT typically displays a sinusoidal waveform with oscillations, characteristic of an underdamped LCR response. However, when assessing the practical application of an PPT, these current reversals and consequent fluctuations in capacitor voltage can strain the capacitor, thereby shortening its operational lifespan. The

oscillating pattern observed in a PPT discharge arises from impedance mismatching between the LCR circuit and the PPT, indicating that the efficiency of electrical energy transfer is low. As noted by Burton & Turchi (1998), employing a pulse-forming network can address this impedance mismatching issue with the PPT, although it's typically implemented for energy levels in the range of several hundred joules. However, for micro propulsion applications where power levels typically range in the order of several joules, pulse-forming networks are ineffective due to parasitic inductances. Hence, alternative approaches are necessary for achieving efficient energy transfer at lower power levels. Turchi et al. (1996) introduced a novel strategy to overcome the difficulties in achieving the pulse-forming network. This approach, termed the two-step energy transfer process, involves a sequential sequence of actions. Following the reversal of the discharge, a secondary ignition of a second PPT within the same circuit is triggered. This secondary ignition serves the purpose of limiting the reverse direction recharge of the capacitor. Another technique to eliminate the occurrence of an oscillating waveform involves the incorporation of diodes within the discharge circuit to inhibit current reversal. Kimura et al. (1978) implemented this method by adding two solid-state diodes into the discharge circuit of a 6-J PPT, positioning it in parallel with the capacitor. Nevertheless, the incorporation of diodes brings about a trade-off, resulting in a reduction of both mass bit and impulse bit by approximately 10%. While these methods enhance the lifetime of capacitor, they do so at the cost of other aspects such as the efficiency of the thruster. Improving capacitor design and matching impedance are crucial for enhancing PPT circuitry in the future. Tackling these issues is vital for maximizing performance and lifespan of pulsed plasma thrusters.

2.6 Lifetime limiting factor in Pulsed Plasma Thrusters

The carbonization of the discharge chamber often cited as the primary mechanism limiting the lifespan of PPT. The deposition of a carbon layer on the walls of the discharge chamber or the propellant surface, forming a conducting path between the electrodes. Eventually, this can lead to electrode shorting, resulting in permanent thruster failure. Carbonization occurs as the plasma plume generated by the main discharge expands, impacting the inner surfaces of the discharge chamber and depositing carbon ablated from the PTFE propellant bars. Furthermore, optimizing the spark plug system is another significant concern for enhancing PPT longevity and propulsion system reliability. The spark plug must demonstrate reliability throughout the PPT's operational life, as a failure in the ignition system could prove catastrophic for the entire propulsion system.

2.6.1 Carbonization issue

Carbonization poses a significant challenge in the operation of PPTs. The formation of carbon, induced by high temperatures during discharge, alters the composition of the propellant surface. Compared to pure Polytetrafluoroethylene (PTFE), the evaporation and ionization of a carbonized surface demand considerably more energy, thus complicating the generation of a discharge event. In Takegahara et al.'s study (2001), carbonization was noted, leading to thruster failure after approximately 110,000 discharge pulses. However, by reducing the discharge area from 5 cm² to 0.5 cm² and increasing the energy density from 0.5 J/cm² to 7.2 J/cm², the carbonization issues were resolved. In 2011, a side fed PPT, (PPTCUP), was developed at the University of Southampton (Guarducci et al., 2011). This thruster experienced significant carbon deposition on the discharge chamber walls after just 1000 shots. It is asserted that the chosen energy level and energy-to-propellant-area ratio of 2.13 J/cm² should ensure that the thruster remains unaffected by severe carbonization of the propellant and discharge chamber walls. These

studies suggest that increasing the initial energy and the energy-to-propellant-area ratio reduces the effect of the carbonization.

2.6.2 Spark plug system

The spark plug holds a pivotal role within a PPT as it initiates the main discharge. Reducing the breakdown voltage of the spark plug, ideally to a level equal to or lower than that of the main capacitor bank's charging voltage, offers several advantages, including:

- Decreased overvoltage on the capacitor bank during the trigger discharge,
 potentially lowering the risk of failures or damage to individual capacitors.
- Simplified and more reliable control electronics, wherein a single high-voltage power supply can charge the main capacitor bank and trigger the discharge.
- Enhanced overall reliability of the propulsion system, essential for extending its operational lifetime.

The most common technique for reducing the breakdown voltage and improving spark plug performance is to apply a thin layer of a different material onto the insulator. This approach may include depositing a semiconductor layer, as demonstrated by Brady & Aston (1983), or applying a metal coating, as shown by Anders et al. (1998) and Keidar et al. (2006). This strategy is substantiated by the successful utilization of metal-coated spark plug insulators in other miniaturized thrusters, which have demonstrated durability, enduring over one million shots.

2.7 Research and development in Pulsed Plasma Thrusters

In the initial stages of space technology evolution, government institutions predominantly spearheaded the endeavours. However, there has been a noticeable transition towards increased participation from commercial operators and, in some cases, universities. For example, SpaceX unveiled ambitious plans for a satellite Internet service named "Starlink." The company aimed to launch approximately 12,000 microsatellites by 2020, envisioning a global network that provides cost-effective Internet connectivity. This initiative underscores the growing influence of commercial entities in shaping the trajectory of space technology.

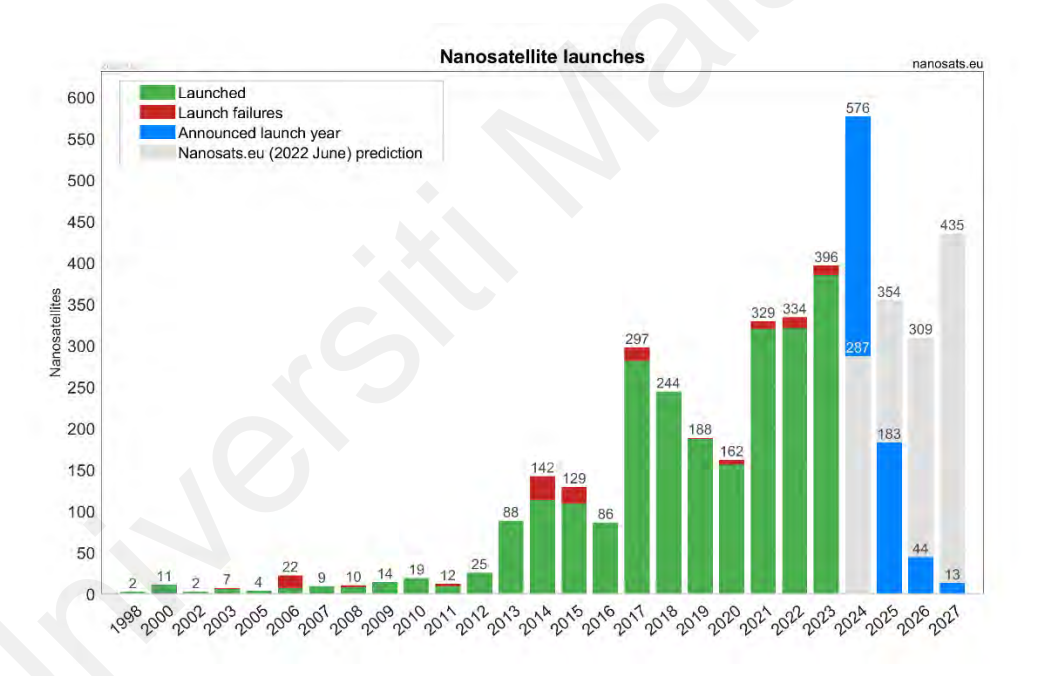


Figure 2.6: Number of CubeSat launches for the last 25 years. (Photo sourced from https://www.nanosats.eu/)

As shown in Figure 2.6, there is an increasing trend in the number of CubeSat launches each year. There has been a significant surge in the number of CubeSat launches, jumping from 25 in 2022 to an impressive 583 this year. Based on these trends, it's very likely that CubeSats will replace traditional satellite missions in Earth observation, telecommunications, and astronomy (Cappelletti & Robson, 2021). ExoCube, launched

in 2015, is a 3U CubeSat designed to characterize the densities of different elements and ions in the Earth's exosphere and ionosphere (Jones et al., 2015). Another example is ANGELS, a 12U CubeSat launched in 2019, which tracks beacons attached to animals, ships, and weather buoys. In the field of telecommunications, ISARA, a 3U cube launched by JPL (Poghosyan & Golkar, 2017), demonstrated the feasibility of a foldable Ka-band reflect array antenna concept, which could greatly enhance downlink bandwidth for small satellites. In the field of astronomy, typically the large space agency will operating the large satellite (Hubble, JWST) focus on one target type only (distant galaxies, black holes, exoplanets). CubeSats provide an opportunity to allow individuals or groups to dedicate their own spacecraft for a specific target at much lower cost. ASTERIA, a 6U CubeSat launched by NASA was the first CubeSat that to observe a transiting ExoPlanet—55 Cancri e (Smith et al., 2018). CubeSat missions are not confined to low Earth orbit (LEO). They can also serve in deep space missions or provide support for future manned missions to other planets. However, a challenge is that miniature propulsion systems may require a longer duration to reach their destination. Fortunately, CubeSats can leverage rideshare opportunities on interplanetary missions by being accommodated as secondary payloads onto launchers through standardized deployers. For example, MarCO, a 6U CubeSat launched by NASA, transmitted crucial Entry, Descent, and Landing (EDL) data to Earth in near real-time when the lander or other orbiters, like MRO, were unable to do so (Freeman, 2020). Another example is the Artemis I, NASA's Lunar Exploration mission, where thirteen 6U CubeSats were deployed with a focus on studying the Moon.

Table 2.3: A list of several PPT developed.

Electrode Configuration	Energy (J)	Impulse bit, I _{bit} (µNs)	Specific Impulse, I _{sp} (s)	Massbit, m _{bit} (μg)	Efficiency (%)	Work by
Tongue-flared parallel electrode	1.8	31	590	4.8	5	Clark etal.
Tongue-flared parallel electrode	2	38	608	6.4	5.8	PPTCUP
Tongue-flared parallel electrode	2.5	25.3	676	3.8	3.3	AOBA VELOX- IV
Tongue-flared parallel electrode	16.7	420	1300	16	32	ADD-SIMP- LEX
Coaxial	2	80	830	9.83	16	FalconSat-3
Coaxial	2.43	108	740	23.4	26	PROITERES1
Coaxial	2.5	4.4	904	-	-	Pegasus
Coaxial	3	20	536	-		BMP-220
Parallel electrode	1.85	27	300	-	2	LES-6
Parallel electrode	2.25	29.5	300	10	2	ETS-IV
Parallel electrode	2.37	16.5	927	1.78	3.2	TMIT
Parallel electrode	2.6	40	608	-	4.9	LPPT-5
Parallel electrode	4	63	280	25	2	An et al.
Parallel electrode	4.2	25	800	13	2.3	STSAT-2
Parallel electrode	4.9	66	266	25.4	1.8	Dawgstar
Parallel electrode	5	40	450	-	-	AX-III
Parallel electrode	6.6	112	613	-	5.6	LPPT-25
Parallel electrode	8	88	530	17	3	APPT-8
Parallel electrode	8.4	122	405	-	3.7	SMS
Parallel electrode	8.5 56	90 860	650 1400	-	8	EO-1
Parallel electrode	20	378	540	-	5.4	NOVA-1
Parallel electrode	20	298	1000	30	7.4	LES 8/9
Parallel electrode	20	375	850	45	7.6	TIP-II
Parallel electrode	20	500	1140	44.7	14	APPT-20
Parallel electrode	27.3	943	525	183	9	Sharif UT-PPT-1

Table 2.3 shows a list of PPTs developed. Detailed comparison and discussion with this work will be carried out in chapter 4.4. Traditionally, satellites weighed several thousand kilograms. However, there has been a remarkable shift, and it is now feasible to manufacture satellites weighing less than 100 kg, and even as minimal as the 1-kg range. This shift toward miniaturization in the satellite industry holds significant implications for cost-effectiveness, accessibility, and the diversification of space missions. To facilitate the miniaturization of technology, as well as the downsizing of satellites, there is an urgent and vital need for new, more efficient, and long-serving thrusters specifically designed for small satellites.

CHAPTER 3: EXPERIMENTAL METHOD

This chapter is divided into three parts. Part I describes the experimental setup of the pulsed plasma thruster system while the diagnostic methods are described in Part II. Part III describes the characterization technique employed in studying surface erosion.

3.1 Design and fabrication of the Pulsed Plasma Thruster (PPT) system

3.1.1 Pulsed Plasma Thrusters design

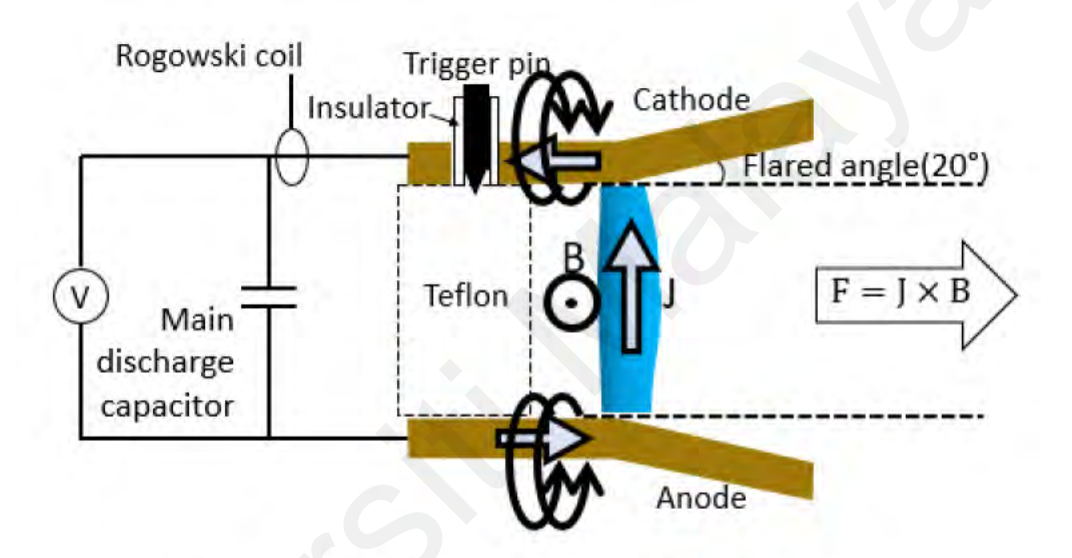


Figure 3.1: Schematic diagram of the PPT system

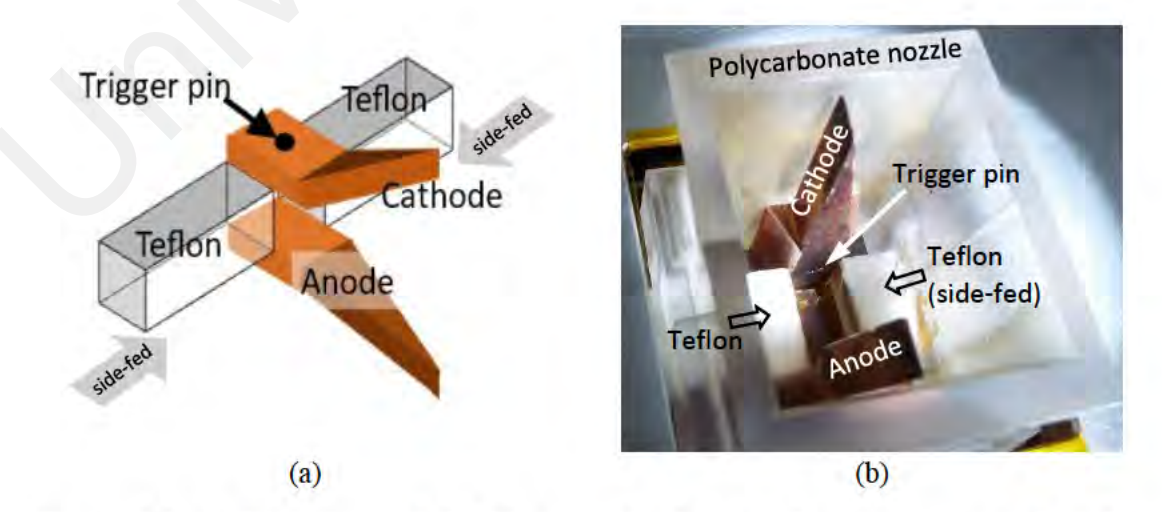


Figure 3.2: (a) Diagram and (b) Photograph of electrode arrangement of a sidefed, tongue-flared plasma thruster.

Table 3.1: PPT parameters

Parameters	Value
Discharge energy (J)	0.5-2.5
Charging voltage (kV)	1.05-2.31
Trigger voltage (kV)	15
Capacitance of main capacitor (µF)	0.94
Electrode gap distance (mm) (at the narrowest part)	10
Electrode width (mm)	5
Electrode thickness (mm)	5
Electrode (total horizontal) length (cm)	25
Electrode length at the parallel part (cm)	10
Electrode flared angle (°)	20

Figures 3.1 and 3.2 show the schematic of the PPT system and its electrode configuration respectively. The PPT consists of 2 parallel tongue-flared copper electrodes with flared angle 20°, main discharge capacitor of 0.94 μF, a trigger pin, polycarbonate nozzle and two PTFE rectangular pieces (5 cm × 11 cm × 35 cm) and total weight around 8g as the solid propellant fuel. The trigger voltage was fixed at 15 kV while the main discharge capacitor was charged to different voltages corresponding to discharge energy of 0.5 to 2.5 J. The main discharge capacitor consists of two *KEMET F464-AK3* capacitors, each of 0.47 μF and rated voltage of 2.5 kV (DC), connected in parallel. These are metallized polypropylene film pulse capacitors and were tested to be stable and robust. They provide consistent discharge current under low pressure environment. A side-fed configuration of the PTFE propellant fuel was preferred. Comparing to the breech-fed configuration, the side-fed one is more compact in design and allows the power electronics to be installed directly behind the electrodes. All the driver and trigger circuits

were made to fit inside a 10 cm \times 10 cm \times 10 cm aluminium casing as shown in Figure 3.3.



Figure 3.3: Exterior and interior views of the PPT unit.

3.1.2 Pulsed electronics system

The development of the pulsed electronics for the charging and trigger circuits of the PPT and its improved version is described in the following sections.

Version 1

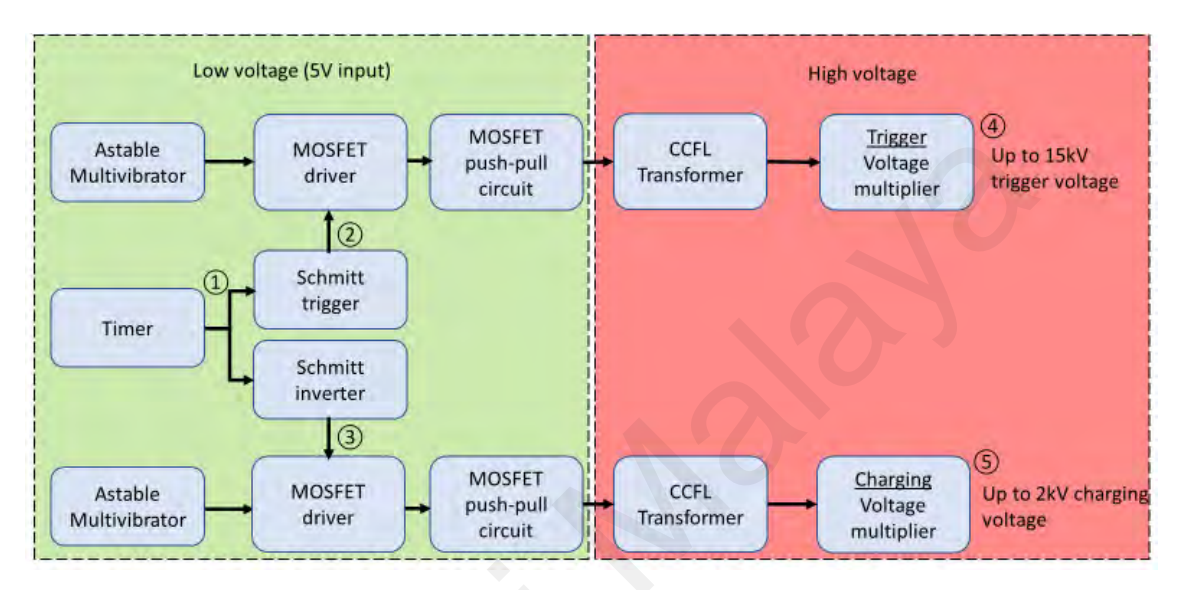


Figure 3.4: Schematic diagram of charging and trigger circuit design for the PPT.

Figure 3.4 is the schematic diagram of electronic circuit (first version) to power up and trigger the PPT. It is a DC-to-DC boost converter that is used to amplify the DC voltage from a 5 V DC supply up to 15 kV for trigger voltage. The DC-to-DC boost converter circuit consists of PWM (pulse width modulation) circuit, MOSFET push-pull circuit, centre-tapped CCFL (cold-cathode fluorescent lamp) transformer, and voltage multiplier circuit. To minimize the inductance of the system, the connections of the circuit on the PCB (printed circuit board) were routed as short as possible and at the same time fulfilled the high voltage spacing requirements. Illustrations of the signal waveforms for the different components in the circuit are shown in Figure 3.5. Detailed explanation of each component will be discussed in the next sections.

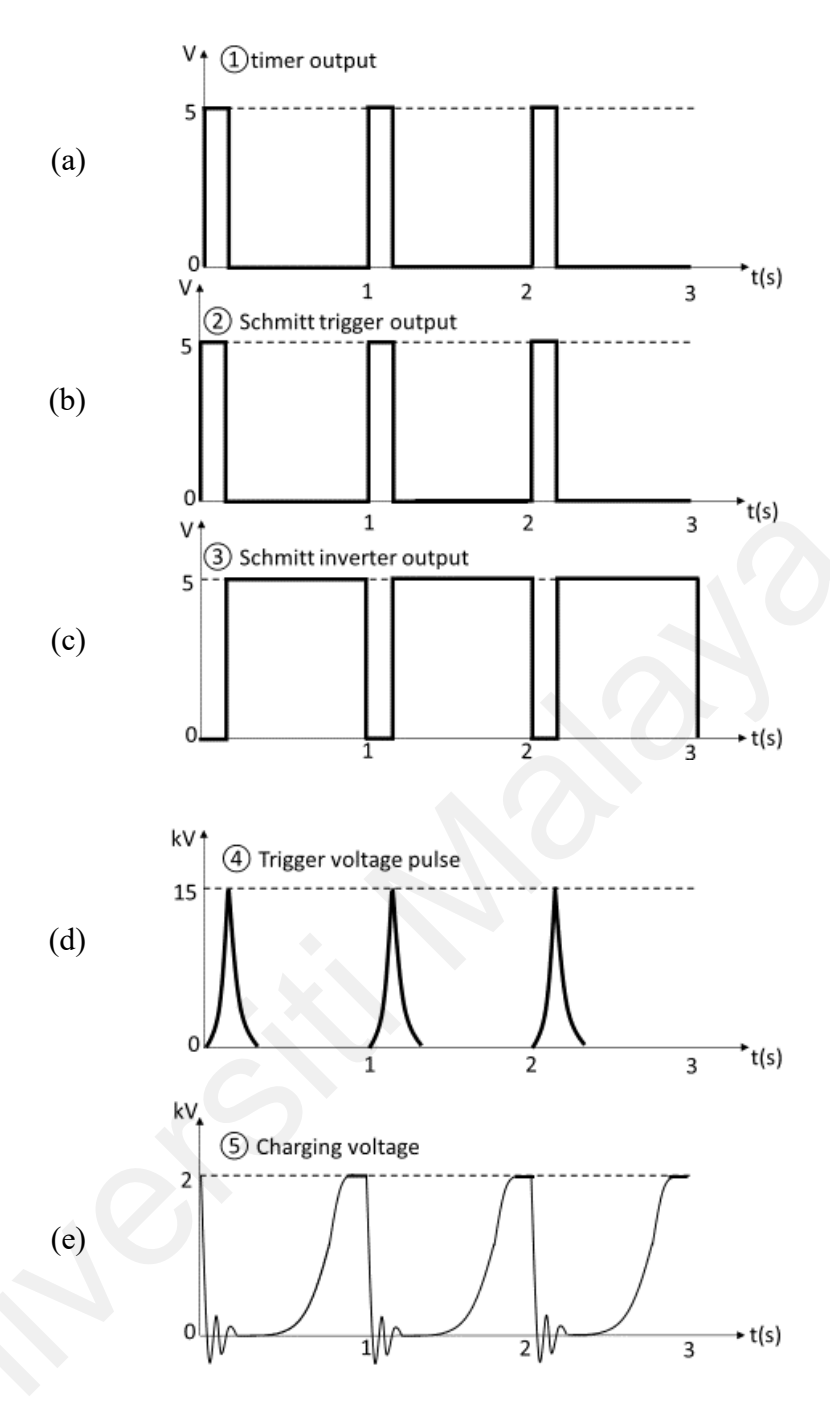


Figure 3.5: Illustrations of the signal waveforms for the different components (with reference to Figure 3.2.1) in the circuit.

(i) Timer

A 555 Timer was operated in astable mode to produce square wave pulses at frequency of 1 Hz. The pulse width was adjusted to allow enough time for the trigger voltage to reach the desired value. Figure 3.6 shows the schematic diagrams for the 555 astable oscillator circuits. The charge time (or on-time) of the 555 astable oscillator circuit is given by $t_1 = 0.693(R_1 + R_2)(C_1)$ and the discharge time (or off-time) by $t_2 = 0.693(R_2)(C_1)$. The duty cycle is calculated from $\frac{t_1}{t_1+t_2} = \frac{R_1+R_2}{R_1+2R_2} \times 100\%$. This basic astable 555 setup has a problem, that is, the duty cycle value will never go below 50%. To overcome this problem, two diodes (D₁ and D₂) were added as shown in the improved version in Figure 3.6 (b).

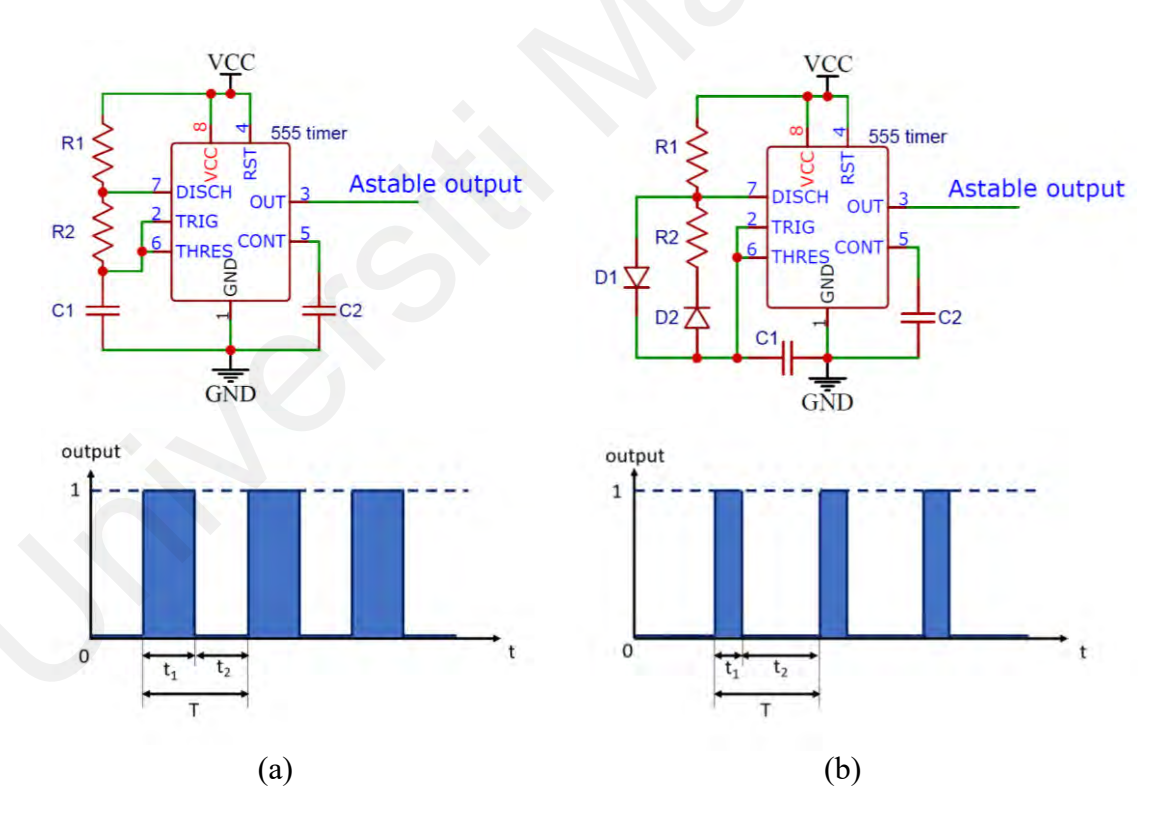


Figure 3.6: (a) Basic Astable 555 oscillator circuit, and (b) Improved Astable 555 oscillator circuit and their respective output pulses.

(ii) Schmitt trigger and inverter

The Schmitt trigger provides hysteresis or two different threshold voltage levels for the rising and falling edge, this is effective in removing noise from signals and produce a clean square wave. Schmitt inverter is similar to the Schmitt trigger except that the output signal is inverted (refer to Figures 3.5 (b) and (c)). The output of Schmitt trigger is sent to the MOSFET driver for the trigger circuit while the output of Schmitt inverter to the MOSFET driver for the charging circuit. This is to make sure that either the trigger side or charging side is turned on at any one time.

(iii) MOSFET push-pull circuit

Push–pull circuits are widely used in many amplifier outputs. The two MOSFETs (M1 and M2 in Figure 3.7) cannot be turned on at the same time. When M1 is turned on, M2 will remain turned off, and when M1 is turned off, M2 will turn on. The current will flow through the centre-tapped transformer T1 and to the ground via M1 while M2 will block the current flow on the other tap of the transformer. The opposite thing happens when M2 turns on and M1 remains turned off. M1 and M2 require a small amount of time to effectively turn on and off. The turn-on and turn-off involve a process of charging and discharging a MOSFET gate, thus the MOSFET driver is added. The driver switches with higher current, allowing the gate to charge faster, hence, MOSFET can switch on faster. The faster a MOSFET switches the lower the heat dissipation losses. Furthermore, switching MOSFET can cause a back current from the gate back to the circuit, and this can be handled by MOSFET drivers.

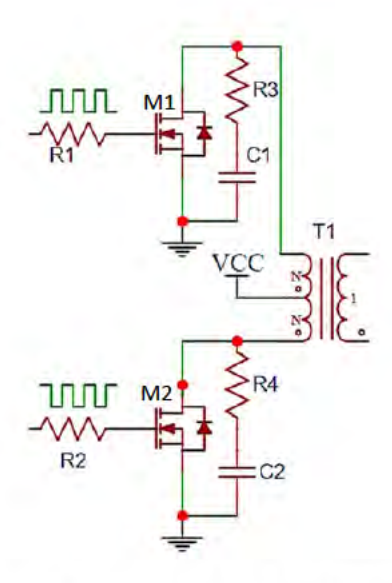


Figure 3.7: Schematic diagram of the MOSFET push-pull circuit.

The parasitic inductance of the transformer and the parasitic capacitance of the MOSFETs can form a resonant circuit that create unwanted high voltage spikes which increase stress on the MOSFETs. Hence, the RC snubber circuits (R3 & C1, R4 & C2) are added to suppress the unwanted voltage spikes.

(iv) Voltage multiplier

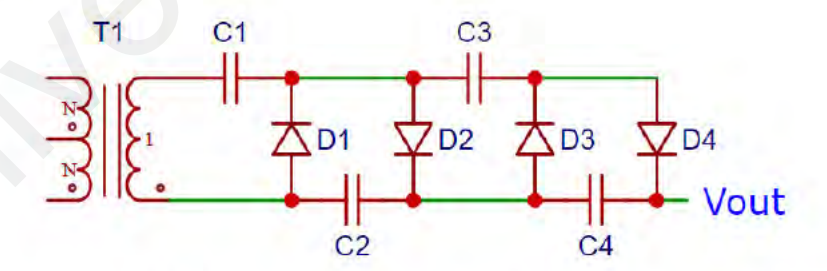


Figure 3.8: Schematic diagram of voltage multiplier.

Voltage multiplier or Cockcroft-Walton generator is an electric circuit that uses AC input at a lower voltage to generate higher DC voltage. The Cockcroft-Walton design is suited for high bias voltage but low-current application. Low AC input voltage can be amplified to much higher DC voltage by using combinations of rectifier diodes and capacitors. This circuit can be stacked to any number of stages. The output voltage, V_{out}

is the peak-to-peak input voltage (V_{pp}) multiplied by the number of stages N. The number of stages is equal to the number of capacitors in series between the output and ground. The assembly of all the circuits mentioned above was fitted into a square PCB of size 9 cm \times 9 cm as shown in Figure 3.9.



Figure 3.9: PCB design for PPT system.

Version 2 (Improved Version)

The circuit design shown in Figure 3.4 encountered heating problem in the MOSFET driver after the Schmitt inverter. The temperature of the MOSFET increased to 70°C within a few minutes after the system was turned on and the output voltage dropped, compromising its performance. To overcome this issue, the capacitor charger controller (IC LT3750) replaced the astable multivibrator component, to ensure the charging voltage remained stable (Figure 3.10).

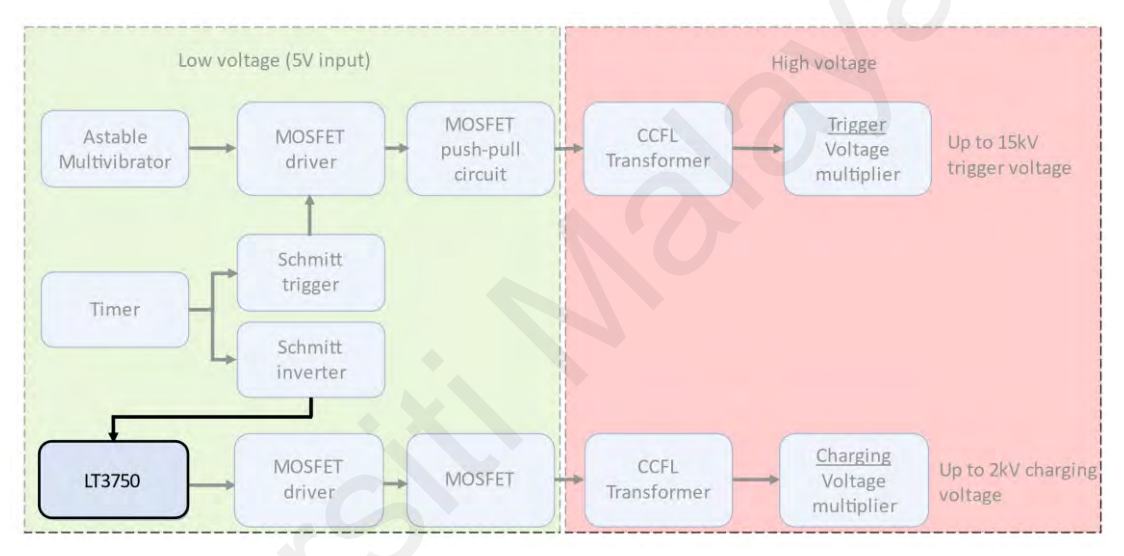


Figure 3.10: Schematic of the improved design for the PCB.

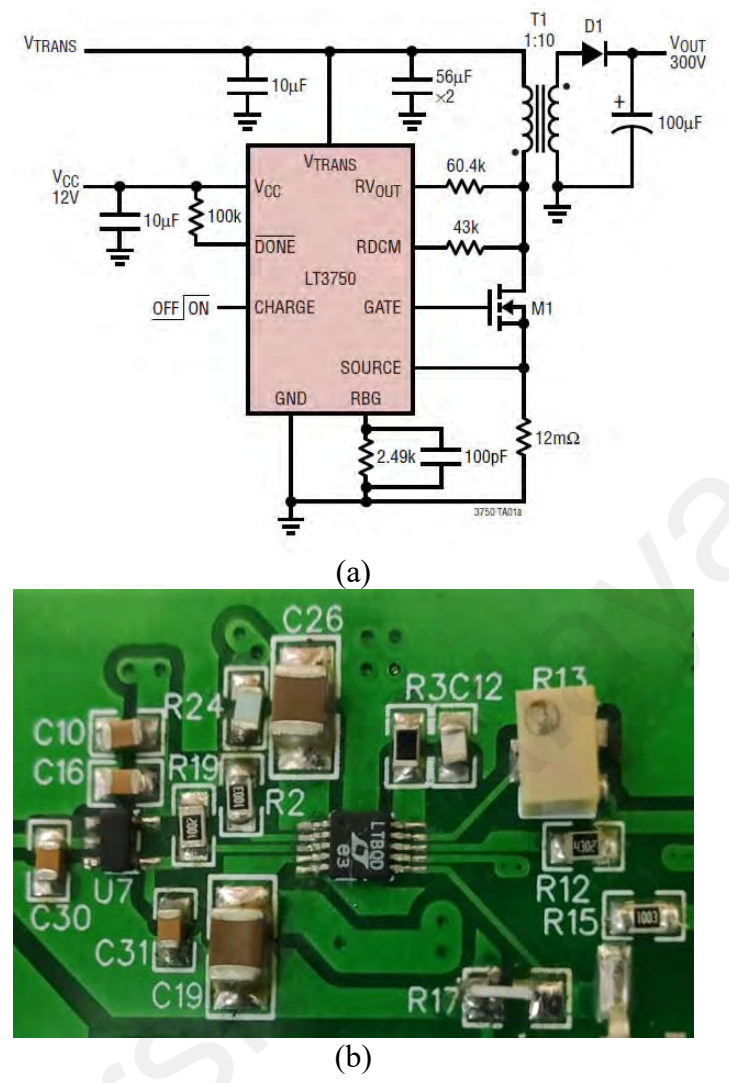


Figure 3.11: (a) Circuit diagram of capacitor charging controller using LT3750, and (b) the assembled circuit.

The LT3750 is a flyback converter designed to rapidly charge large capacitors to an adjustable target voltage. The target output voltage was set according to the following equation.

$$V_{out} = \left(1.24V \times \frac{R_{Vout}}{R_{BG}} \times N\right) - V_{diode} \tag{3.1}$$

where the parameters that determine the output voltage are the resistors, R_{vout} and R_{BG} , the turns ratio of the transformer (N), and the voltage drop across the output diode (V_{diode}) . The charging process will pause when the target output voltage was reached. This will

increase the efficiency of the overall circuit. Figure 3.11 shows the circuit diagram and the actual assembled circuit of LT3750.

3.1.3 Vacuum system

The entire PPT system was mounted inside a cylindrical vacuum chamber (Figure 3.12) of internal diameter of 0.4 m and internal length of 0.7 m. A total of nine NW40 ports (three ports arranged horizontally at each of the opposite sides of the cylinder) and two NW50 ports (one each at the front and back cover plates) are used for insertion of probes, vacuum pump fittings, as cables feedthrough and optical windows. The chamber was pumped down using Balzers TPH-190 Turbo Molecular pump (190 L/s) backed by Edwards E2M18 dual stage rotary vane mechanical vacuum pump (5 L/s). Gas pressure measurement was made using an Edwards Active Pirani gauge APG-L-NW16.

The lowest achievable pressure was in the order of 10⁻⁶ mbar (10⁻⁴ Pa) when the chamber was empty. When the entire PPT system and the thrust stand were installed, the lowest pressure achievable was 5×10⁻⁵ mbar (5×10⁻³ Pa). The working pressure of the PPT was made to be as low as possible to mimic the low-pressure environment at the low Earth orbit altitude of 300-800 km at which CubeSats are usually parked (Polat et al. ,2016). The ambient pressure at altitude 500 km is 10⁻⁸ to 10⁻¹⁰ mbar. Within the vicinity of an object at the low Earth orbit, the pressure is 10⁻⁴ to 10⁻⁶ mbar due to outgassing (Horneck, 2011). In comparison, the lowest achievable pressure in our system still higher by at least one order of magnitude. With reference to published works, it is necessary to operate at the range of 10⁻⁶ to 10⁻⁷ mbar (Ciaralli et al, 2015; Pottinger et al., 2011)) for qualification test of the propulsion system for launch. However, for study on plasma properties of the plasma thrusters, pressure of the order of 10⁻⁵ mbar have been reported (Ling et al., 2018; Wu et al., 2020; Zhou et al., 2020).

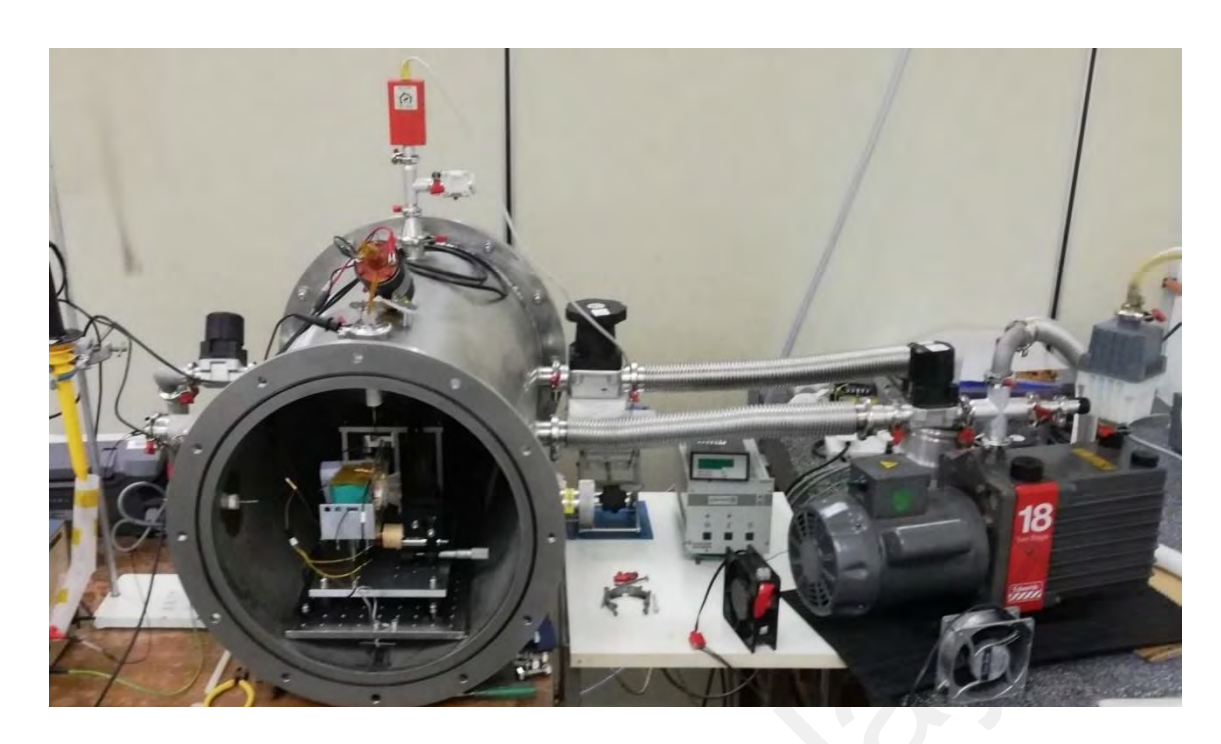


Figure 3.12: Vacuum chamber and pump system for the experiment.

For the Triple Langmuir Probe measurements, another smaller cylindrical vacuum chamber was used. The inner diameter of this chamber was 0.32 m (wall thickness 0.53 cm) with height 0.15m. A total of eight NW40 ports (all ports are arranged evenly along the curved surface, with an angle difference of 45° between each port) are used for insertion of probes, vacuum pump fittings, as cables feedthrough and optical windows. The lowest pressure achievable with entire system installed was 5×10^{-5} mbar, but in order to standardize the experiment results, the pressure was made to operate as the same pressure with the large chamber.

3.2 Thrust measurement and plasma diagnostics

3.2.1 Thrust measurement

A sub-µN torsional thrust stand developed by Lam et al. (2019) was used to measure the impulse bit produced by the PPT. Unlike hanging or inverted pendulum type thrust stand, the torsional thrust stand response is independent of thruster mass since its plane of motion is perpendicular to the gravity vector. Furthermore, the horizontal configuration is well suited for the cylindrical type of vacuum chamber as shown in Figure 3.12.

Figure 3.13(a) shows a simple illustration of a top view of the torsional thrust stand. A counterweight of the same mass is added on the other side of the torsional arm. This will ensure that the centre of mass of the system is close to the pivot. Having a counterweight also makes the system more stable and reduces the vibrational noise (Haag, 1997; Mirczak, 2003).

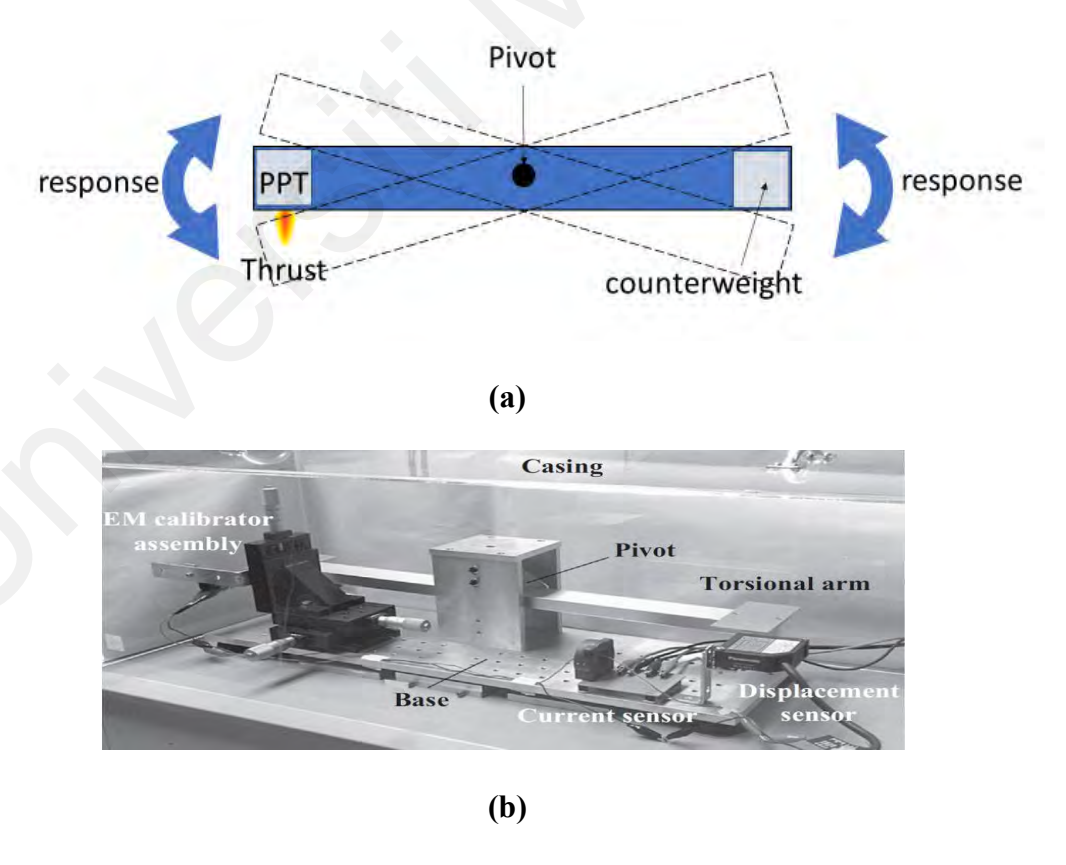


Figure 3.13: (a) Schematic (top view) showing the response when a thrust is applied to one arm of the thrust stand, and (b) photograph of the torsional thrust stand system.

As shown in Figures 3.13(b) and (c), the thrust stand consists of a few main parts, which include:

i) Torsional arm

The length of the entire torsional arm is 60cm. The sensitivity of thrust stand is proportional to the length of the arm but at the same time, it should be able to fit inside the chamber. Therefore, the length chosen is based on a compromise between the limited space available and the appropriate sensitivity of the device. To further optimize the torsional arm design, a U-shape configuration is employed instead of a solid shape. This design choice is motivated by the dual objective of maintaining structural strength and minimizing weight. The U-shape configuration allows the arm to retain its integrity and durability while simultaneously reducing its overall weight. The weight of the torsional arm is around 210g.

ii) Pivot

In this thrust stand, the pivot used was the F-20 C-flex bearing with diameter 9.53mm and torsional spring rate of 0.0054 Nm/degree. It allows oscillations in one plane only.

iii) Laser displacement sensor

The impulse produced by the PPT can be calculated from the displacement of the arm. A Panasonic compact laser displacement sensor (HL-G103-S-J) was mounted at one end of the torsional arm to measure its displacement. The laser displacement sensor has a measuring resolution as low as 0.1 µm and a sampling rate of 5kHz which is sufficient for the displacement measurement. The laser displacement sensor was connected to the computer, and the software (HL-G1SMI) was used for data acquisition and control interface.

iv) Magnetic damper

A damper is needed to dampen the oscillation of the thrust stand. A strong neodymium permanent magnet was placed underneath the torsional arm as shown is Figure 3.14.

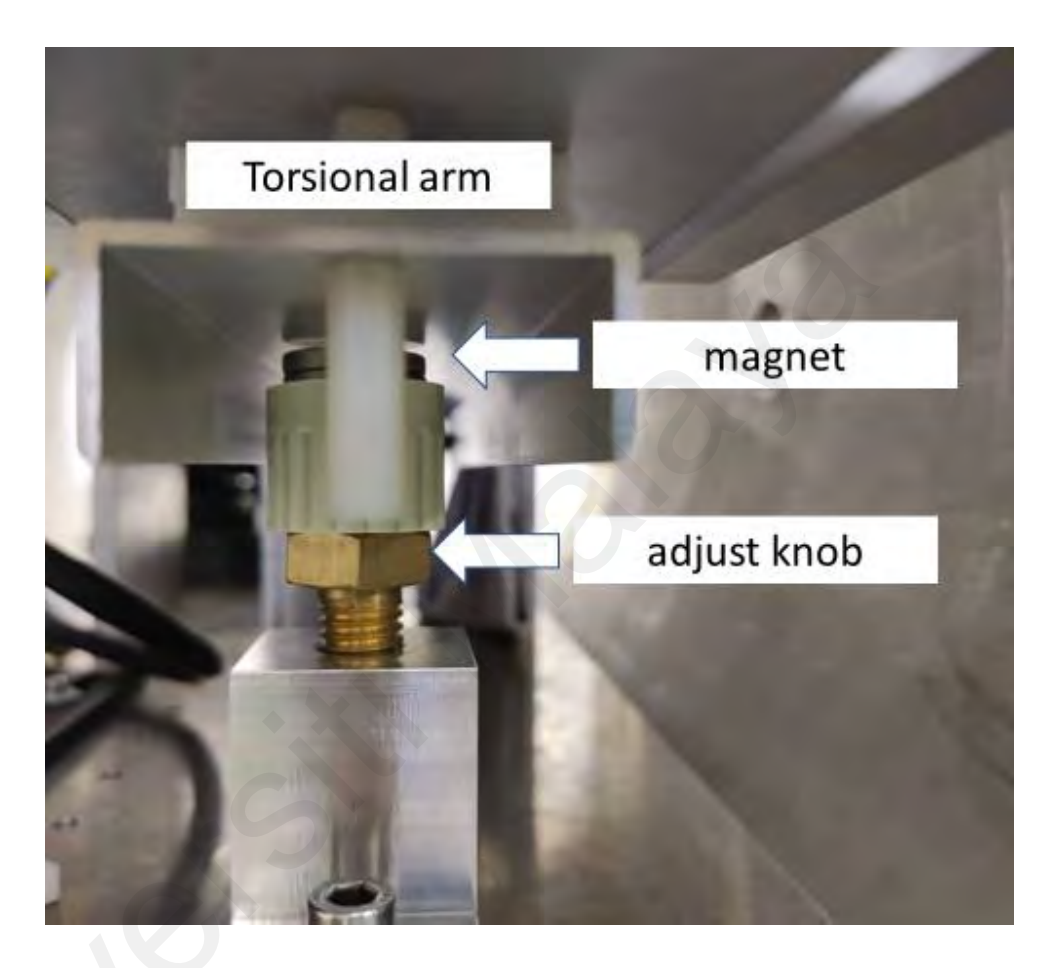


Figure 3.14: Set up of magnetic damper.

When the arm oscillates, the changing magnetic field lines induced eddy currents inside the arm, and it produce a force which is in opposite direction of the motion of the arm. The setup is simple and non-contact method, which will not affect the displacement measurement.

v) Anti-vibrational mounts

As shown in Figure 3.15, four anti vibration mounts were installed underneath the base plate. It is used to isolate the external vibrations transmitted to the thrust stand by the base plate or table.



Figure 3.15: Anti-vibration mounts for the base plate.

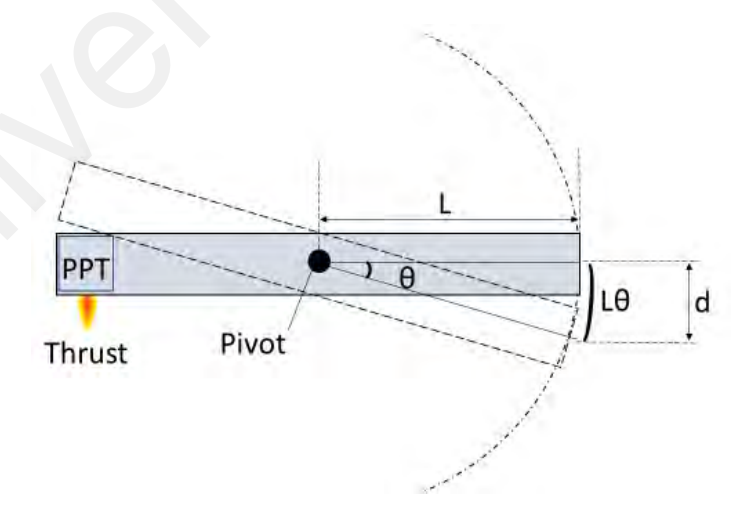


Figure 3.16: Schematic of torsional thrust stand for equation derivation of force and displacement measurement.

By referring to Figure 3.16 above, the torque produced, and the displacement can be obtained by formula below:

$$FL = k\theta \tag{3.2}$$

$$d = L\sin\theta \tag{3.3}$$

Where *F*=Force produced by the thrust,

L=length of torsional arm

k=effective spring constant

 θ =angular deflection

d=displacement of torsional arm

The angular deflection, θ is very small, hence

$$\sin \theta \approx \theta$$
 (3.4)

Thus, equation 3.2 can be simplified and combined with equation 3.3,

$$d = \frac{L^2}{k}F\tag{3.5}$$

The displacement d is proportional to the force F. Therefore, the displacement of torsional arm can be used to calculate the impulsive force produced by the thruster.

A simple setup comprising a permanent ferrite disc magnet with magnetic strength of about 100 Gauss, diameter 9mm and thickness 3mm, a voice coil, DC power supply (6306D, Topward) and weighing balance (HR-250AZ, resolution 0.1 mg) was used to calibrate the force shown in Figure 3.17. Voice coil is a type of solenoid which is commonly used in loudspeakers. An electromagnetic field can be generated by passing through a DC current through the coil. The strength of electromagnetic field of the voice coil, *B*, is governed by Ampere's Law:

$$B = \mu_0 n I \tag{3.6}$$

where μ_0 is the permeability of vacuum,

n is the number of turns of wire per unit length, and

I is the amount of electrical current flow through the coils.

By varying the current, different magnitude of magnetic field strength can be produced. When the applied DC power supply provide current was varied from 0.05 A to 0.4 A, the distance between magnet and voice coil varied from 0mm to 8mm. The magnet was arranged such that the voice coil and magnet repel each other.

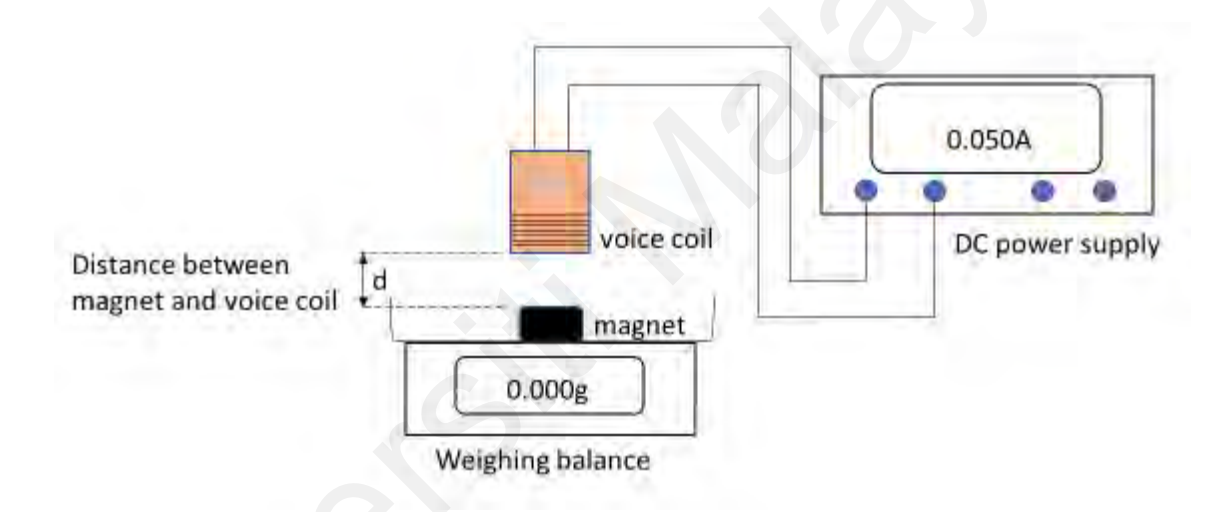


Figure 3.17: Set up for the force calibration measurement.

The calibration force of different current and distance is shown in Figure 3.18. The magnet was then installed on the torsional arm as shown in Figure 3.19. The voice coil was connected to the RIGOL DG4062 function waveform generator. Pulses of square wave with different amplitude and pulse width (from 5ms to 20ms) were sent to the voice coil to reproduce the calibration forces as shown in graph 3.18. The current magnitude was measured using a current sensor (CTSR1-P) and Tektronix 2024B digital oscilloscope.

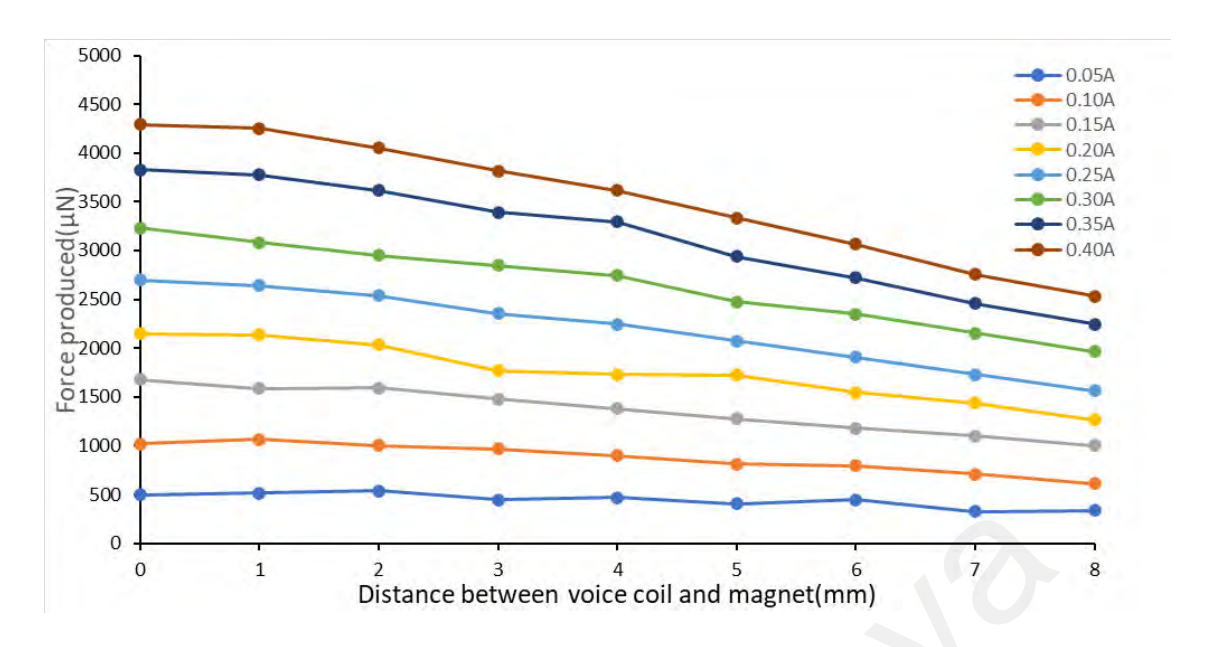


Figure 3.18: Graph of calibration of force measurement.

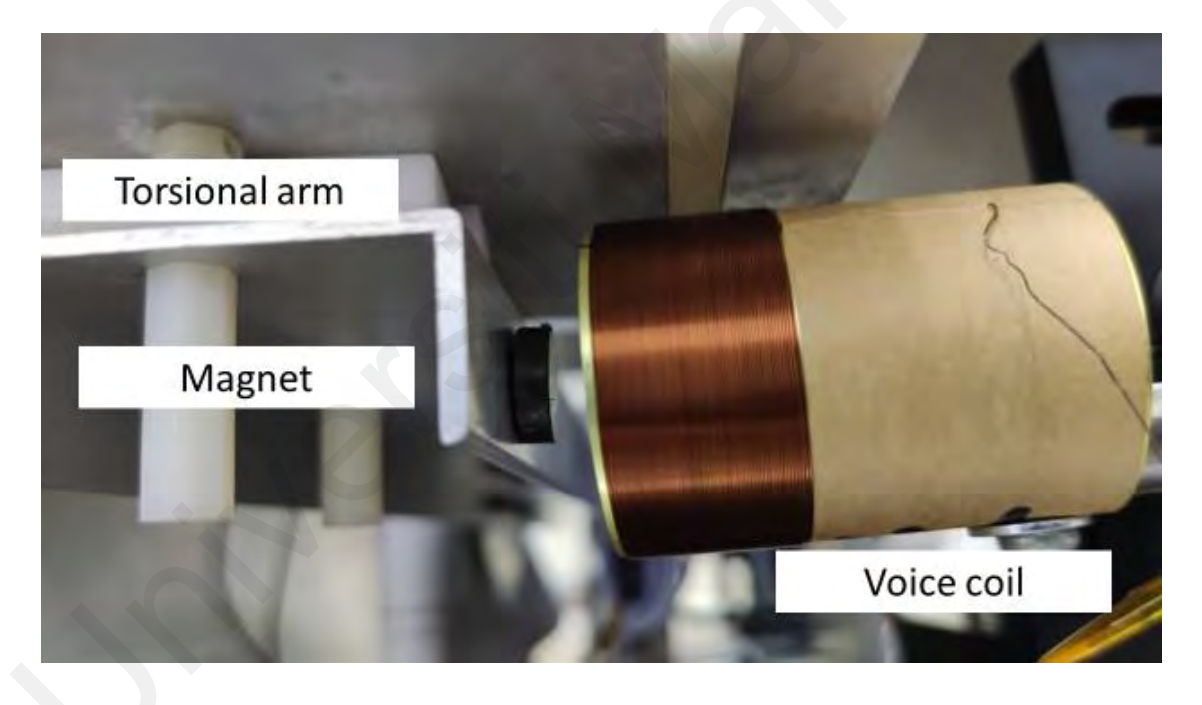


Figure 3.19: Installation of permanent magnet on torsional thrust stand

The pulse width should be within one-tenth of the natural period of the thrust stand. (Souza & Ketsdever, 2005)

$$T < \frac{1}{10} \left(\frac{1}{f_{nat}} \right) \tag{3.7}$$

The natural frequency, f_{nat} depends on the balance arm length, mass and position of the thruster and the counterweight. It is also influenced by the electrical wires connected to

the thruster via the feedthrough. f_{nat} can be determined by using the Fourier transform of the displacement readings under free motion of 1 minute. As shown in Figure 3.20, the natural frequency is determined to be 0.59Hz. By referring to Equation 3.7, the period of the pulse width should not exceed 169 ms.

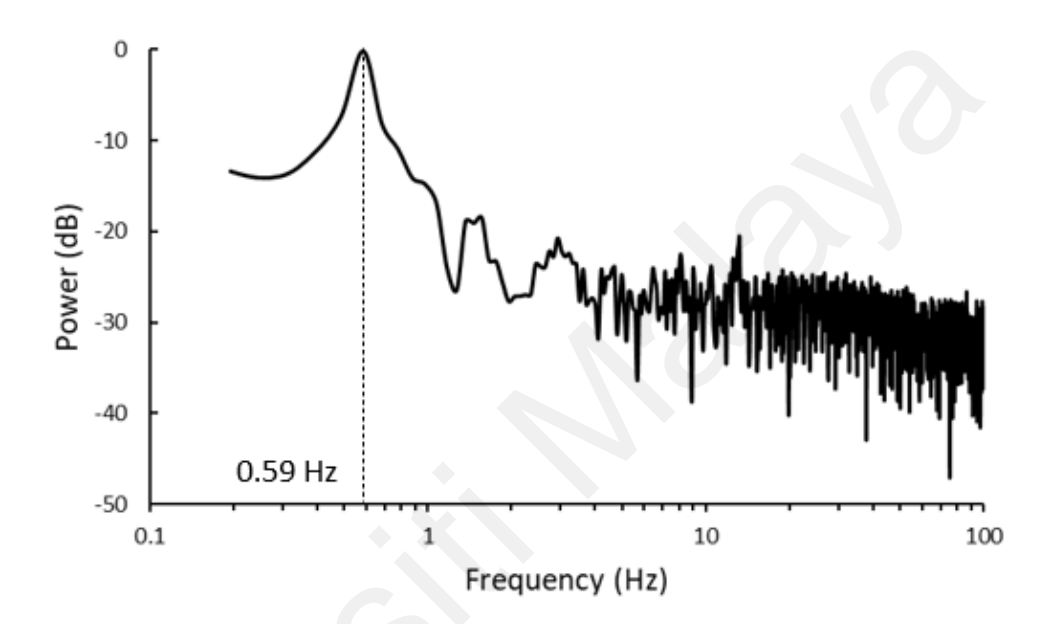


Figure 3.20: Example of Fourier Transform used to evaluate the natural oscillation frequency.

The impulse bit created by the voice coil, I_{bit} can be obtained by integrating the force across the time interval of signal pulse,

$$I_{bit} = \int_0^{t_{pulse}} F \ dt \tag{3.8}$$

Where $I_{bit} = impulse bit$

 $t_{pulse} = time interval of the pusle signal$

 $F = force \ produced \ by \ the \ voice \ coil$

The impulse bit measured was then calibrated with the displacement of the torsional thrust stand as shown in Figure 3.21. The impulse bit produced by the thruster can be obtained from this calibration curve.

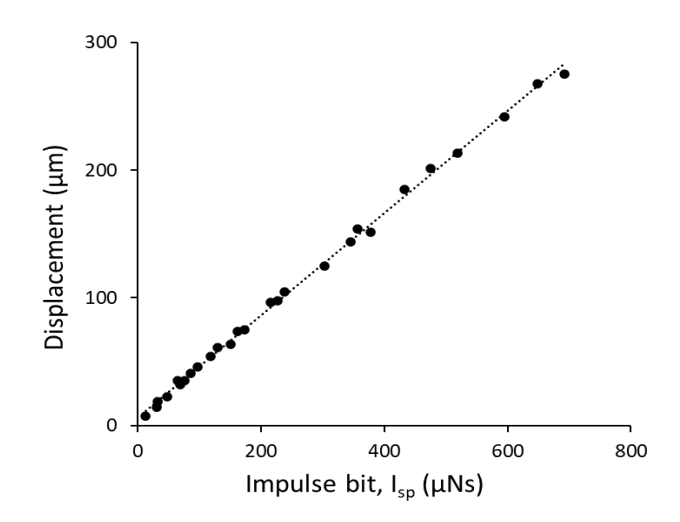


Figure 3.21: Electromagnetic calibration curve for impulsive force measurement.

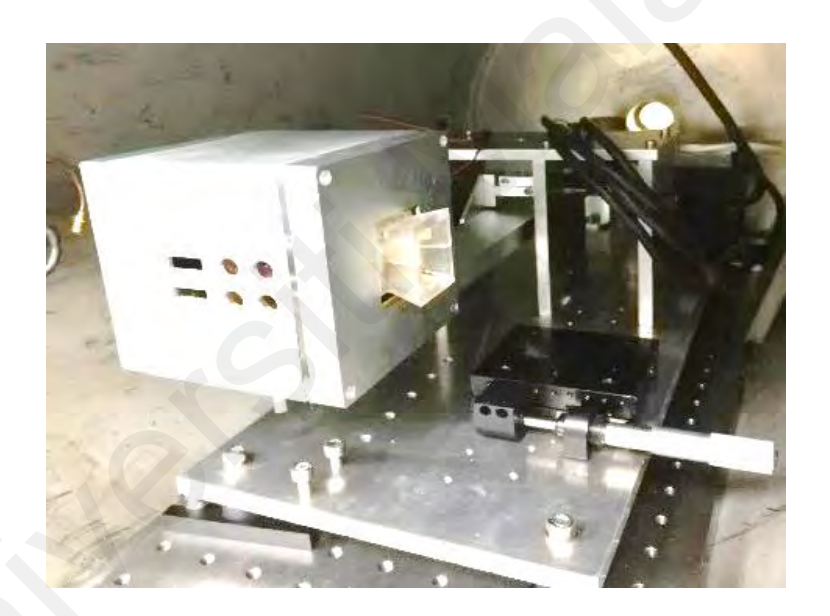


Figure 3.22: Actual setup for impulse bit measurement for the pulsed plasma thruster.

3.2.2 Discharge voltage-current measurement

The discharge voltages were measured using a TESTEC HV-15-HF 1000x high voltage probe and the discharge currents using a Rogowski coil that consisted of a wound induction coil of 40 turns and a resistor-capacitor integrator. The voltage and current signals were acquired using the Tektronix TDS2024B oscilloscope.

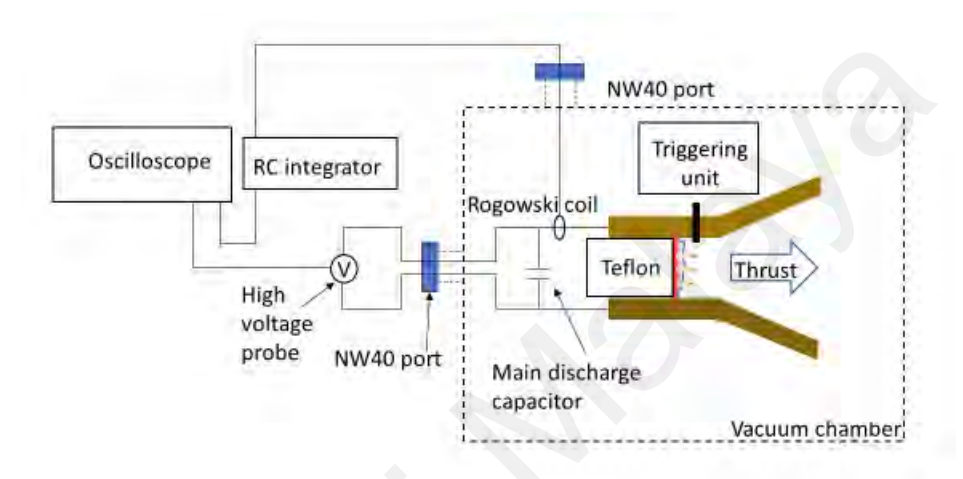


Figure 3.23: Setup for voltage and current measurement.

3.2.3 Triple Langmuir Probe measurements

The triple Langmuir probe is a plasma diagnostic technique used for measuring electron temperature $T_{\rm e}$ and electron number density $n_{\rm e}$. It was first outlined by Chen & Sekiguchi (1965) for use in collisionless, Maxwellian low-temperature plasmas. Triple Langmuir probes do not require a voltage or frequency sweep common to other Langmuir probe methods. This feature makes triple Langmuir probe ideal for time varying plasmas and plasmas that have fast transients such as the plasma plume of a PPT.

A triple probe consisting of three exposed Tungsten wires was aligned with the plasma flow. The wires, each of diameter 0.2 mm, were fed through a 4-hole alumina tube, with 3 mm length at the tip being exposed to the plasma. The alumina tube serves to insulate the wires and provide mechanical support.

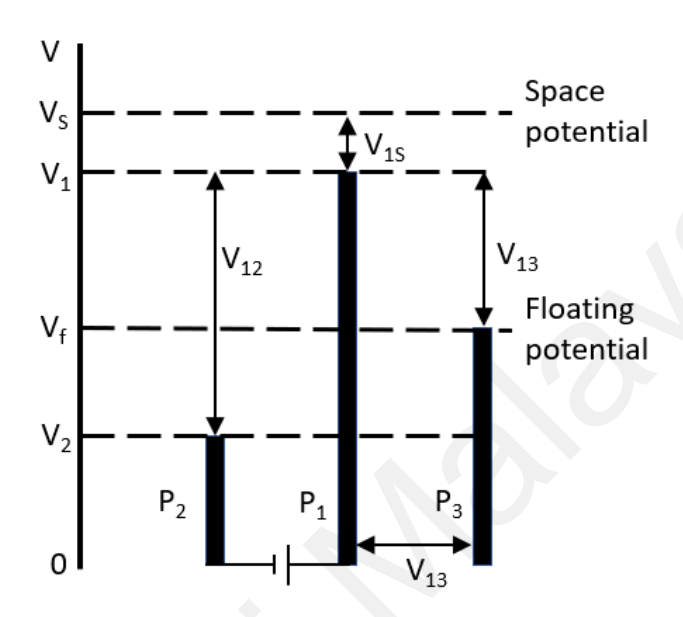


Figure 3.24: Diagram of electric potential of triple Langmuir probe.

One of the probes, indicated as probe 3 in Figure 3.24, is the floating probe. 27 V DC was supplied to probes. This selected biased voltage ensures that all three probes operate in reasonable proximity to the floating potential such that they collect current that vary by small amount only. (Lobbia & Beal, 2017)

The Debye length, assuming a quasi-neutral plasma is

$$\lambda_D = \sqrt{\frac{\varepsilon_0 k T_e}{e^2 n_e}} \tag{3.10}$$

The dimension of the probe was carefully designed such that the probe radius, to Debye length ratio, $\frac{r_p}{\lambda_D} > 100$. For $\frac{r_p}{\lambda_D} > 100$, thin-sheath current collection model was used, the ion current to a probe is independent of the bias voltage and the ion current to the probe

can then be approximated as the ion current to the sheath that is given by the Bohm expression:

$$I_i = A_p e n_e \sqrt{\frac{kT_e}{m}} exp(-\frac{1}{2})$$
(3.11)

The full system using the thin-sheath equation is as follows:

$$I_1 = A_p J_{eo} \exp\left(-\frac{eV_{s1}}{kT_e}\right) - A_P e n_e \sqrt{\frac{kT_e}{m}} \exp(-\frac{1}{2})$$
 (3.12)

$$I_2 = A_p J_{eo} exp \left[\frac{e(V_{s1} + V_{12})}{kT_e} \right] - A_P e n_e \sqrt{\frac{kT_e}{m}} exp(-\frac{1}{2})$$
 (3.13)

$$I_{3} = A_{p}J_{eo}exp\left[\frac{e(V_{s1} + V_{13})}{kT_{e}}\right] - A_{p}en_{e}\sqrt{\frac{kT_{e}}{m}}exp(-\frac{1}{2})$$
(3.14)

The equations above can be manipulated into expressions for T_e and n_e :

$$\frac{I_1 - I_3}{I_1 - I_2} = \frac{1 - exp(-\frac{eV_{13}}{kT_e})}{1 - exp(-\frac{eV_{12}}{kT_e})}$$
(3.15)

$$n_{e} = \frac{1}{eA_{p}\sqrt{\frac{kT_{e}}{m}exp(-\frac{1}{2})}} \left[\frac{I_{2} - I_{1}exp(-\frac{eV_{13}}{kT_{e}})}{exp(\frac{eV_{13}}{kT_{e}}) - 1} \right]$$
(3.16)

Since the probe 3 is floating, so $I_3 = 0$, and $I_1 = I_2$. The equations 3.15 and 3.16 can be rewritten into equation 3.17 and 3.18.

$$\frac{1}{2} = \frac{1 - exp(\frac{-ev_{13}}{kT_e})}{1 - exp(\frac{-ev_{12}}{kT_e})}$$
3.17

$$n_e = \frac{1}{eA_p \sqrt{\frac{kT_e}{m} exp(-\frac{1}{2})}} \left[\frac{I}{exp\left(\frac{eV_{13}}{kT_e}\right) - 1} \right]$$
 3.18

The value of electron temperature, $T_{\rm e}$ can be obtained via equation 3.17 using just the biased voltage, V_{12} and the voltage difference between the floating potential and the positively biased probe, V_{13} . The value of V_{13} was obtained through subtraction of the signals from probe 1 and probe 3 digitally on the Tektronix TDS2024B oscilloscope. This method was proved to be less susceptible to the noise than using the differential probe. (Eckman et al., 2001; Kelly & Jahn, 1990) The electron density, $n_{\rm e}$ can be calculated from equation 3.18.

The LOESS (locally estimated scatterplot smoothing) algorithm was applied to the voltage and current data to reduce noise (as shown in Figure 3.25). The main error in Langmuir probe measurements is due to the smoothing of the high frequency noise picked up by the voltage probes, this introduced a 15% uncertainty into the measurements.

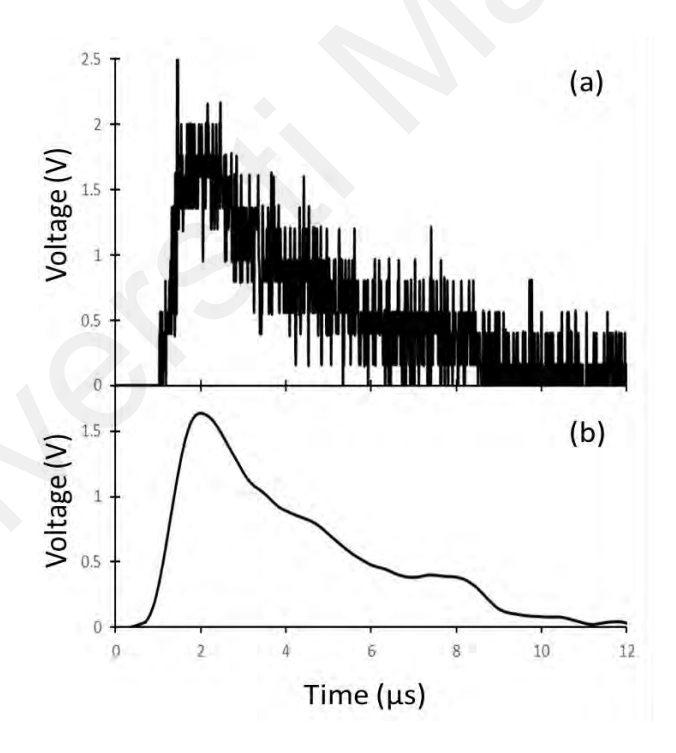


Figure 3.25: Typical V_{13} signal from the triple prob (a) unfiltered and (b) after noise filtering.

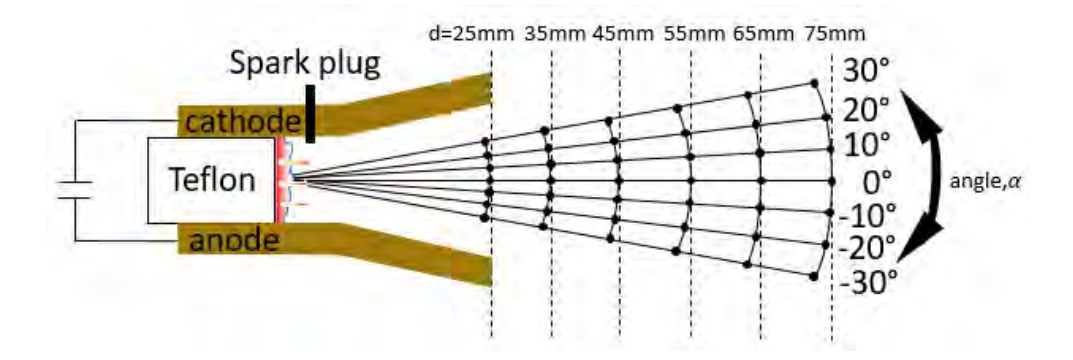


FIGURE 3.26: The perpendicular plane with marked positions (black dots) where Langmuir probe measurements are made.

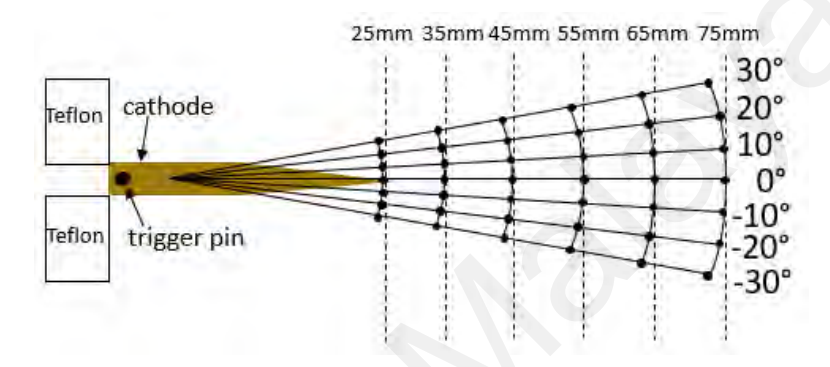


Figure 3.27: The parallel plane with marked positions (black dots) where Langmuir probe measurements are made.

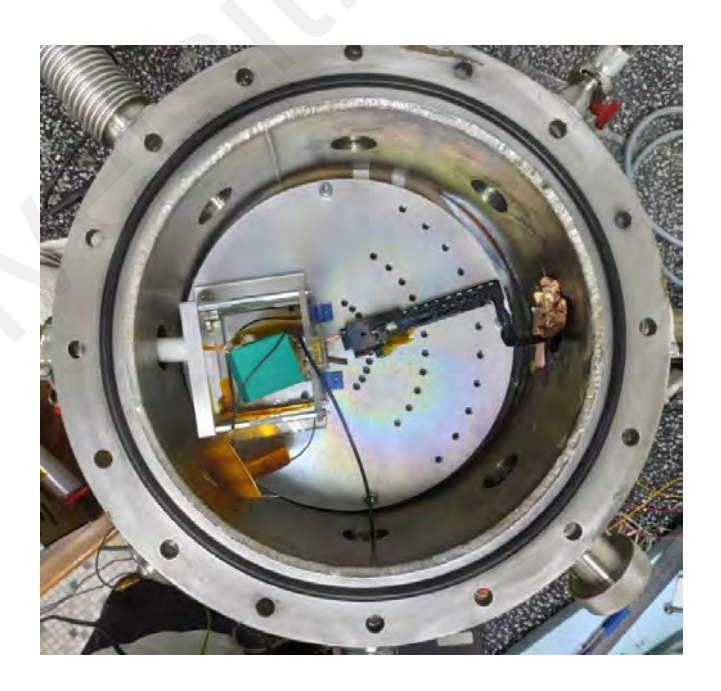


Figure 3.28: Aluminium base plate with different drill holes.

As shown in Figure 3.26 and Figure 3.27, the end of the PPT electrodes is considered to be d=25 mm. Starting from d=25 mm, the spatial positions are marked in steps of 10mm up to a maximum of d=75mm along a radial line. The measurements are made along different radial lines of incremental angle 10 degrees up to 30 degrees to the right and left of the central line; and it was repeated in a plane perpendicular to it. As shown in Figure 3.28, a circular aluminium base plate has drilled guide holes to fix the probe at the required position and angle. The fastest velocity of ions can be calculated by using the time difference between discharge initiation and the signal recorded by the probe.

3.2.4 Triple Langmuir Probe cleaning

After multiple PPT discharges, black residue gets deposited on the tip of the probes and this contamination will affect the accuracy of the data taken. Thus, a plasma jet system was used to clean the Triple Langmuir probe tips. During cleaning, an arc is struck to the probe tip, and this arc cleans the probe of any contaminants.

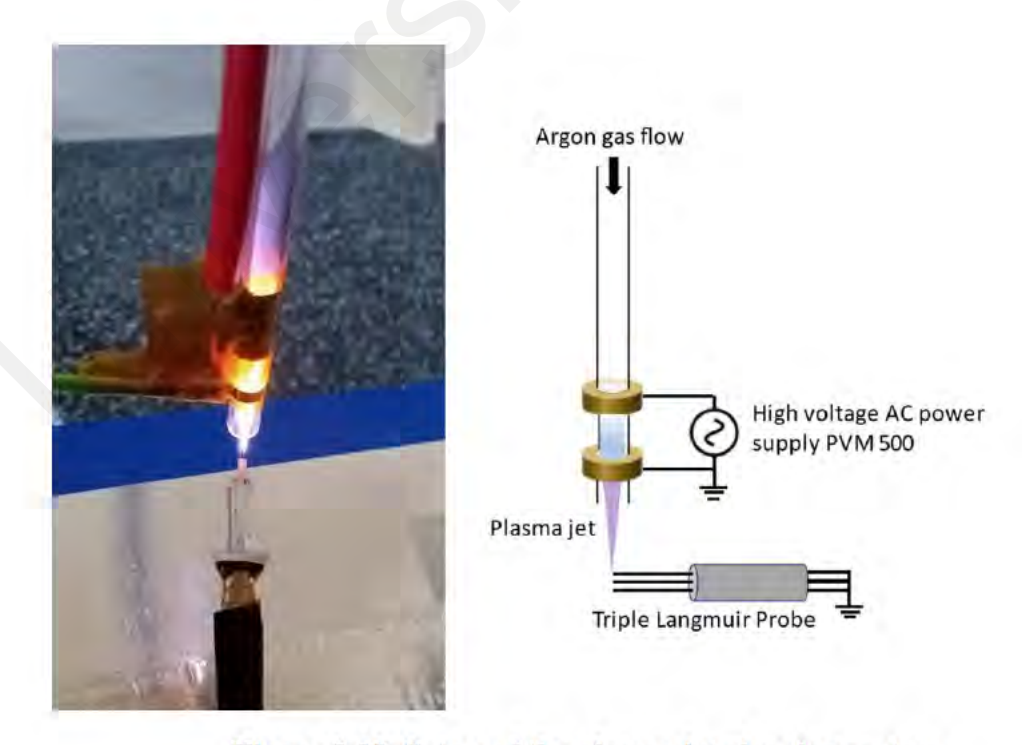


Figure 3.29: Setup of the plasma jet cleaning system

The diagram of the plasma jet cleaning system is shown in Figure 3.29. During the cleaning procedure, the probes were first disconnected from the vacuum chamber, and connected to the ground on the high voltage supply. The plasma jet system was operated under atmospheric pressure, The flow rate of Argon gas was fixed at 2 L/min. The discharge voltage was maintained around 7kV peak to peak value with frequency 28kHz. This discharge was sustained for 3 minutes (1 minute for each tip). The duration of discharge was sufficient to clean the probe tips as shown in Figure 3.30.

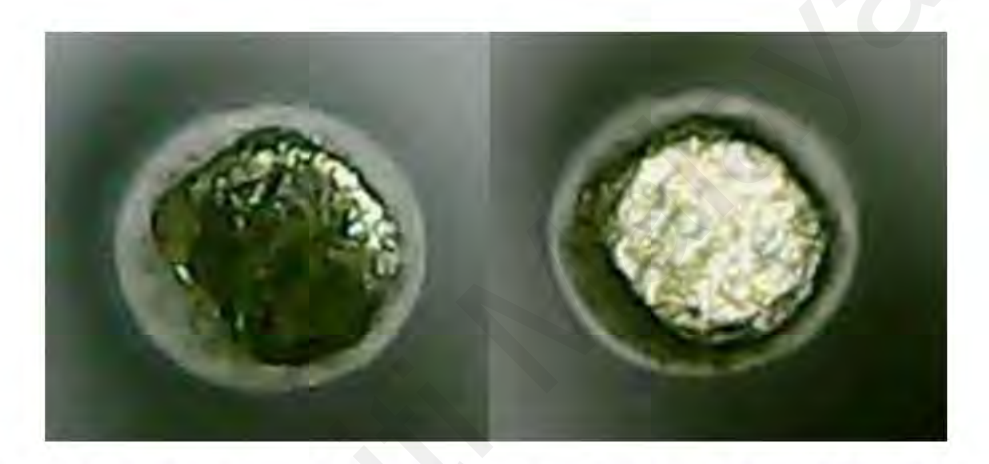


Figure 3.30: Condition of a probe tip before (left) and after (right) cleaning.

3.2.5 Optical Emission Spectroscopy

The plasma discharge species were identified from the optical emission spectra (OES) measured using the Ocean Optics HR4000 spectrometer. The spectrometer has a resolution of 0.5 nm and can measure spectral wavelengths ranging from 250 to 700 nm at 0.13 nm intervals. The wavelengths were calibrated by using a standard mercury lamp source. Spectral measurement was obtained using the SpectraSuite software. The setup for emission spectra measurement includes a quartz convex lens with focal length 10cm and a multimode fibre optic cable (400 µm, UV/SR-VIS). The lens and the fibre optic cable were mounted onto an optical table, the height and the distance were adjusted such that the collected light was focused on the entrance aperture of the optic fiber. An average of 5 data sets is taken for for each spatial position. The wavelength of the peaks in the spectra were compared to standard atomic emission lines from the NIST Atomic Spectra Database and standard emission bands from Pearse & Gaydon (1964). This will allow identification of the plasma species.

3.3 Surface erosion study

Field Emission Scanning Electron Microscope (FESEM) makes possible the visualization of very small topographic details on the surface of a sample. FESEM services provided by the (*Hitachi SU8030 UHR*) instrument at MIMOS Sdn. Bhd. The electron accelerating voltage ranging from 0.5 to 30 kV, with image resolution up to 1.0 nm. Energy dispersive X-ray spectroscopy (EDX) is an analytical technique used for the elemental analysis or chemical characterization of a sample. Each element has a unique atomic structure which allowing unique peaks on X-ray emission spectrum. The X-rays emitted from the sample can be measured by an energy dispersive spectrometer.

The copper electrode and PTFE solid fuel were sent for FESEM imaging and EDX analysis for study of surface erosion. The magnification was selected to be 5000x, 10000x, 15000x and 30000x. The electrode dimension is 10mm x 25mm x 8mm while the dimension of PTFE is 11mm x 5mm x 35mm. To fit inside the machine, the PTFE height was reduced to 10mm. Since PTFE is an electrical insulator, it must be first made conductive for FESEM imaging. This is done by coating with a thin layer of platinum. The surface of non-conductive materials causes accumulation of electrons on the surface which will creates extra-white regions on the sample and influence the image information. When coating is used, the conductive coating material acts as a channel that allows the charging electrons to be removed from the material. Coating can increase the signal-to-noise ratio during FESEM imaging and therefore produce better quality images.

CHAPTER 4: THRUST AND PROPULSION

4.1 Introduction

This chapter consists of four sections. The first section involves examining the performance of various capacitors to determine their suitability for the project. The second section include discussion of the impulse characteristics of PPT, such as impulse bit, specific impulse, mass bit, and thrust efficiency. Following that, the third section focuses on examining surface erosion and fuel consumption related to PTFE. Lastly, the fourth section involves comparing the thruster performance of this PPT with findings from others published research.

4.2 Performance comparison of different capacitor

Capacitor that designed to space based program requiring ultra-high reliability performance, no aging phenomena or hysteresis over prolonged operation and high peak current pulse capability. Those high voltage capacitors that are approved by the MIL-PRF or ESCC are expensive and not affordable. Thus, alternative capacitors are chosen from the commercial market. Space grade high voltage capacitors are ceramic as they offer low Equivalent Series Resistance (ESR) and Equivalent Series Inductance (ESL) values. Furthermore, ceramic capacitors have low outgassing issue at space environment which make them highly reliable and ideal for space-based program. However, commercial ceramic capacitors usually do not offer both high capacitance (>1 μF) and high voltage (>1 kV) rating together, if high capacitance is required then these capacitors need to be stack or connected in parallel which may cause issues such as rise in inductance and non-ideal discharge. Electrolytic type capacitors are completely unsuitable due to the containing liquid or gel inside. Film capacitors use thin plastic film as a dielectric. These capacitors are very stable over time and have very low ESR and ESL. Another interesting

^{*}A part of the content in this chapter has been published in Plasma Science and Technology, 26(4), 045502.

aspect of film capacitors is that they are self-healing, any arcing within the capacitor will vaporizes the thin metallization of the film around that spot, and this causes that area to lose its metallized coating, without the conductive material there is no longer a short, so the capacitor ceases to be in a failure mode. In this work, 4 different types of capacitors include ceramic and film capacitors are selected to test the performance on different aspects such as discharge current, inductance, impulse bit (I_{bit}), and stability (Figure 4.1). All capacitors are discharged at 2 J of energy to make fair comparison.



Figure 4.1: Capacitor used in preliminary test.

a) Ceramic capacitor

20 ceramic capacitors are connected in parallel and are charged by 1400 V of DC voltage. As shown in Figure 4.2, the discharge current waveform exhibits non-regular periodic oscillation, it is due to large number of capacitors connected in parallel. When the capacitors discharge, the energy is not overall dumped onto the discharge gap but is swung among the capacitors causing the energy losses. The ceramic capacitors are able to produce $7 \pm 3 \mu Ns$ of I_{bit} . The discharge current after 1000 shots remains almost constant, with only 0.01% drops (Figure 4.3).

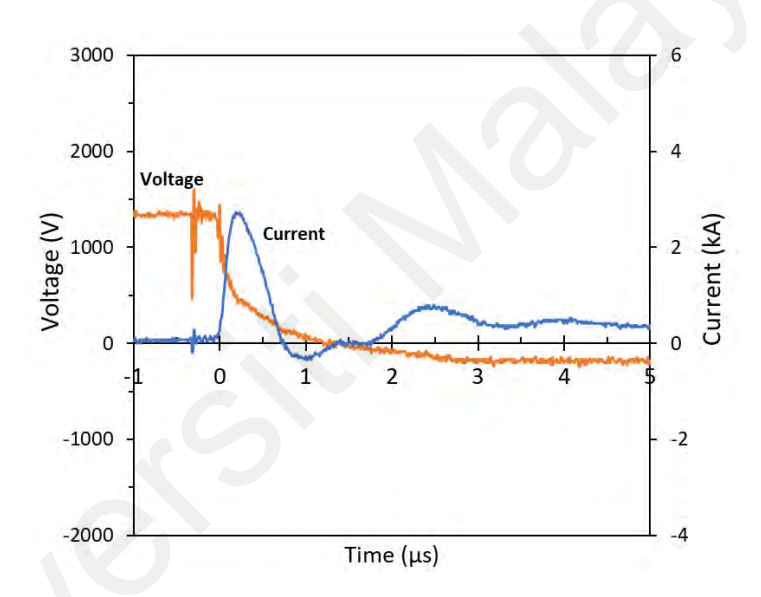


Figure 4.2: Electrical discharge voltage and current waveforms of ceramic capacitor.

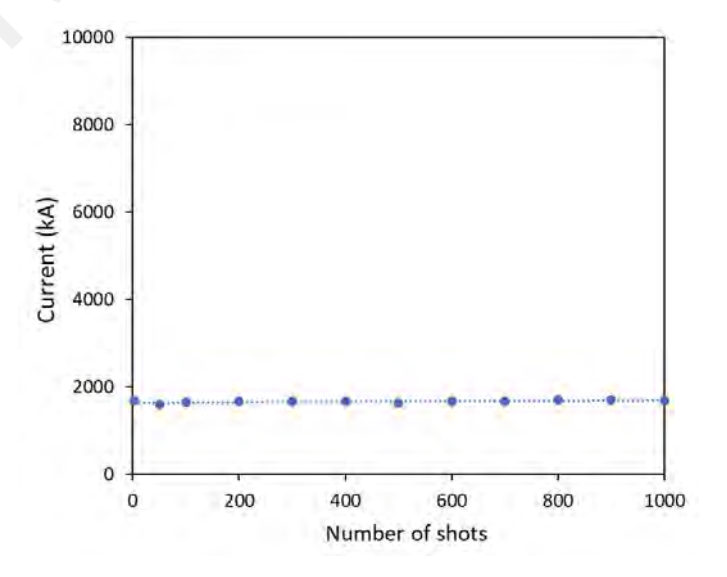


Figure 4.3: Discharge current against number of shots of ceramic capacitor.

b) Polypropylene film capacitors (105J)

Two polypropylene film capacitors are connected in parallel and charged up to 1600 V DC voltage. As show in Figure 4.4, the oscillation period is around 2.0 μ s, with overall inductance of 65nH. This capacitor is able to produce I_{bit} of 17±3 μ Ns. After firing for 1000 shots consecutively, the discharge current shows a linear drop from 6.7 kA to 5.3 kA, decrease by 22%.

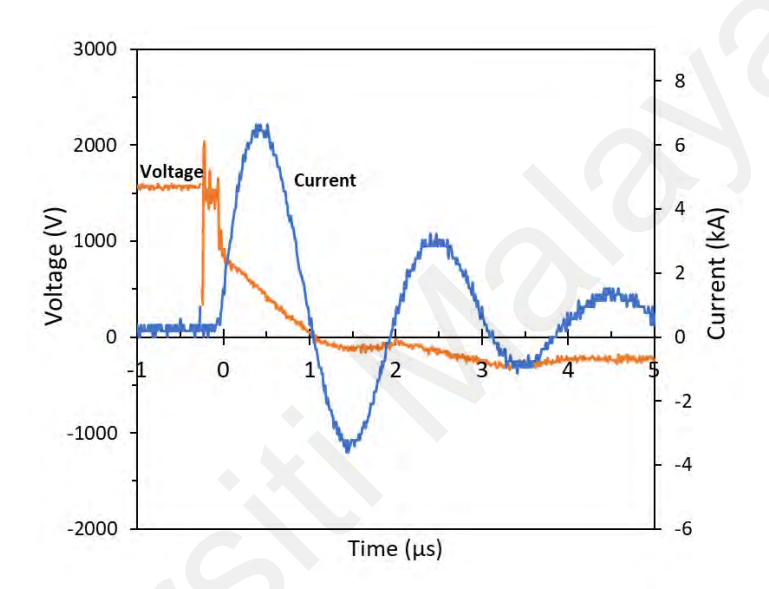


Figure 4.4: Electrical discharge voltage and current waveforms of polypropylene film capacitor (105 J).

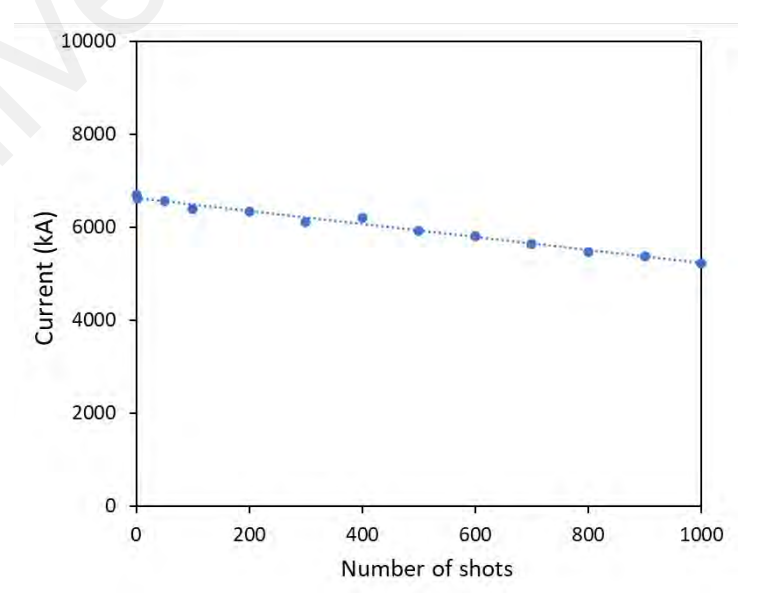


Figure 4.5: Discharge current against number of shots of polypropylene film capacitor (105 J).

c) Polypropylene film capacitors (225J)

1350 V DC voltage is used to charge this capacitor. The oscillation period is around 2.73 μ s with inductance of 86 nH (Figure 4.6). This capacitor is able to produce I_{bit} of 14±4 μ Ns. Similar with the polypropylene film capacitor, the discharge current shows a linear drop from 7 kA to 5.5 kA in 1000 shots, which shows a decrease of 23%.

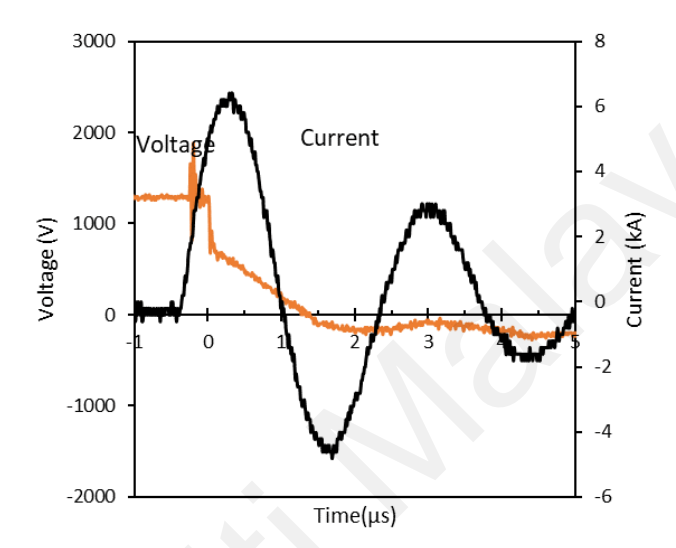


Figure 4.6: Electrical discharge voltage and current waveforms of polypropylene film capacitor (225 J).

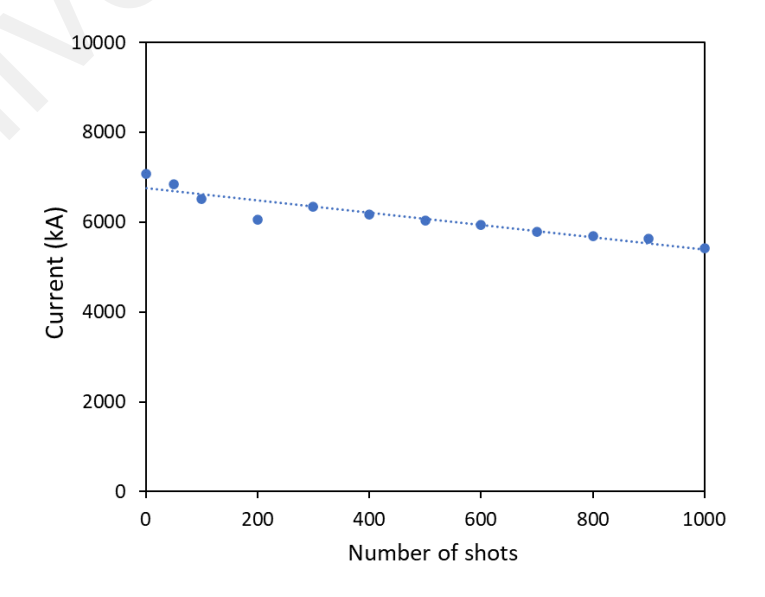


Figure 4.7: Discharge current against number of shots of polypropylene film capacitor (225 J)

(d) **KEMET** capacitor

The F464 series capacitor is a metallized polypropylene film encapsulated with self-extinguishing resin, in a box of material meeting the requirements of UL94V–0. Two capacitors are connected in parallel (total 0.94 μ F) and with discharge voltage of 2100 V. The oscillation period is around 1.2 μ s with inductance of 39 nH. This capacitor is able to produce $I_{\rm bit}$ of $26\pm2~\mu{\rm Ns}$. The discharge current also shows a linear drop from 8kA to 6.5kA in 1000 shots.

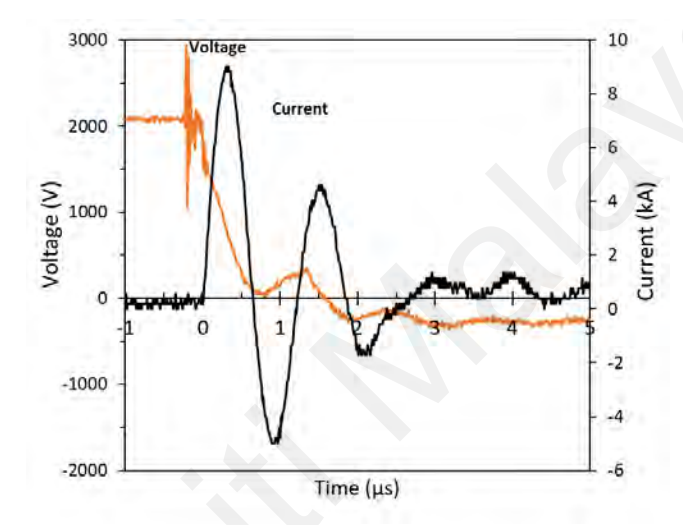


Figure 4.8: Electrical discharge voltage and current waveforms of KEMET capacitor.

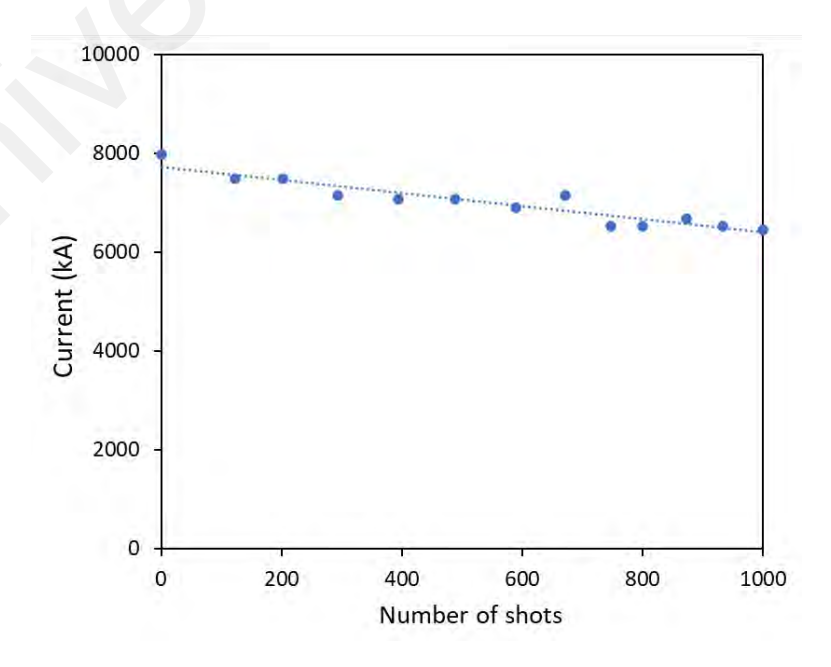


Figure 4.9: Discharge current against number of shots of KEMET capacitor.

Table 4.1: Results comparison between capacitors for preliminary test.

Type of capacitor	Total mass (g)	Inductance (nH)	Discharge current (kA)	Impulse bit (μNs)	Performance drops after 1000 shots
Ceramic STE-104	≈40	22	1.7	7	0.01%
PP 105J	≈30	65	6.7	17	22%
PP 225J	≈25	86	7.1	14	23%
KEMET F464 AK9	≈120	39	7.9	26	19%

Table 4.1 shows the comparison between all capacitors used in the preliminary test. KEMET capacitor is the heaviest among all, about 5 times heavier than the lightest polypropylene film capacitor, but since this work focus on the performance on low discharge energy, not the lifetime qualification test on flight unit, mass is not a crucial factor for capacitor selection. Ceramic capacitor has the lowest inductance but its discharge current and I_{bit} produced is the lowest, only 1.7kA and 7 μNs. Polypropylene capacitors have larger inductance, but it is able to produce higher I_{bit} than ceramic capacitor, but the discharge current drop is around 20% for all PP type capacitor. The drop in current is due to the heating effect of rapid discharge, increase in resistance causes some energy to dissipate as heat. Among the PP capacitors, the inductance of KEMET capacitor is the lowest, about 50% less than PP (225J), the discharge current and I_{bit} produced by KEMET capacitor is the highest, up to 7.9kA and 26 μNs respectively. This value is within the range expected for discharge energy as shown in the comparison of impulse bit with discharge energy over the different energy range for various PPT designs (Igarashi et al., 2001).

Considering all the factors, the KEMET capacitor (F464-AK9) is proved to be suitable to use as the capacitor for PPT system, other capacitors are unable to achieve a decent value of $I_{\rm bit}$. The only drawback of KEMET capacitor is the large mass. It is worth noting that Austrian Research Centers have also opted for a KEMET capacitor with a similar rating for their PPT system (Pottinger & Scharlemann, 2007).

4.3 Impulse characteristic

Uncertainty in the EM calibrator system originate from the resolution of the instrumentations used. Aggregating the component errors contributed by each instrument, the uncertainty error in EM calibration can be calculated as:

$$\frac{\delta I_{bit}}{I_{bit}} = (1+\beta) \sqrt{\left(\frac{\delta I}{I}\right)^2 + \left(\frac{\delta F_c}{F_c}\right)^2 + \left(\frac{\delta x}{x}\right)^2 + \left(\frac{\delta t_c}{t_c}\right)^2 + \left(\frac{\delta \Delta x}{\Delta x}\right)^2 + (\Delta F_{ch})^2}$$
(4.1)

the term β has been added to consider all the unpredictable sources of disturbance. The known sources of error are summarized in Table 4.2. The value of β has been chosen arbitrarily to be 20% for a worst-case estimate of the error, thus a more conservative I_{bit} evaluation is achieved. In the present configuration, the uncertainty in I_{bit} measurement is 11.8%.

Table 4.2. Known source of error for uncertainty analysis.

	Relative uncertainty	Value (%)
Current, I	δΙ/Ι	2.5
EM calibration forces, F_c	$\delta F_c/F_c$	0.4
Engagement distance, x	$\delta x/x$	0.5
Pulse width, t_c	$\delta t_c/t_c$	0.7
Deflection, Δx	$\delta \Delta x/\Delta x$	4.3
Non-linearity of EM force	ΔF_{ch}	8

4.3.1. Impulse bit (I_{bit})

Figure 4.10 shows that I_{bit} increases linearly with discharge energy, from (10 \pm 2) μ Ns at 0.5 J to (41 \pm 5) μ Ns at 2.5 J. The values shown are averaging over 10 data points, and the error bars indicate twice the standard deviation. The specific impulse bit (or specific thrust), I_{bit}/E_0 obtained from the data in Figure 4.10 was 17 μ Ns/J. The impulse bit values reported in other PPTs of similar flared electrodes, side-fed propellant configuration falls within the trendline. Of the three references, Tran et al. (2019) used

tongue shaped electrodes. Clark et al. (2011) also showed a linear trend for a small range of E_0 from 0.6 to 2 J, and their I_{bit}/E_0 was 17 μ Ns/J. For much higher discharge energies up to 800 J, Gessini & Paccani (2001) showed a much higher I_{bit}/E of 38.6 μ Ns/J. Results on higher pressure (5×10⁻³ mbar) are added to show the comparison. I_{bit} on higher pressure also shows linear trend but with less steep gradient. At higher pressure, the ablated particles will lose energy when colliding with the background air molecules, hence producing less impulse. Furthermore, operating at high pressures will cause the breakdown of the discharge through residual air molecules inside the vacuum chamber, rather than the PTFE propellant, causing the efficiency to decrease as part of energy is not used to ablate the PTFE propellant.

It is noted that some applications of PPTs require extremely small and precise momentum change per pulse that is important for the fine tuning of the satellite's location or attitude to a fraction of a millimetre. Thus, small impulse bit capability of the PPT at low energy may be an advantage.

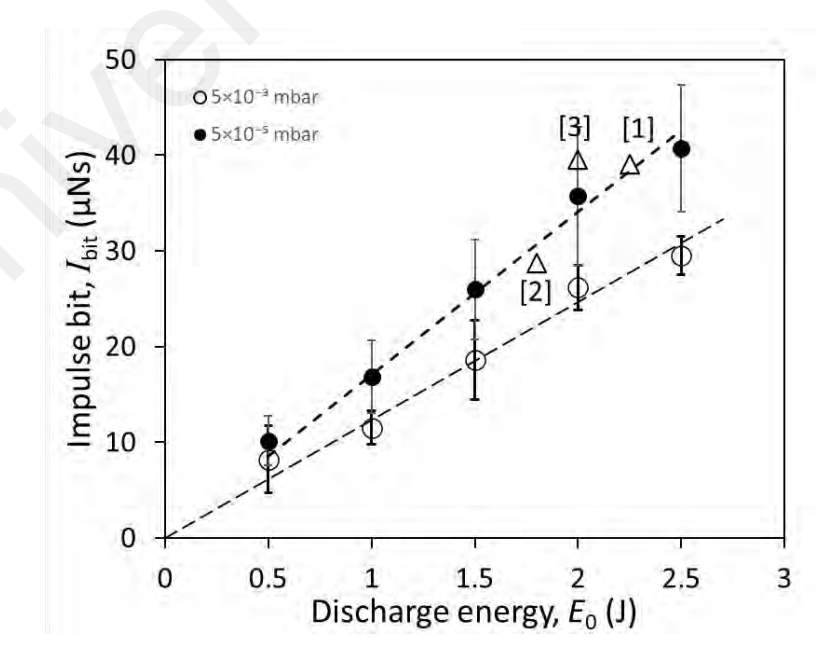


Figure 4.10: Impulse bit as a function of discharge energy. *I*_{bit} from similar flared electrodes, side fed PPTs (¹Tran et al., ²Clark et al., ³Ciaralli et al.) are included for comparison.

The combined effect from the electromagnetic impulse bit, $I_{\text{bit-em}}$ and the electrothermal component contributes to the total impulse bit (I_{bit}). $I_{\text{bit-em}}$ is due to the accelerating ions in the discharge plasma while the electrothermal component is contributed by the energetic neutral particles that are thermally expelled. $I_{\text{bit-em}}$ can be calculated from equation (4.1) below:

$$I_{\text{bit-em}} = \frac{L'}{2}\psi; \quad \psi = \int_0^\infty i^2 dt, \qquad (4.1)$$

where L' is the inductance variation per unit length in $\mu H/m$ and ψ is the current parameter in A^2 s. L' is dependent on the electrode geometry and its expression gets more complex when the electrodes are flared and tongue shaped; the mean change in inductance, $\Delta \bar{L}(x)$ at axial position x of the flared and tongue shaped section can be expressed as (Antropov, 2003)

$$\Delta \bar{L}(x) = \frac{\mu}{2\pi} \int_{x_1}^{x} f[x, w(x), h(x)] dx, \qquad (4.2)$$

where μ is the permeability, and both the width w(x) and gap height, h(x) being functions of the axial position. For a parallel rectangular geometry, L' can be calculated using the simple expression:

$$L' = 0.6 + 0.4 \ln \left(\frac{h}{w + t} \right), \tag{4.3}$$

where t is the thickness of the electrode and equation (4.3) is applicable for h/w > 1. To make an approximate calculation of L', the axial length is segmented into equal sections of axial length 0.1 mm, and L' is calculated for each section, of which each section will have a different h (due to flaring) and different h (due to tapering shape). A mean value of h' is estimated from these segments and is equal to h' is estimated from these segments and is equal to h' is estimate of 0.6 h' much for parallel rectangular electrodes.

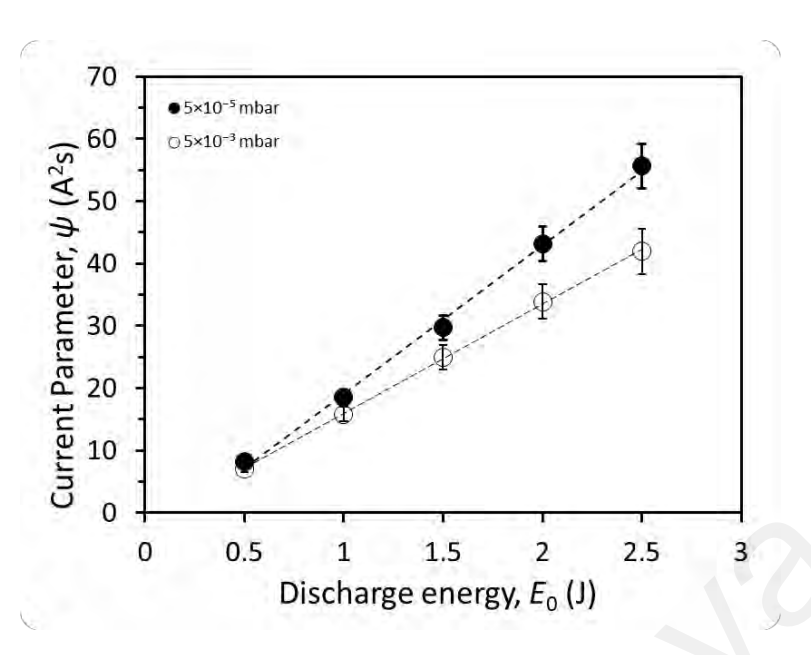


Figure 4.11: Current parameter (ψ) as a function of discharge energy.

The current parameter, ψ is calculated by discretely summing the area under the square of discharge current curve, i^2 and it is proportional to the discharge energy, E_0 . This linear relation can be fitted to a linear expression proposed by Palumbo and Guman (1976), $\psi = a(\sqrt{C/L_0})E_0$, where the multiplying coefficient a has been shown to have fitted values of around 2 (Clark et al., 2011). The fitted value for a using data of Figure 4.11 is 4.4 ± 0.1 . The difference in the fitted values of coefficient a could be attributed to the difference in the thruster design, whereby Palumbo and Guman's (1976) and Clark et al. (2011) are side-fed configuration with flaring rectangular electrodes while this work uses a side-fed configuration with tongue-flared electrodes.

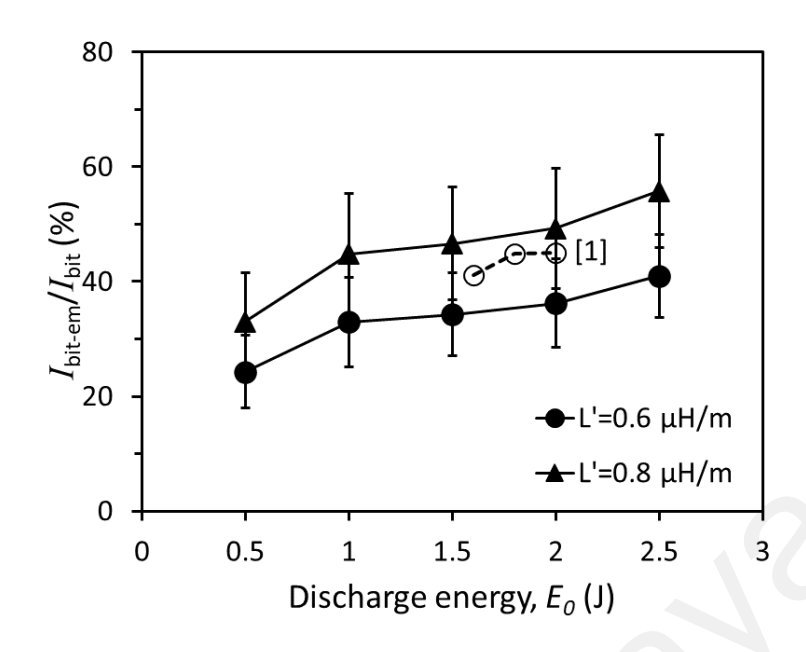


Figure 4.12: Percentage of $I_{\text{bit-em}}$ to total I_{bit} as a function of discharge energy for two different values of L'. For comparison, data (hollow circles) from Ref. [¹Clark et al] are included.

Figure 4.12 shows the ratio of $I_{\text{bit-em}}$ to I_{bit} in percentage. The upper curve took into consideration the flare and tapering (tongue shape) electrode geometry while the lower curve (dashed line) is determined for parallel rectangular electrodes. Within the discharge energy of 1 to 2.5 J, about 50% of the total impulse bit is contributed by the electromagnetic component. This is high as PPTs at energies below 20 J are known to be dominantly in the electrothermal mode, hence, $L' = 0.8 \,\mu\text{H/m}$ may be an over estimated value. Additionally, using an uncertainty contributed by one standard deviation from calculation of the average of L', the derived uncertainty for the ratio $I_{\text{bit-em}}/I_{\text{bit}}$ is approximately 25-50 %. The conservative value of $0.6 \,\mu\text{H/m}$ (non-flared and rectangular electrodes is assumed) yields the lower curve, demonstrating a reasonable amount of electromagnetic component of approximately 30%. In comparison, the ratio reported by Clark et al. (2011) for a parallel rectangular electrodes arrangement that flare outward from halfway on their axial length falls in-between the upper and lower curves. They had used $L' = 0.66 \,\mu\text{H/m}$. At the 0.5 J discharge energy, the ratio is much lower at 24% (at the lower curve), implying that the electrothermal component is the major contributor to

the impulse bit; and this means only a small portion of the ablated PTFE was ionized and converted to plasma thrust.

4.3.2. Mass Bit measurement (*m*_{bit})

The mass bit (m_{bit}) is a measure of the effect of ablated propellant in a single firing. The value for m_{bit} is determined from the reduction in mass of the solid PTFE propellant bar after 1,000 shots. As shown in Figure 4.13(a), m_{bit} increases linearly from 0.9 \pm 0.2 μ g to 4.9 \pm 0.2 μ g with respect to the discharge energy and can be fitted to a relation: $m_{bit} = 2.08E_0 - 0.14$. The values are lower than those published by in Refs. (¹Tran et al., ²Clark et al., ³Ciaralli et al.). But it follows the linear trend reported by (Schönherr et al., 2013) for a tongue-flared PPT (replotted in Figure 4.13(b)) that was operated at much higher capacitances (20- and 80-fold higher) or higher discharge energy. It is noted that the m_{bit} reported in the most literature is for energies around 2 J and above. Results of m_{bit} at higher pressure (5×10⁻³ mbar) were added to make comparison, m_{bit} increases exponentially from 0.5 \pm 0.2 μ g to 4.8 \pm 0.2 μ g with respect to the discharge energy, and can be fitted to a relation: $m_{bit} = 0.23 \exp(1.2E_0)$.

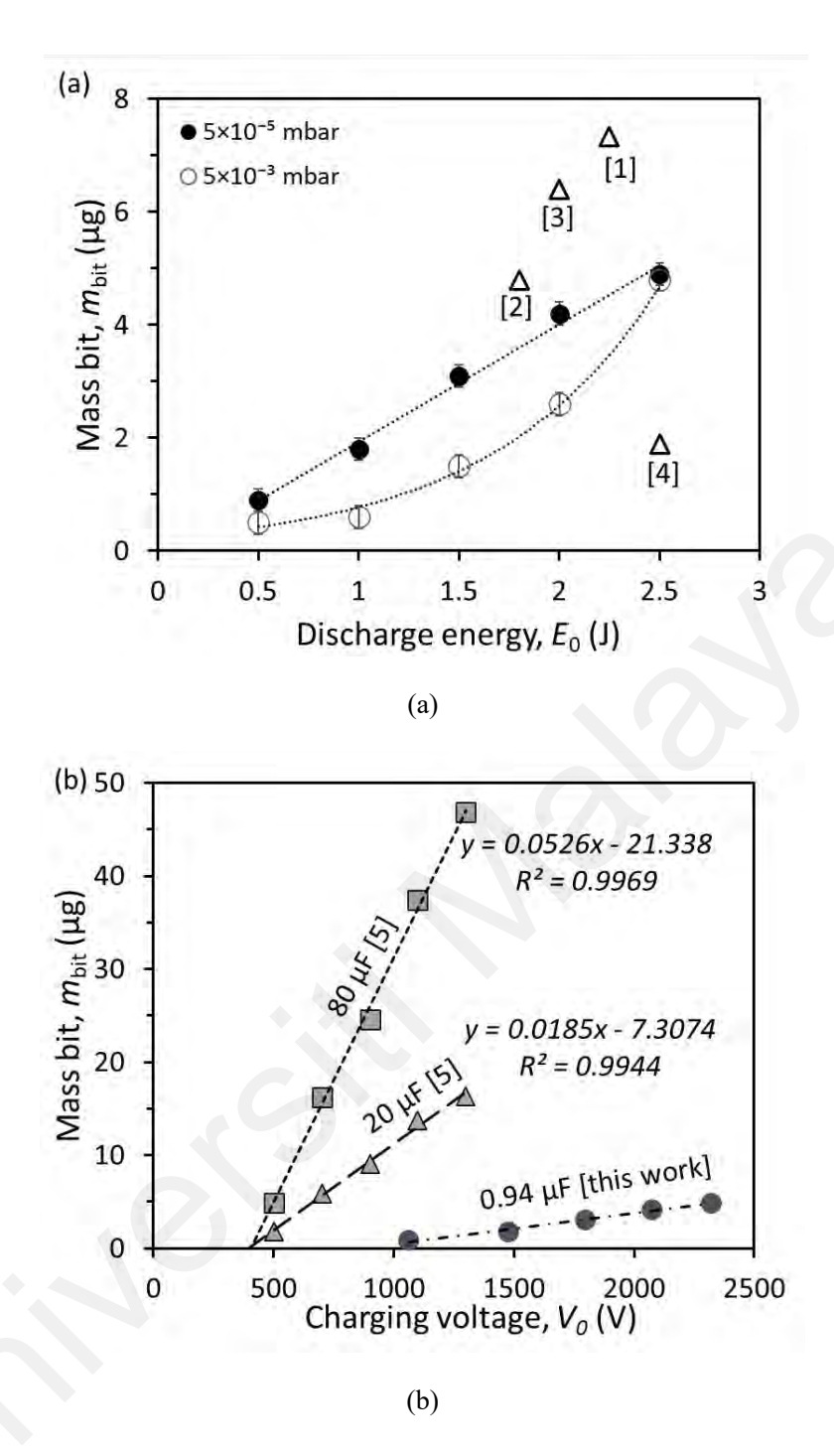


Figure 4.13: Mass bit (*m*_{bit}) as a function of (a) discharge energy and (b) charging voltage. Data from similar flared electrodes, side fed PPTs (¹Tran et al., ²Clark et al., ³Ciaralli et al., ⁴Schönherr et al., ⁵Gessini & Paccani) are included for comparison.

4.3.3. Specific impulse (I_{sp})

The specific impulse (I_{sp}) measures how efficiently the thrust is created by the PPT, and a higher specific impulse means that the mass of the ablated propellent is more efficiently used for propulsion. It is calculated using the expression (in units of s):

$$I_{\rm sp} = \frac{I_{\rm bit}}{m_{\rm bit}g_0} \tag{4.4}$$

where g_0 is the gravitational acceleration. Figure 4.14 plots I_{sp} versus the discharge energy per area of the propellant exposed to the discharge, E_0/A , and compared to the semi-empirical specific impulse relations, $I_{\rm sp}=504(E_0/A)^{0.40}$ by Gessini and Paccani (2001) for side-fed type and $I_{\rm sp}=317(E_0/A)^{0.585}$ by Guman (1975) for all different geometries of propellant-feed. At E_0/A below 2 J/cm², the specific impulse values are about 2 to 3 times higher than those predicted by Gessini & Paccani (2001). I_{sp} is a derived value from two independently measured parameters, I_{bit} and m_{bit} . Especially at the very low discharge energy (also lower voltage), it is speculated that the arc discharge is weak and may not have been formed directly over the propellant surface leading to relatively much lower liberated PTFE mass, and the deposition of the carbon back flux from the plasma may be relatively higher. Hence, a much lower mass loss is measured leading to a derived value for I_{sp} that is much higher than those predicted by both the semi-empirical relations. Above 1.5 J/cm^2 , the I_{sp} values are consistent with those estimated from the semi-empirical relation. It is possible that when at lower discharge energy, the effective area is also lower, thus the data points of the specific impulse would be occurring at higher E_0/A .

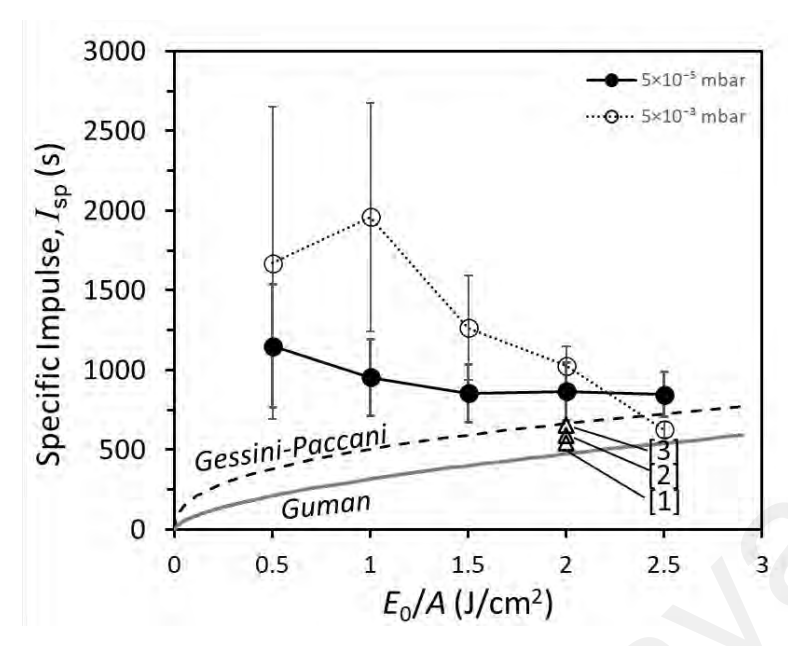


Figure 4.14: Specific impulse (I_{sp}) as a function of discharge energy/exposed area of propellant. I_{sp} from flared electrodes, side fed PPTs [1 Tran et al., 2 Clark et al., 3 Ciaralli et al] are included for comparison.

4.3.4. Mean exhaust velocity

The mean exhaust velocity c_e represents the average velocity of all ablated mass bit and is determined from the expression

$$c_e = \frac{I_{\text{bit}}}{m_{\text{bit}}} \,, \tag{4.5}$$

The variation of c_e with discharge energy is shown in Figure 4.15. Like the case in the determination of I_{sp} , c_e is also a derived value from the two independently measured I_{bit} and m_{bit} , and larger value of c_e at the lower discharge energies with high uncertainty level is presented.

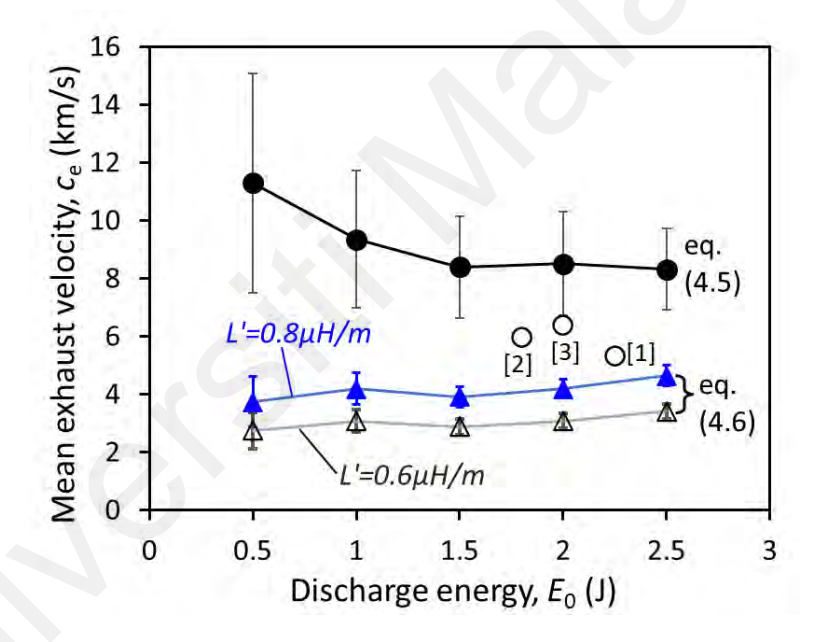


Figure 4.15: Mean exhaust velocity (c_e) as a function of discharge energy determined from equations (4.5) and (4.6). [¹Tran et al., ²Clark et al., ³Ciaralli et al] are included for comparison.

Assuming that entire mass bit $m_{\rm bit}$ to be uniformly accelerated as in a 'slug' model, and that the change of inductance with axial position (dL/dx = L') of the plasma layer is also constant, the mean exhaust velocity $c_{\rm e}$ can then be approximated through an alternative expression

$$c_e \cong \dot{x} = \frac{1}{2m_{\rm bit}} L' \psi , \qquad (4.6)$$

The two values of L' (0.6 and 0.8 μ H/m) are in equation (4.6). Both give a lower mean exhaust velocity, below 5 km/s which is of the same order of magnitude to other published data, e.g., Koizumi et al. reported c_e of 7.5 km/s for a 7.4 J ablative PPT of rectangular, breech-fed electrode configuration. When compared to side fed PPTs (about 2 J) of Tran et al., Clark et al., and Ciaralli et al., c_e from equation (4.6) matches their values. The mean exhaust velocity is the average of a slow-moving component contributed by the neutral particles in the exhaust plasma plume and a much faster component (several times higher in speed) contributed by the ions that are accelerated by the Lorentz force (Koizumi & Noji 2007). The determination of the faster component in terms of 'fastest' ion velocity is discussed below.

4.3.5. 'Fastest' ion velocity

Upon exiting the PPT channel, the plasma plume has been observed to continue accelerating further downstream. In this work, the 'fastest' ion velocity (i.e. velocity of ions at the leading-edge of the downstream plasma plume) is determined from the plasma transit time from the PTFE target where surface discharge was first initiated to the position of the Triple Langmuir probe placed external to the PPT channel, that is, $x \ge 25$ mm, where x = 0 is at the plane of the PTFE propellant and x = 25 mm is at the exit plane of the thruster. Measurements were made up to 30 mm downstream from the exit plane. In the plasma plume of PPT, there are different ion species with different ionization states (CII, CIII, FII, FIII, etc.), each species experiences different acceleration due to different mass and charge. The probe current is contributed by all these ions. Thus, instead of using the peak of the probe current for time-of-flight measurements, the arrival time of the fastest ion species was used for the velocity measurement, as it is more reliable and yet able to show the changes when discharge energy is varied.

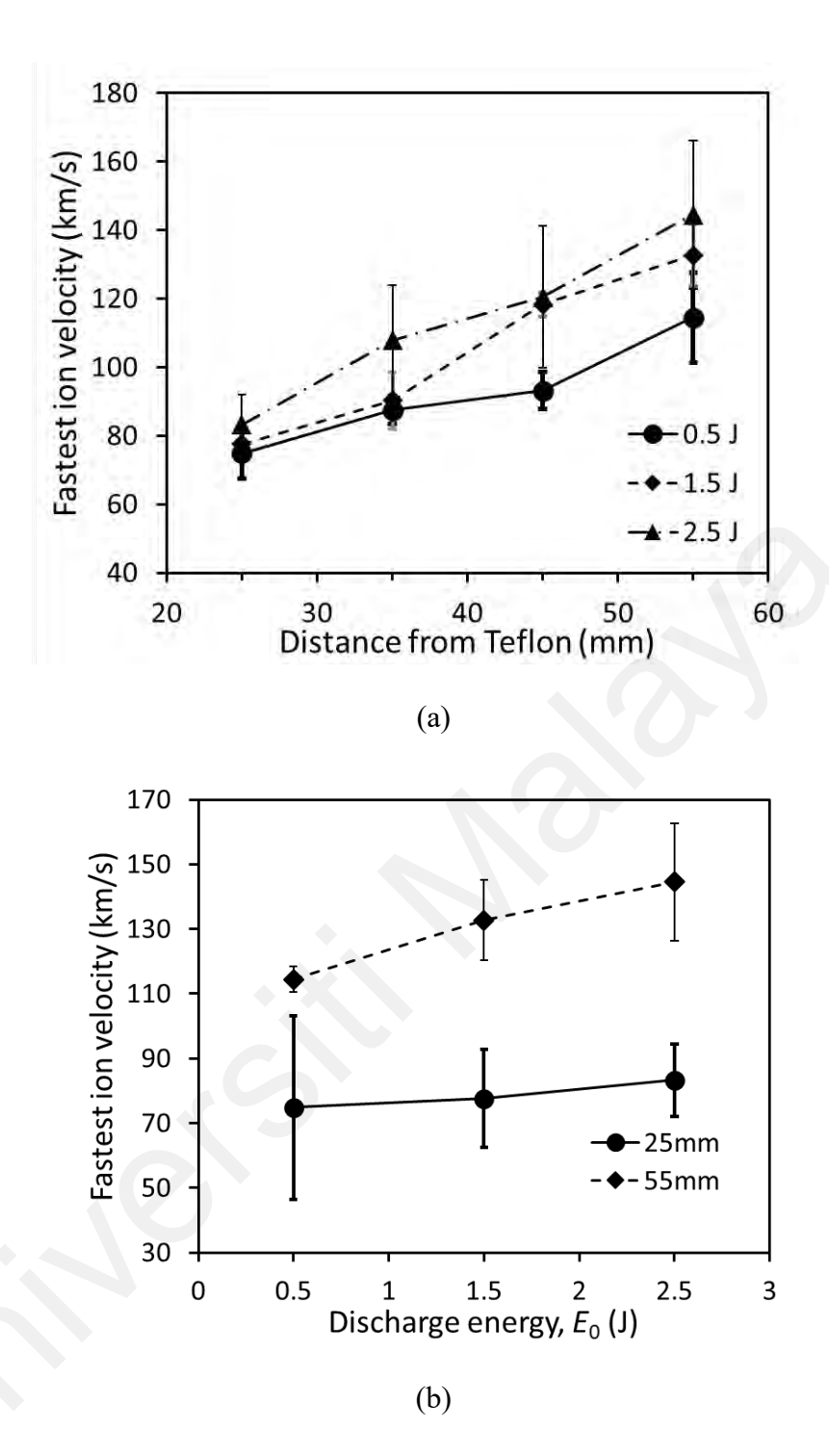


Figure 4.16: 'Fastest' ion velocity at (a) different distance from PTFE surface, and (b) at different discharge energy.

From Figure 4.16, all energies show the trend of ions acceleration along the downstream direction. This is evident from the increase in velocity from 71 km/s and 83 km/s at 25 mm to 114 km/s and 145 km/s at 55 mm, respectively for discharge energy of 0.5 J and 2.5 J (Figure 4.16(b)). The ions seem likely to continue accelerate further downstream, but it was not possible to measure beyond x = 55 mm due to the limited size

of the vacuum chamber. Similar trend was observed by Ling et al. (2017) and they recorded a highest velocity of 81 km/s at 140 mm from the exit plane of a 9.8 J PPT. As the discharge energy is increased, the ions in the plasma plume gain higher kinetic energy, hence, the 'fastest' ion velocity increases. The plasma plume of the PPT exiting the thruster channel consists of energetic electrons and multiple species of ions with different ionization energies. The much lighter electrons attain significantly larger velocity leaving the ions behind, and this possibly resulted in ambipolar diffusion that acts on the ions and accelerating them. Therefore, the velocity of the 'fastest' ion would be higher than the average ion exhaust velocity within the PPT channel; Koizumi et al. (2007) deduced this value to be 10-20 km/s from high-speed camera imaging of the C⁺ emission line of the plasma plume.

4.3.6 Thrust efficiency (η) calculation.

There are different terms used by researchers to describe the efficiency of the PPT, such as overall efficiency (the fraction of energy supplied to the power processing unit that is converted to kinetic energy), transfer efficiency (the fraction of energy stored in the capacitor that is delivered to the discharge), and propellant utilization efficiency (the ratio of ionized mass to total mass bit). In this work, thrust efficiency is used, which is defined as the ratio between the kinetic energy of the plasma plume and the energy stored in the capacitor. The thrust efficiency, η is calculated using the relation that involves only the independently measured impulse bit ($I_{\rm bit}$), mass bit ($m_{\rm bit}$) and the discharge energy (E_0) (Burton et al.1998),

$$\eta = \frac{I_{\text{bit}}^2}{2m_{\text{bit}}E_0},\tag{4.7}$$

and the approximated expression from the 'slug' model consideration

$$\eta = \frac{1}{8m_{\rm bit}E_0} L'^2 \psi^2, \tag{4.8}$$

For equation (4.8), two values of L' (0.6 and 0.8 μ H/m) are used in the calculation, and the plots are shown in Figure 4.17. The thrust efficiency calculated from equation (4.7) is higher than those determined using equation (4.8). Comparing to values reported by others (Tran et al., Clark et al., and Ciaralli et al) for discharge energies in the vicinity of 2 J, the values calculated from equation (4.7) are more consistent. Data from published literature showed the thrust efficiency to increase with discharge energy (capacitor bank energy) (Molina-Cabrera P, et al. 2011). the thrust efficiency is about 7 % for energy from 1 J to 2.5 J. The high efficiency for 0.5 J is possibly due to different discharge mechanism.

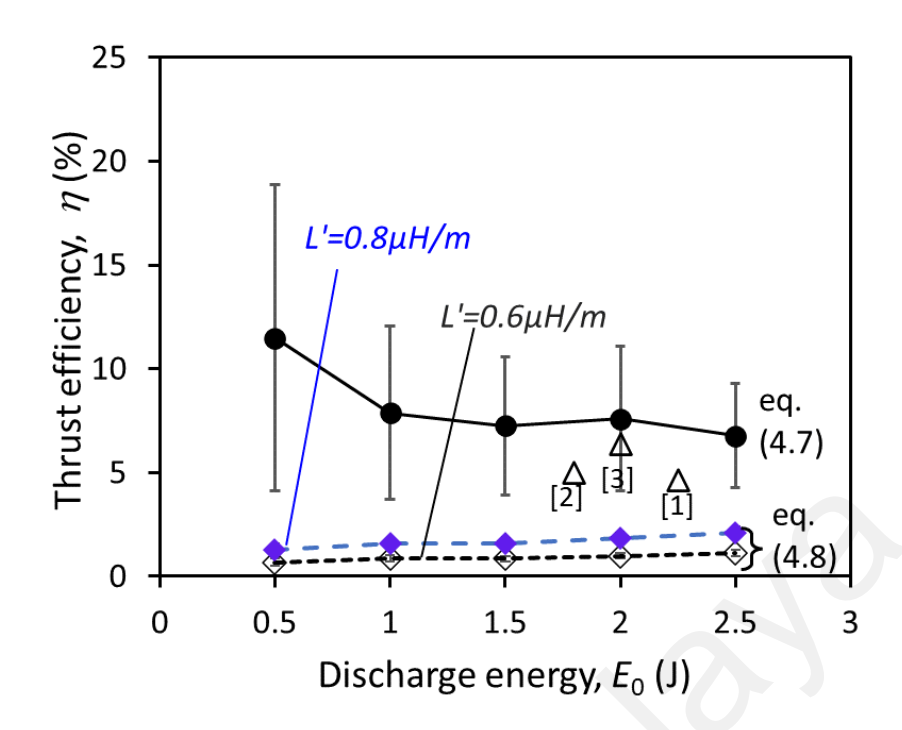


Figure 4.17: Thrust efficiency η of PPT for discharge energy from 0.5 to 2.5 J. η from similar PPTs of flared electrodes, side-fed propellants are included for comparison. [¹Tran et al., ²Clark et al., ³Ciaralli et al] are included for comparison.

4.4 Surface erosion and fuel consumption

Evidence of ablation is visible as eroded area on the propellant surface after 10^3 - 10^5 of discharge firings. The images can qualitatively represent some of the discharge features such as its structure and strength of the discharge (Keidar et al., 2004). The 'black' areas are due to charring, possibly due to carbon back flux from the plasma as reported by Keidar et al. (2004). Figure 4.18 shows that at 2.5 J, there is an uncharred area (whitish) whereby the PTFE propellant gets ablated and ejected. The uncharred region is smaller at lower energy indicating less ablation has taken place. At the lowest energy of 0.5 J that produced the lowest discharge current, the charring occurred over the entire PTFE surface that faces the discharge. The lighter colour tone indicates a less thick charred layer relative to those at the higher discharge energies. This suggests that there might be a change in discharge mechanism or due to incomplete decomposition of PTFE. This is consistent with the lowest ratio of I_{bit-em} to I_{bit} as compared to those at higher discharge energy. Conversely, discharge at higher discharge energy produces higher current leading to higher surface temperature of the PTFE propellant bar, enhancing the ablation rate (Keidar et al. 2001).

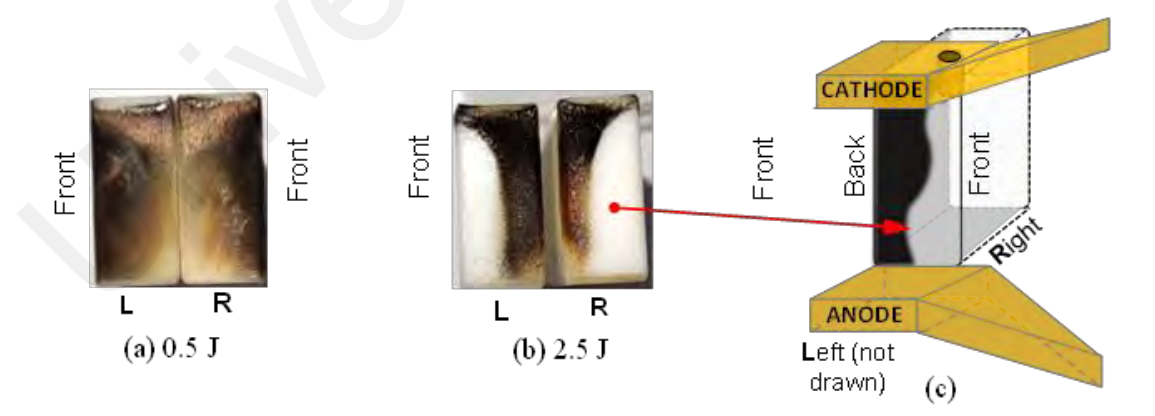


Figure 4.18: Discharge-induced surface erosion on the PTFE propellant bar after 1,000 shots fired at (a) 0.5 J, (b) 2.5 J, and (c) Placement of the propellant bar (only the right side is drawn) with respect to the electrodes.

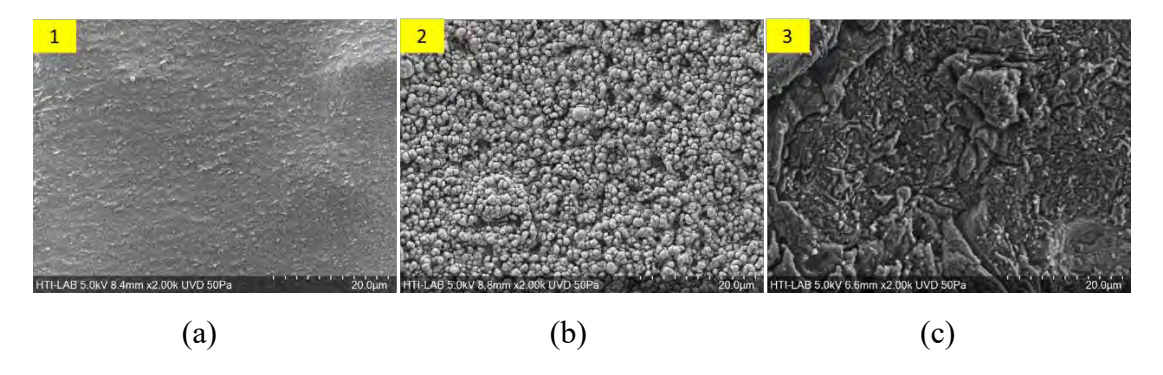


Figure 4.19: FESEM image of PTFE propellant surface at different regions after 1000 shots fired at 0.5 J and 2.5 J. The respective eroded and charred regions for 2.5 J are marked as (1) and (2), while (3) marks the charred region for 0.5 J.

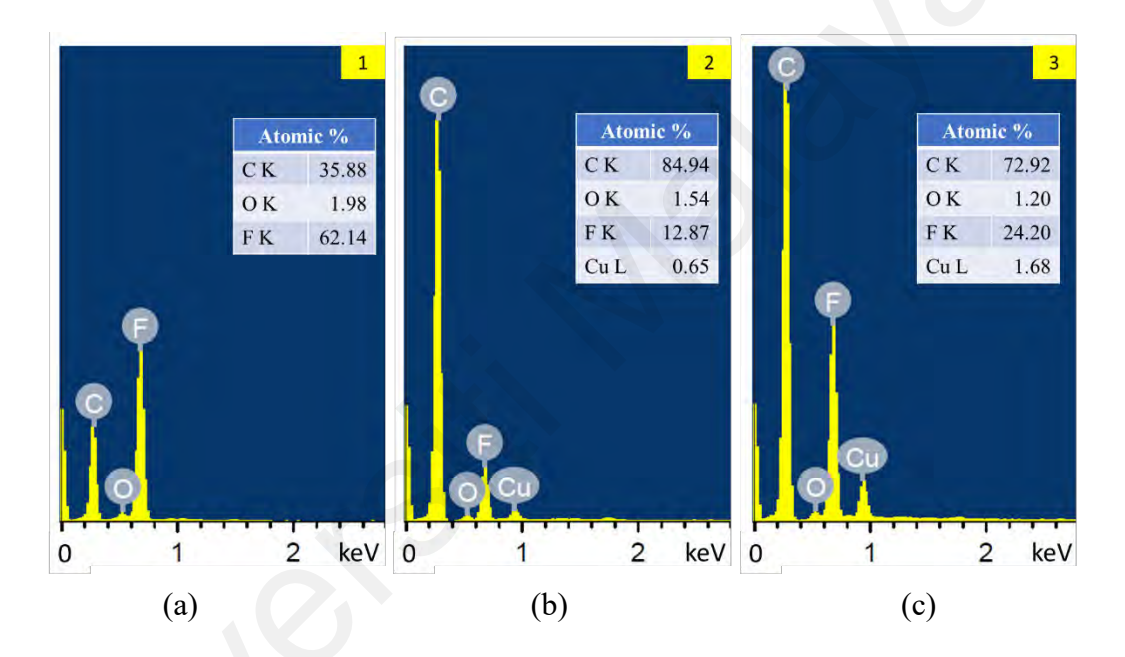


Figure 4.20: FESEM EDX spectra measured at the sampled regions (a) '1' and (b) '2' and (c) '3' of Figure 4.19.

Figure 4.19 shows the FESEM imaging of the PTFE surface after 1000 shots fired at discharge energy of 0.5 and 2.5 J. There is a difference between the images of 0.5 J and 2.5 J, although they are both charred area (Figure 14.19b and 14.19c), Figure 14.19(b) shows globular structure while Figure 14.19(c) shows non-uniform structure. EDX spectrum in Figure 4.20(a) shows that the eroded area at 2.5 J contains mainly fluorine (62.14 at%) and carbon (35.98 at%) with a ratio \approx 2 that corresponds to the stoichiometric ratio of PTFE, (C_2F_4)_n. Oxygen is likely from moisture in residual air in the evacuated chamber or deposition when exposed to the air . Figure 4.20 (b) shows that the charred

region contains mostly carbon (84.94 at %), followed by fluorine (12.87 at %), oxygen (1.54 at %), and trace amount of copper (0.65 at %). The copper peak indicates copper sputtering to have occurred during the discharge, and this indicate that copper electrodes are eroded during discharge. The globular structures are similar to those shown by Keidar et al. (2004) in a 1 and 3 J coaxial micro-PPT. These structures suggest that the carbon char is formed due to carbon deposits from the plasma rather than the incomplete decomposition of PTFE propellant (Keidar et al. 2004). It is expected that F ion density exceeds that of C ion in the plasma plume arising from their stoichiometric composition in PTFE, but the heavier F ions being less mobile led to its lower amount in the char relative to C ions. Figure 4.20(c) shows the charred area for discharge energy of 0.5 J, the peaks are similar to Figure 4.20(b), but the C/F ratio is less than that in Figure 4.20(b), 3 and 6.6 respectively. The difference in the ratio could be the hints that indicate the incomplete decomposition of PTFE propellant at low discharge energy. Together with the structural differences observed in the FESEM images, it is postulated that discharge mechanism has change when the discharge energy is low.

Increasing discharge energy raises the PTFE surface temperature leading to enhanced PTFE ablation and also the carbon char ablation, hence, preventing char formation. From the partially ablated surface area observed, it is likely that the discharge is not uniformly distributed over the entire exposed propellant surface, that is, heating of the surface is also not uniformly distributed. A simulation by Keidar et al. (2004) in a coaxial PPT showed that current density peaks near the electrode whereby PTFE surface temperature is increased near the electrode; this led to more PTFE being ablated near the electrode since the ablation rate is exponentially proportional to the surface temperature. The carbon deposition has a significant impact on the lifetime of the thruster because it can cause short circuit between anode and cathode. At the boundary between the charred and

eroded areas, some tubular structures are formed on the surface (Figure 4.21). It is speculated, albeit inconclusively, that formation of these structures might be aided by the interplay of forces arising from plasma dynamics and the carbon back flux during the discharge.

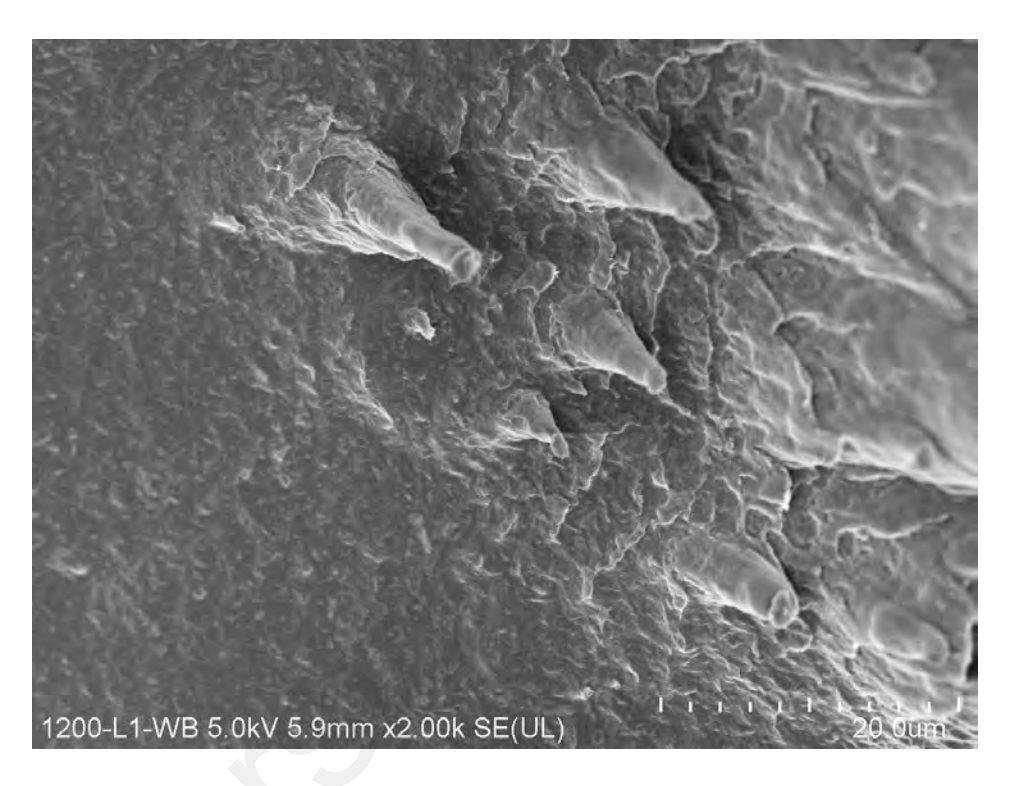


Figure 4.21: FESEM image of PTFE propellant surface at the boundary between the charred and eroded areas

4.5 Comparison with other pulsed plasma thrusters (PPTs)

Table 4.3 provides a comparison of the impulse bit (I_{bit}), specific impulse bit (I_{sp}), and thrust efficiency (η) of various PPTs, both the flared (both tongue and rectangular shaped) and plane-parallel electrodes configurations, within the discharge energy range of 1.8 to 8.5 J. Some of these PPTs have been used in actual space flight application. The dependence of I_{bit} , I_{sp} and η on the discharge energy is plotted in Figure 4.22. Larger deviation range is observed to occur in the I_{bit} , I_{sp} and η for the PPTs of plane-paralell electrode configurations other than the flared type (the dashed lines/curves are drawn as a visual guide that depicts the approximate upper and lower boundaries of the variation range). I_{bit} exhibits an approximate linear increase with the discharge energy as shown in Figure 4.22(a), within its variation range. Variation in I_{sp} is much larger at the lower end of the discharge energy range and narrows down as the energy increases (Figure 4.22 (b)).

Table 4.3. Comparison of the performance parameters of various PPTs. n/s means not stated.

Electrode Configuration	Energy (J)	Impulse bit, I _{bit} (µNs)	Specific Impulse, I _{sp} (s)	Mass bit, m _{bit} (μg)	Thrust efficiency, η (%)	Status	
Tongue-flared electrode (*rectangular- flared)	2.0	26	1027	2.6	6.6	Lab	
	2.5	30	627	4.8	3.6		
	1.8	31	590	4.8	5	Lab	
	2	38	608	6.4	5.8	Lab	
	2.25	39.1	543	7.34	4.6	Flight	
Plane-parallel electrode	1.85	27	300	n/s	2	Flight	
	2.25	29.5	300	10	2	Flight	
	2.37	16.5	927	1.78	3.2	Lab	
	2.6	40	608	n/s	4.9	Lab	
	4	63	280	25	2	Flight	
	4.2	25	800	13	2.3	Flight	
	4.9	66	266	25.4	1.8	Lab	
	5	40	450	7	n/s	Flight	
	6.6	112	613	n/s	5.6	Flight	
	8	88	530	17	3	Lab	
	8.4	122	405	n/s	3.7	Flight	
	8.5	90	650	n/s	8	Flight	

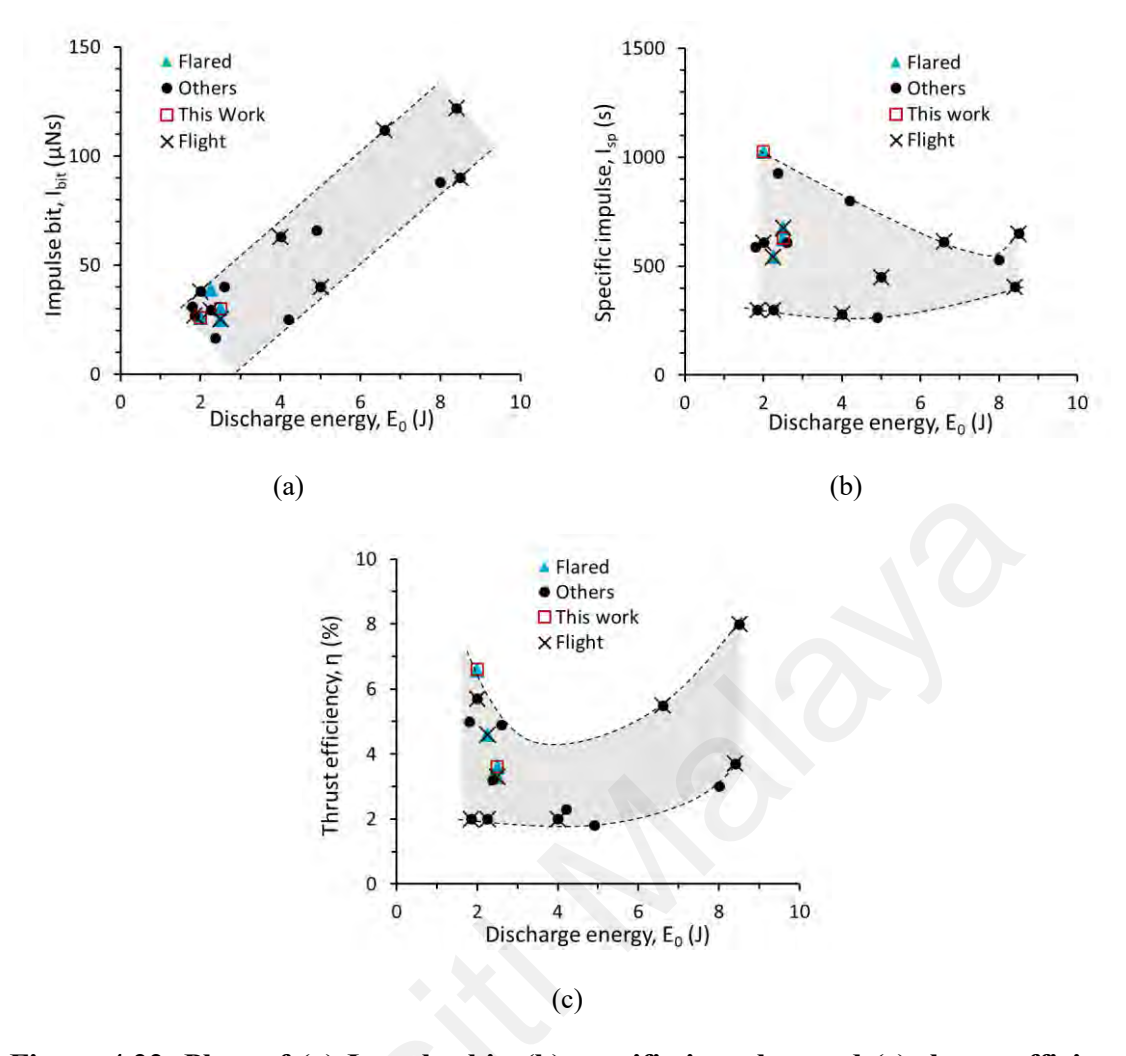


Figure 4.22: Plots of (a) Impulse bit, (b) specific impulse, and (c) thrust efficiency with respect to discharge energies for the PPTs listed in Table 4.3.

Thrust efficiency, η , falls between (2-8) %, but tends to be on an increasing trend for energy >8 J (Figure 4.22(c)). Some possible reasons for the large deviations in Figure 4.22 may be due to differences in (1) system design, (2) electrode dimension, (3) propellant bar configuration, (4) exposed area of propellant, (5) impedance matching, and (6) quality of capacitor. It was reported that m_{bit} was affected by the exposed surface area of propellant (Nawaz, et al. 2010). PPTs with tongue-flared electrode configuration exhibits slightly better and consistent thrust efficiency of above 4%. Although the thrust efficiency is expected to increase with higher discharge energy, a low m_{bit} and low current when operated at the low discharge energy range could introduce less losses due to ohmic heating. Using a tongue-flared electrode configuration, a greater change in inductance per

unit length of the plasma position can occur (Schönherr, et al. 2009). Therefore, the combined effect is an improvement in thrust efficiency.

Within the low discharge energy (E_0) range of 0.5 - 2.5 J of a tongue-flared PPT, the impulse bit I_{bit} increased slower at a specific impulse bit of 12 μ Ns/J than that of PPTs at higher energies. The electromagnetic component ($I_{\text{bit-em}}$) that contributes to the I_{bit} was about 55 % for E_0 of 1-2.5 J when a higher change in inductance with position (L') with the tongue-flared electrodes was considered; and dropped to 35% at the 0.5 J. These values are higher than those reported in similar PPTs at 1.6-2 J. Low mass bit $m_{\rm bit}$ was obtained, and it increased non-linearly with the charging voltage unlike those reported for higher energy PPTs with much larger (20 and 80 times more) capacitor banks. With reference to the degradation of PTFE surface, it was speculated that especially at the low end of the energy range investigated, charring rate may have exceeded the less extensive ablation of the propellant and could have resulted in the extremely low mass bit measured. At higher energy \geq 2J, the discharge striking across the electrodes is stronger and ablation rate is higher than the charring rate and reasonable $m_{\rm bit}$ could be measured. Owing to the low mass bit, the derived values of specific impulse I_{sp} were 4 to 2 times higher especially at $E_0/A < 2$ J/cm² than those predicted by a semi-empirical formula of Gessini-Paccani. Likewise, the mean exhaust velocity c_e as well as the thrust efficiency η , both derived using values of $m_{\rm bit}$, also recorded a higher value especially at the low end of the discharge energy range albeit with large uncertainties (60 to 70% at 0.5 J) and reduced as discharge energy was increased which is contrary to intuition. At discharge energy around 2 J, c_e and η were closer to values published in references (Tran et al, 2009, Clark et al, 2011, Ciaralli et al, 2016). Using another method (independent of the measured m_{bit}) that employed the triple Langmuir probe to determine the 'fastest' ion velocity at the downstream locations external to the PPT channel, this velocity increased with discharge

energies at the exit plane of the PPT channel which is to be expected. Although the 'fastest' ion velocity is not equal to the mean ion exhaust velocity and the mean exhaust velocity, the trend can still be representative of that in the mean exhaust velocity; and this seemingly contradicts the trend observed for $c_{\rm e}$. The increase of 'fastest' ion velocity with distance downstream indicates acceleration of ions outside the PPT channel, possibly to have been aided by ambipolar diffusion. Analysing the elemental component of charring on the propellant surface, the highest proportion was C (77 at%), trailed by F (16 at%) with traces of Cu from the electrodes. The globular structures and the EDX spectrum suggest that char was formed from carbon back flux from the plasma rather than incomplete decomposition of the propellant. Comparing to published data (gathered from various PPTs of 1.8-8.5 J with tongue-flared, rectangular-flared and plane-parallel electrodes), wider spread in values of I_{sp} and η at the low energy end could be seen, or in other words, higher inconsistency in some performance parameters of the PPTs is likely to occur here similar to our observation. This could be due to the weaker discharge that did not get distributed over the entire exposed surface of the propellant and relatively 'excess' charring that led to a smaller mass bit measured.

4.6 Summary

In the first part of this chapter, after taking all factors into account, the KEMET capacitor (F464-AK9) has demonstrated its suitability for use in the PPT system, it gives consistence output and durable. The voltage and the current waveforms were observed to be very reproducible. Other capacitors have failed to attain a satisfactory $I_{\rm bit}$ value. The primary drawback of the KEMET capacitor is its considerable mass and large inductance.

The impulse bit shows linear trend with discharge energy, from (10 ± 2) µNs at 0.5 J to (41 ± 5) µNs at 2.5 J and the impulse bit of PPTs reported by other researchers falls within the vicinity of this linear trendline. For the ratio of I_{bit-em} to I_{bit} , the results for discharge energy above 1J are almost constant but for discharge energy of 0.5 J, the ratio is much lower indicated that that the electrothermal component is the major contributor to the impulse bit and only small portion of ablated PTFE was ionized. The $m_{\rm bit}$ increases linearly from $0.9 \pm 0.2 \,\mu g$ to $4.9 \pm 0.2 \,\mu g$ corresponding to discharge energy of 0.5 and 2.5 J of discharge energy respectively. At the very low discharge energy, the arc discharge is weak and may not have been formed directly over the propellant surface leading to relatively much lower liberated PTFE mass, and the deposition of the carbon back flux from the plasma may be relatively higher. Hence the value for I_{sp} that is much higher than those predicted. However, above 1.5 J/cm², the I_{sp} values are consistent with those estimated. The results of the fastest ion velocity shows that ions continue to accelerate further downstream due to ambipolar diffusion. Using a tongue-flared electrode configuration, a greater change in inductance per unit length of the plasma position can occur, therefore, it shows improvement in thrust efficiency.

CHAPTER 5: PLASMA CHARACTERIZATION OF PPT

5.1 Introduction

First section of this chapter discusses about the electrical characteristics of pulsed plasma thruster such as discharge voltage and current. The second part of the chapter presents data on electron temperature and density, which were obtained using a triple Langmuir probe, considering three different aspects: the center axis, parallel plane, and perpendicular plane. Subsequent sections involve identifying plasma species through optical emission spectroscopy. Finally, the last section involves comparing the findings presented in this chapter with those from other previously published research.

5.2 Electrical Characteristic of Pulsed Plasma Thruster

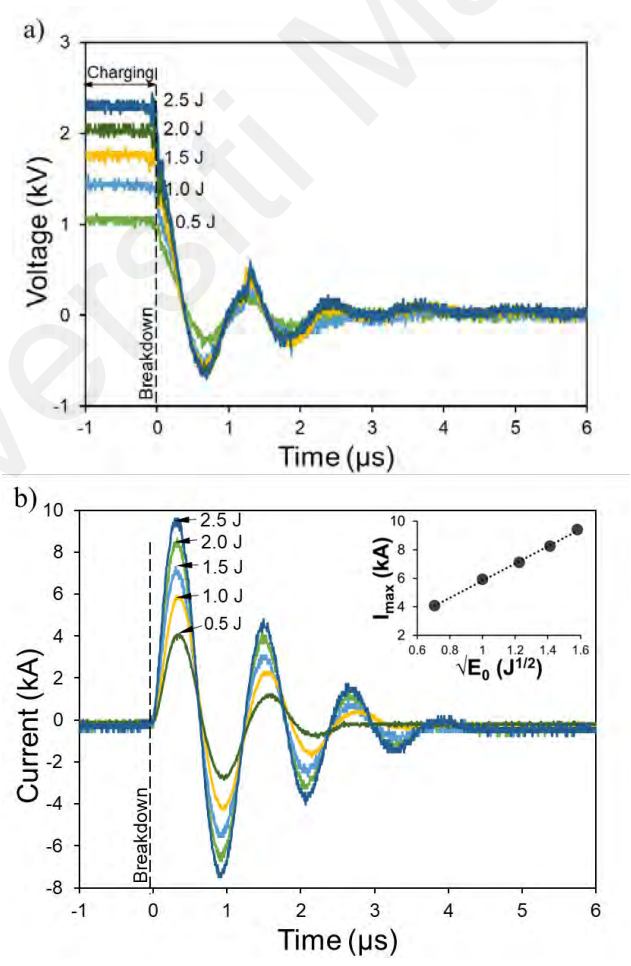


Figure 5.1: (a) Discharge voltage measured across the electrodes, and (b) discharge current for different discharge energies. Inset shows plot of current maximum (first current peak) versus the square root of discharge energy.

Figure 5.1 shows the typical voltage and current waveforms from PPT operation at different discharge energies between 0.5 and 2.5 J. As expected, the discharge current increases with increasing discharge energy, from 4.07 kA at 0.5 J to 9.41 kA at 2.5 J. The voltage and the current waveforms were observed to be very reproducible. It is also noted that irrespective of the discharge energy, the oscillation period of the voltage waveform remains constant at 1.22 ± 0.01 µs. Here, the plasma resistance is assumed to be negligible, but the period may depend on the initial inductance L_0 according to the simple relation, $2\pi\sqrt{L_0C}$ (Nawaz et al., 2010). From this, the approximated value of L_0 is 40 nH. A constant period implies that the time length of exposure of the PTFE surface to the current and the radiation from the plasma sheet are the same for the different discharge energies. Likewise, the position of the current density maximum along the electrodes is expected to be the same at the different energies. The inset plot of the current maximum I_{max} shows a linear relationship to the square root of discharge energy, E_0 as described by equation (5.1) below.

$$I_{\text{max}} = \sqrt{2E_0/L} \exp\left[-\frac{\pi R}{4}\sqrt{C/L}\right],\tag{5.1}$$

where R and L are the mean resistance and inductance respectively (Ling et al.,2017). The capacitance is fixed, and the inductance can be assumed to stay constant since the position of the maximum current is the same. The maximum current may be taken to represent the ablation rate of the propellant although the waveform is oscillatory, and it is usually occurring in low power PPTs because of the small capacitance (Schönherr et al., 2010). Figure 5.2 shows the actual image of PPT discharge.

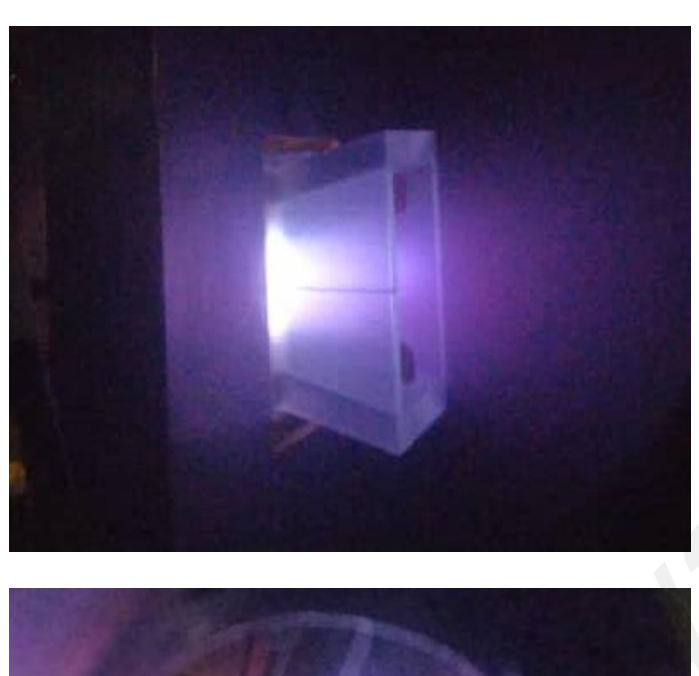




Figure 5.2: Images of PPT discharge

5.3 Electron temperature and density

This section includes analysis of the electron temperature, T_e and density, n_e of plasma plume as a function of discharge energy (ranging from 0.5 to 2.5 J), distance from PTFE (d=25mm to 75mm) and measurement plane (along the center axis, parallel and perpendicular planes). This provides an overall picture of the variation in electron temperature (T_e) and density (n_e) of the plasma plume as it expands from the PPT and allows detailed exploration of how electron temperature and density vary in different spatial directions.

5.3.1 Electron temperature and density along the center axis

A set of typical temporal behaviours of electron temperature and density of center axis are shown in Figure 5.3 and 5.4, where the electron temperature is denoted as $T_{\rm e}$, and the electron density as $n_{\rm e}$. These are calculated, after software smoothing to remove high frequency noise, from the triple-probe voltage and current signals using equations (3.17) and (3.18). The bumps

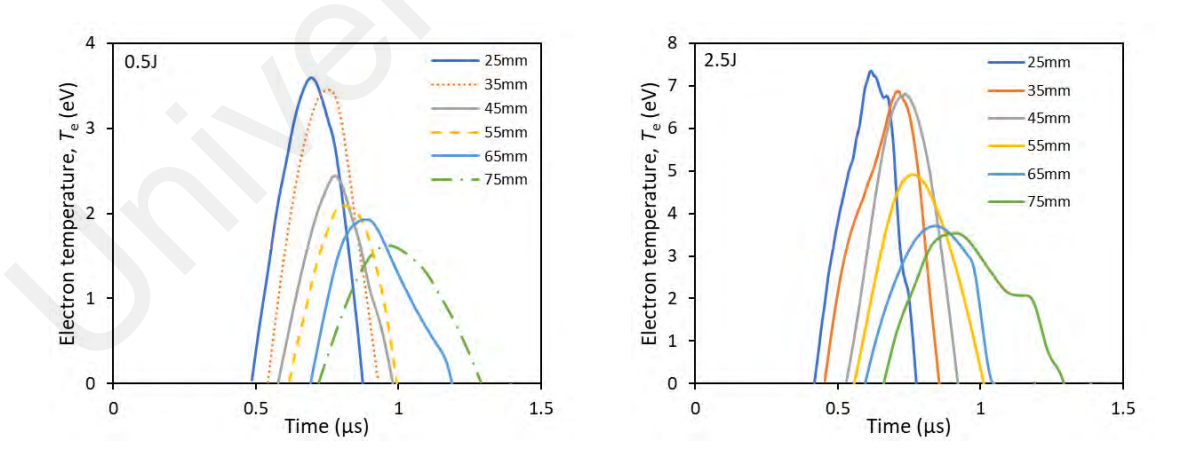


Figure 5.3: Time-varying electron temperature, T_e measured at different points along the center axis (angle = 0°) for discharge energy of 0.5 and 2.5 J.

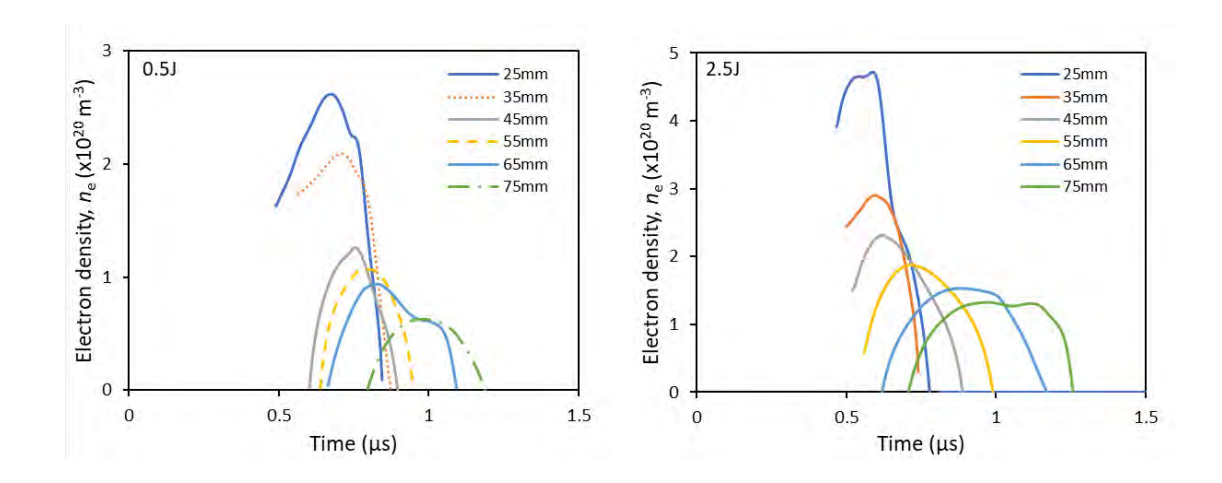


Figure 5.4: Time-varying electron density, n_e measured at different points along the center axis (angle = 0°) for discharge energy of 0.5 and 2.5 J.

As expected, the electron temperature decreases as the plasma expands into the surrounding and cools down as it propagates downstream. Figure 5.3 shows the time-varying profile of electron temperature, T_e , which cover distance from 25mm to 75 mm. For discharge energy of 0.5 J, T_e drops from 3.58 eV to 1.62 eV. For 2.5 J of discharge energy, the value of T_e is much higher, T_e drops from 7.34 eV to 3.53 eV as the plasma propagates from 25mm to 75mm. Figure 5.4 shows electron density n_e profiles along the center axis. For discharge energy of 0.5 J, the electron density, n_e at d=25 mm was 2.60× 10^{20} m⁻³ and as the plasma propagated beyond the flared region, the electron density dropped with increasing distance from the PTFE surface. At d=75 mm, it dropped by almost one order of magnitude, to 6.30×10^{19} m⁻³, over 50 mm of distance. For discharge energy of 2.5 J, n_e at d=25 mm was 4.67×10^{20} m⁻³ and it decreases to 1.35×10^{20} at d=75 mm.

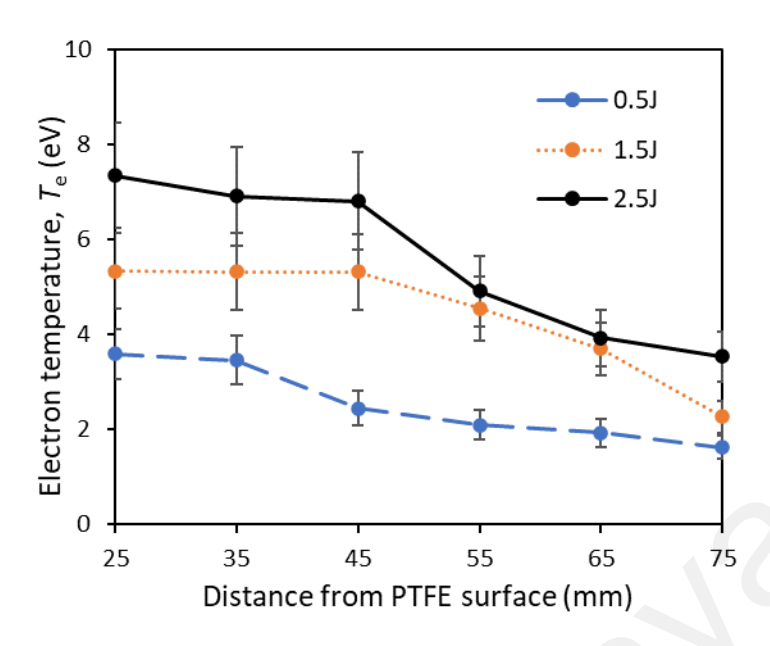


Figure 5.5: Peak electron temperatures as a function of distance (center axis) from the PTFE surface at discharge energy of 0.5-2.5 J

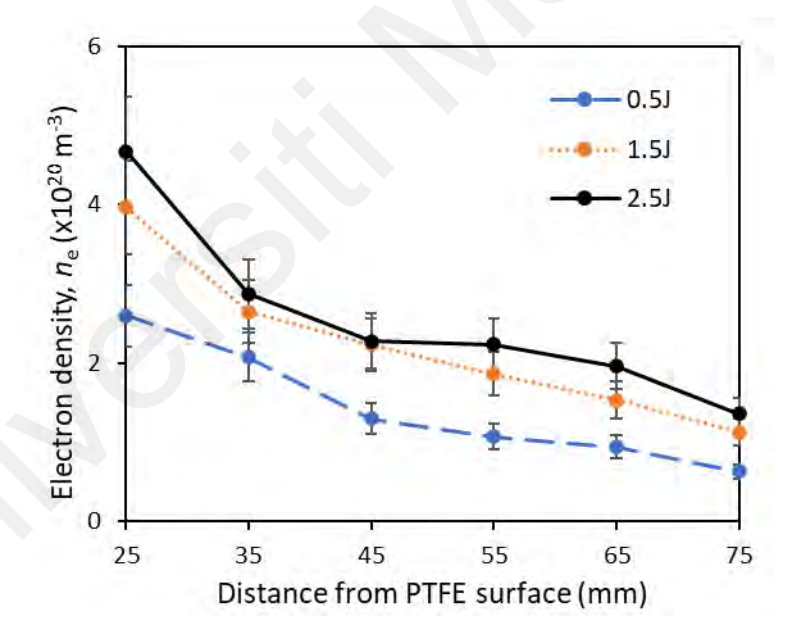


Figure 5.6: Peak electron density as a function of distance (center axis) from the PTFE surface at discharge energy of 0.5-2.5 J.

The peak values of $T_{\rm e}$ and $n_{\rm e}$ along the center axis of all discharge energies are plotted in Figure 5.5 and Figure 5.6 as a function of distance from the PTFE surface. Examining the behavior of $T_{\rm e}$ reveals that its value remains relatively stable within the first 5 to 10 mm of distance for all discharge energies. Specifically, it maintains around 7 eV for a discharge energy of 2.5 J, 5.4 eV for 1.5 J, and 3.5 eV for 0.5 J. Subsequently, $T_{\rm e}$ undergoes a noticeable decrease, reaching values of 3.5 eV, 2.3 eV, and 1.6 eV, respectively, at 75 mm.

In contrast to T_e , the electron density, n_e exhibits a clear and consistent decrease with increasing downstream distance. This decline is attributed to the expansion of the plasma plume as it moves away from the PTFE surface. For discharge energy of 0.5 J, it drops from 2.60×10^{20} m⁻³ to 6.30×10^{19} m⁻³, 3.96×10^{20} m⁻³ to 1.12×10^{20} m⁻³ for 1.5 J and 4.67×10^{20} m⁻³ to 1.35×10^{20} m⁻³ for 2.5 J. The monotonic decrease in n_e signifies the dilution of electron density over the expanding plume.

5.3.2 Radial profiles – parallel plane

Figures 5.7, 5.8 and 5.9 (a) and (b) effectively compare the radial profiles of the peak values of T_e and n_e as a function of angle between -30° to 30° for six distances in the parallel-plane measurement for discharge energy of 0.5 to 2.5 J. The radial profiles effectively showcase the variations in T_e and n_e across different angles, providing insights into the spatial distribution of these plasma parameters. For all discharge energies, both the T_e and n_e radial profiles exhibit a peak at the 0-degree angle, aligning with the direction of plasma propagation. This alignment shows that the highest values of T_e and n_e occur along the axis of plasma movement. As the analysis extends toward the outer regions on both sides (-30° to 30°), a gradual decrease in the radial profiles is observed, which aligns with general expectations in plasma expansion. It is noted that the radial symmetry, particularly at negative and positive angles, falls within the error bars. This show that the acceleration mechanisms are expected to be almost uniform in parallel plane.

At discharge energy of 0.5 J, The peak electron temperature declines to 2.58 eV at - 30° and 2.35 eV at the other side of 30° at d=25 mm. As the probes are moved downstream, the $T_{\rm e}$ drops to 1.18 eV and 1.24 eV respectively. However, beyond certain angular positions (more than 10° or less than - 10°), the electron temperature becomes relatively constant for all downstream positions. At this discharge energy, $n_{\rm e}$ shows a similar trend, peak at center axis, and decreases to $1.25 \times 10^{20} \ m^{-3}$ (- 30°) and $1.17 \times 10^{20} \ m^{-3}$ (30°) at d = 25 mm. At 75mm, there is a plateau in the $n_{\rm e}$ around $0.5 \times 10^{20} \ m^{-3}$.

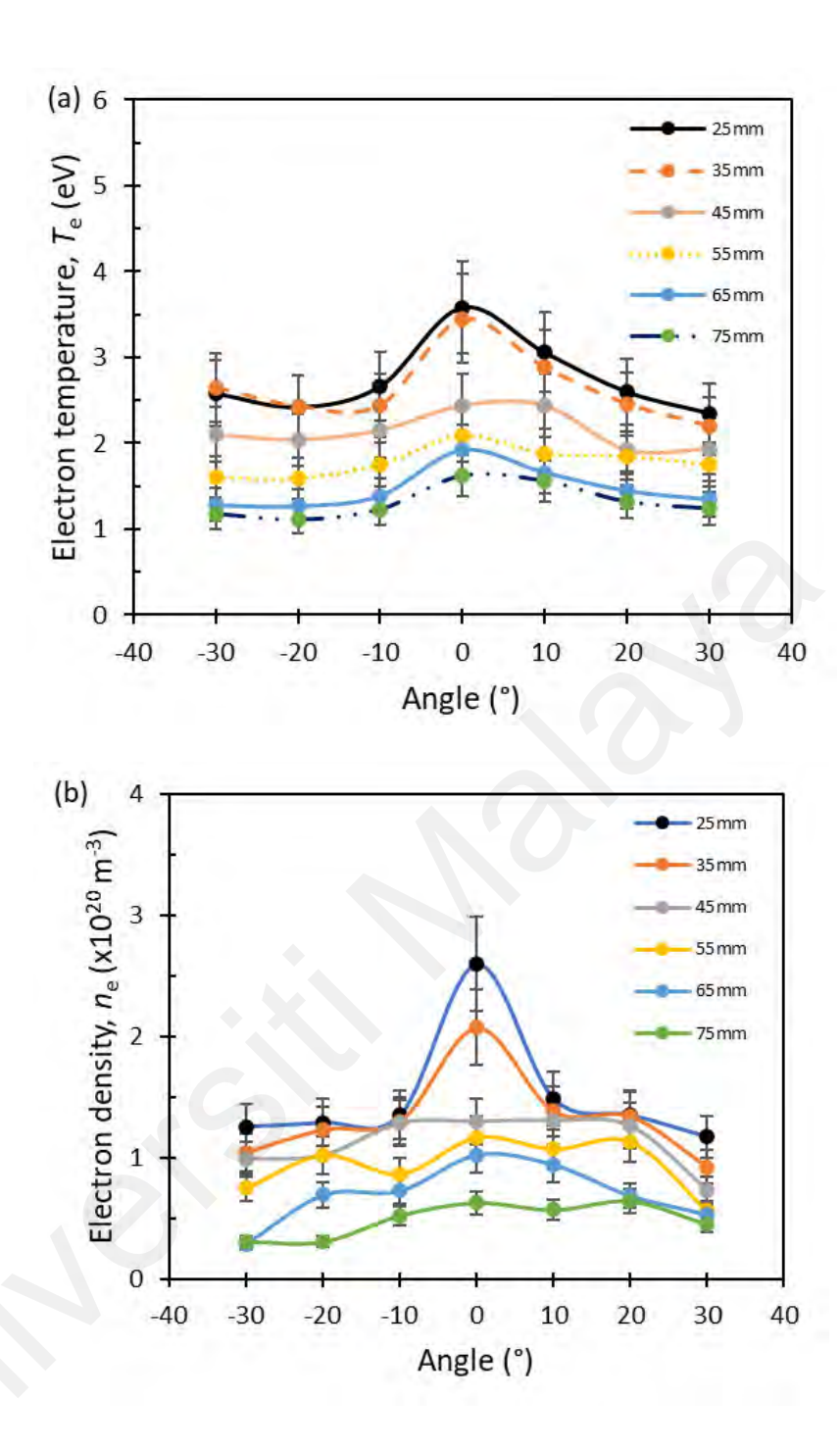


Figure 5.7: (a) Parallel plane measurement of peak electron temperature, T_e and (b) peak electron density, n_e at various distance from angle -30° to 30° for 0.5 J.

As shown in Figure 5.8 of discharge energy of 1.5 J, the overall trends of electron temperature and density are similar to those in discharge energy of 0.5 J but with higher magnitude. At the distance of 25mm, $T_{\rm e}$ varies from 3.65 eV to 3.32 eV across the angular variation from -30° to 30° with a peak of 5.43 eV at 0°, further downstream by 50mm, $T_{\rm e}$ declines to 1.17 eV and 1.00 eV across the 60-degree range. The electron density

distribution shows a higher peak-like shape at the center axis, indicating a concentration of electrons in that region. The graph then becomes flat for angles less than -10° and more than 10°, shows a relatively constant electron density at these angular positions (1.73 × $10^{20} \ m^{-3}$ at 25mm and $0.73 \times 10^{20} \ m^{-3}$ at 75mm).

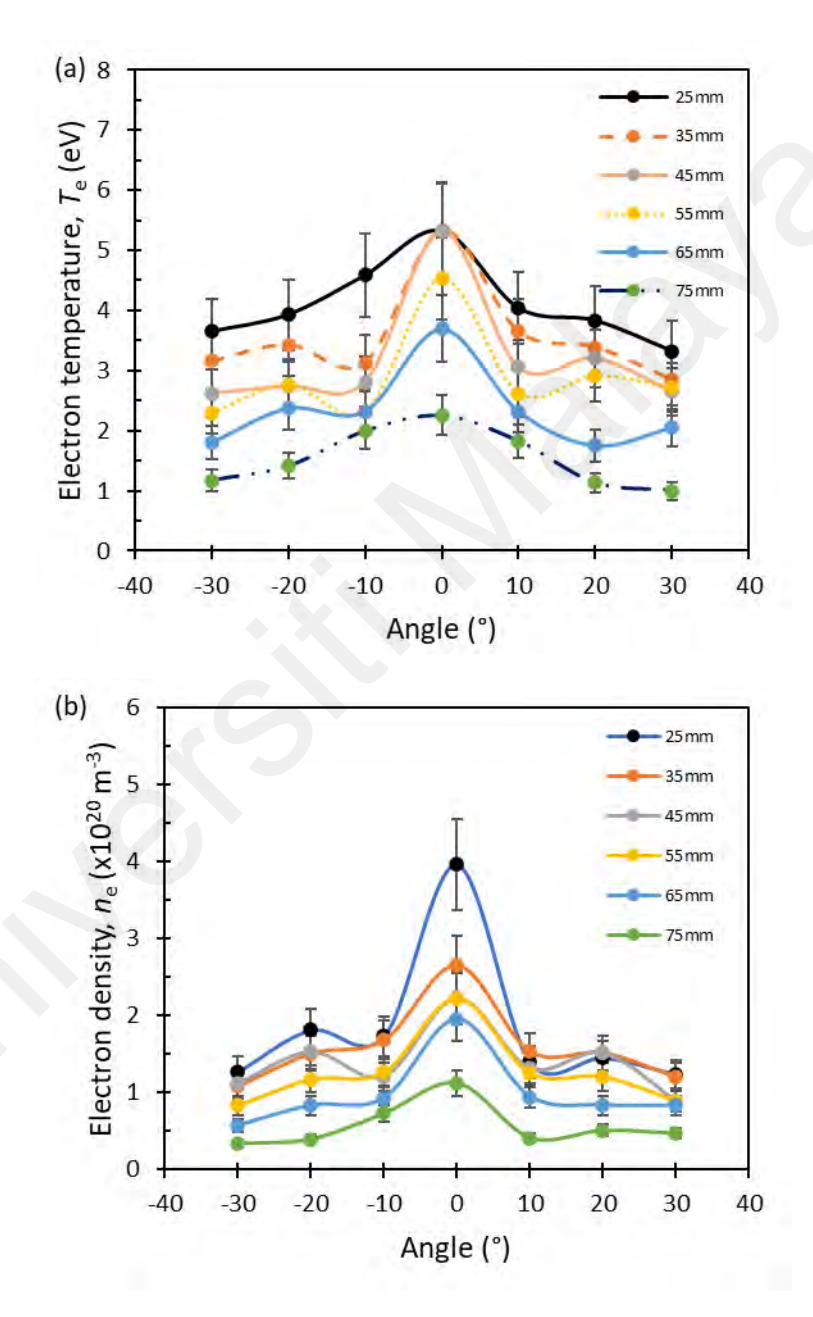


Figure 5.8: (a) Parallel plane measurement of peak electron temperature, T_e and (b) peak electron density, n_e at various distance from angle -30° to 30° for 1.5 J.

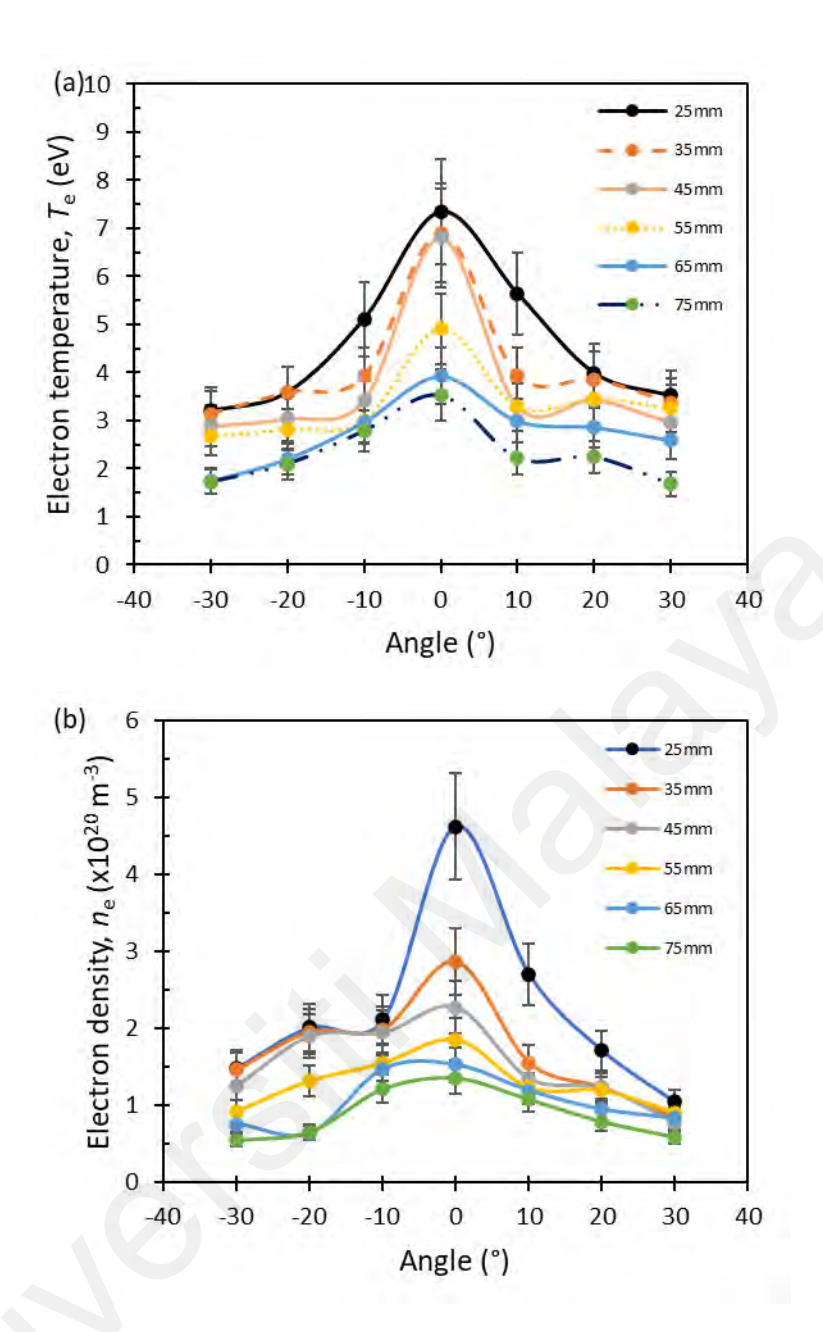


Figure 5.9: (a) Parallel plane measurement of peak electron temperature, T_e and (b) peak electron density, n_e at various distance from angle -30° to 30° for 2.5 J.

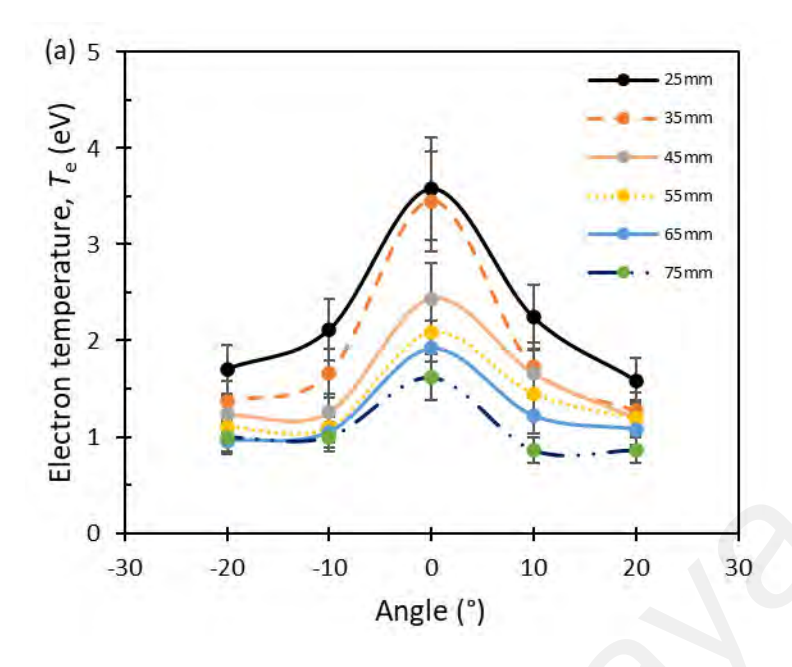
When the discharge energy further increases to 2.5 J (Figure 5.9), the shapes of the electron temperature and density graphs resemble those at lower discharge energies, suggesting a continuity in the observed trends although there is an increase in the values of T_e and n_e . At 25 mm distance, the electron temperature reaches a peak of 7.34 eV at the centre and declines to 3.20 eV and 3.52 eV at angles of 30° to the left and right side of the center axis. As the plasma spread out, the electron density at the 75 mm distance become $0.55 \times 10^{20} \ m^{-3}$ and $0.59 \times 10^{20} \ m^{-3}$ at -30° and 30° respectively.

5.3.3 Radial profiles- perpendicular plane

Figures 5.10, 5.11, and 5.12 (a) and (b) present detailed radial distributions of T_e and n_e in the perpendicular plane. The electron temperature, T_e and electron density, n_e is the highest along the center axis. It is seen that in the perpendicular plane, the plasma plume is more confined than parallel plane due to the obstruction of the electrode and nozzle. An interesting phenomenon that can be observed is the differences in the values of T_e and n_e at the positive angle side (cathode). In this region, both T_e and n_e exhibit slightly larger values. This is more obvious in higher discharge energy. This observation aligns with findings reported by (Wu et al, 2020), where a similar trend was noted. Specifically, Wu et al. reported that clusters of plasmas are formed near the cathode and anode, these two clusters meet downstream, and the intersection is closer to cathode, hence the plasma density was slightly higher at the cathode side, especially at closer distances.

At discharge energy of 0.5 J (Figure 5.10), both $T_{\rm e}$ and $n_{\rm e}$ shows typical bell- shape curve, $T_{\rm e}$ and peak at 3.58 eV and drops to 1.58 eV and 1.70 eV at two ends for 25mm distance, as the distances increases, the value of $T_{\rm e}$ drops accordingly. Similar with $T_{\rm e}$, electron density, $n_{\rm e}$, sharp peaks notice at 0° , and the curve gets flatter when the probes move downstream, recording a value of $0.21 \times 10^{20} \ m^{-3}$ at 20 degrees from the center axis when distance equals to 75mm.

As discharge energy increases to 1.5 J, which is shown in Figure 5.11, the asymmetry is noticeable in both $T_{\rm e}$ and $n_{\rm e}$. The value of $T_{\rm e}$ at 10° is 3.44 eV, which is 20% more than -10° at same distance of 75mm, while for the values of $n_{\rm e}$, at 10°, it is 1.53× 10²⁰ m^{-3} , 32% larger compared to $1.16 \times 10^{20} \, m^{-3}$ at -10°. However, as the measurements progress downstream, this asymmetry diminishes, and both $T_{\rm e}$ and $n_{\rm e}$ become more uniform at the two ends.



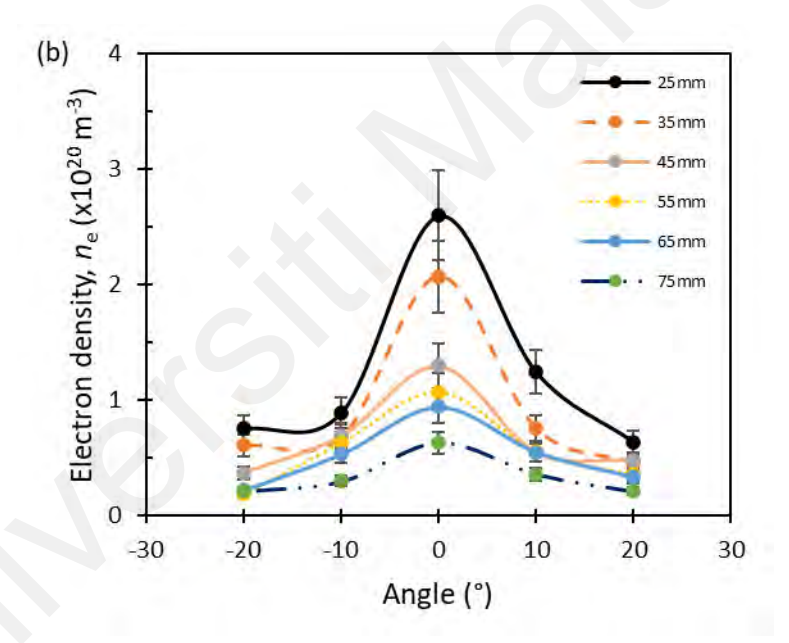


Figure 5.10: (a) Perpendicular plane measurement of peak electron temperature, $T_{\rm e}$ and (b) peak electron density, $n_{\rm e}$ at various distance from angle -20° to 20° for 0.5 J.

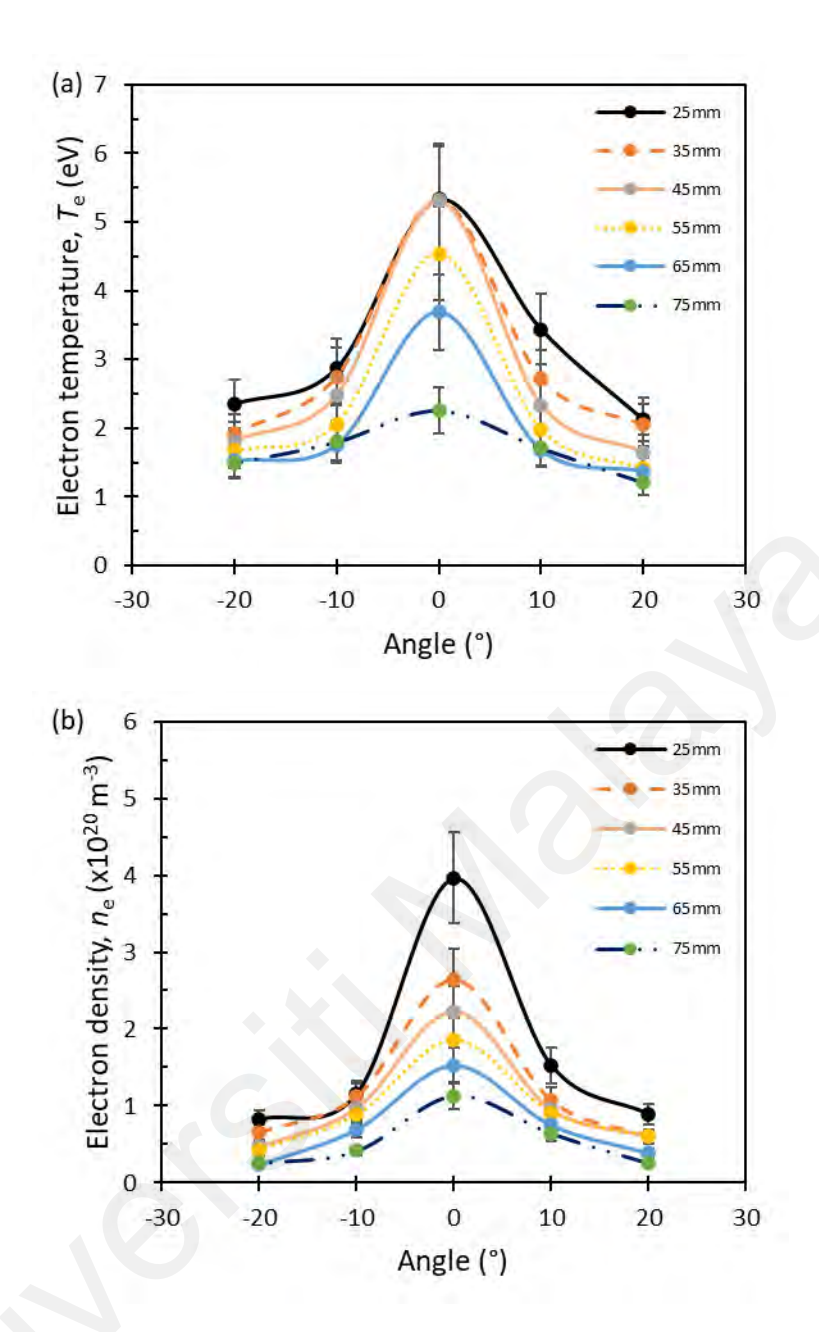
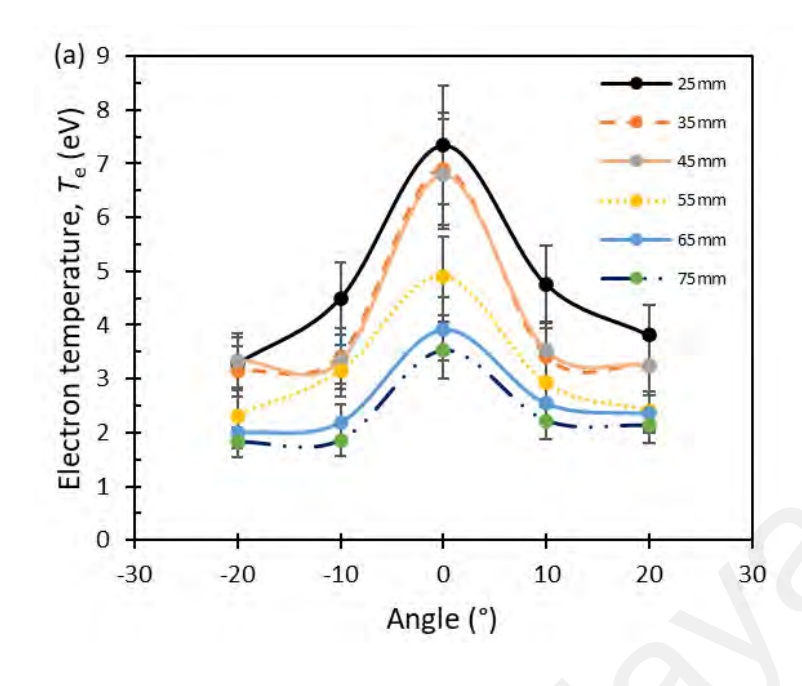


Figure 5.11: (a) Perpendicular plane measurement of peak electron temperature, T_e and (b) peak electron density, n_e at various distance from angle -20° to 20° for 1.5 J.

For discharge energy of 2.5 J, the asymmetric effect extends wider to the 20 degrees angle, the electron temperature for 25mm at 10° was 4.76 eV and 3.81 eV at 20° , which is 6% and 16 % higher than those at the other end. As the probes move downstream further by 50mm, the values drop to 2.22 eV and 2.13 eV at 10° and 20° respectively, which is 20% and 17% higher than those at -10° and -20° respectively. Similar trend is observed on the electron density, $n_{\rm e}$, at distance of 25mm at 10° and 20° angles, the values are

 $1.43 \times 10^{20}~m^{-3}$ and $1.23 \times 10^{20}~m^{-3}$. Compared to -10° and -20°, the values are $1.09 \times 10^{20}~m^{-3}$ and $1.06 \times 10^{20}~m^{-3}$, which are 31% and 16% lower respectively. When the plasma propagates to 75mm, the values of $n_{\rm e}$ for -20°, -10°, 10° and 20° are $0.41 \times 10^{20}~m^{-3}$, $0.45 \times 10^{20}~m^{-3}$, $0.53 \times 10^{20}~m^{-3}$ and $0.46 \times 10^{20}~m^{-3}$ respectively, showing 18% and 12% higher at the 10° and 20° angles.



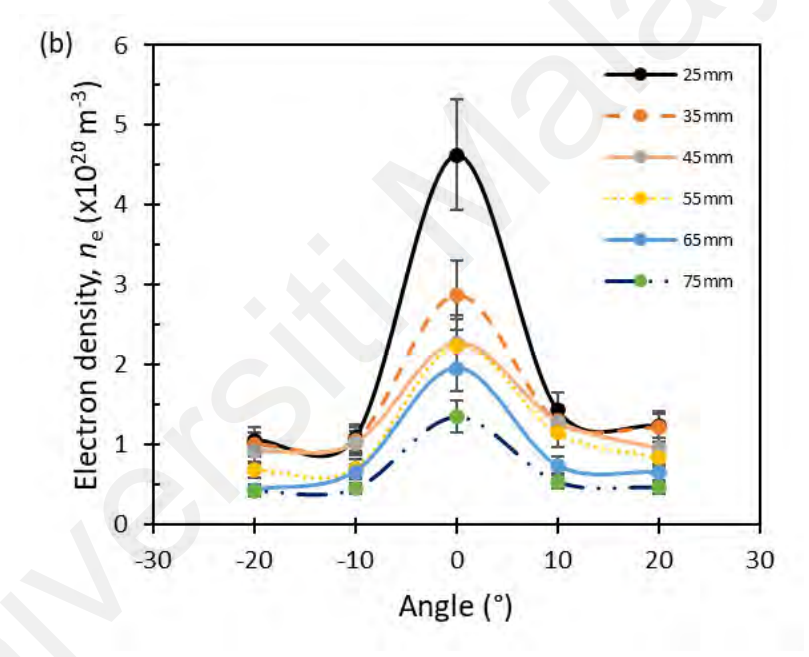


Figure 5.12: (a) Perpendicular plane measurement of peak electron temperature, $T_{\rm e}$ and (b) peak electron density, $n_{\rm e}$ at various distance from angle -20° to 20° for 2.5 J.

5.4 Plasma species identification

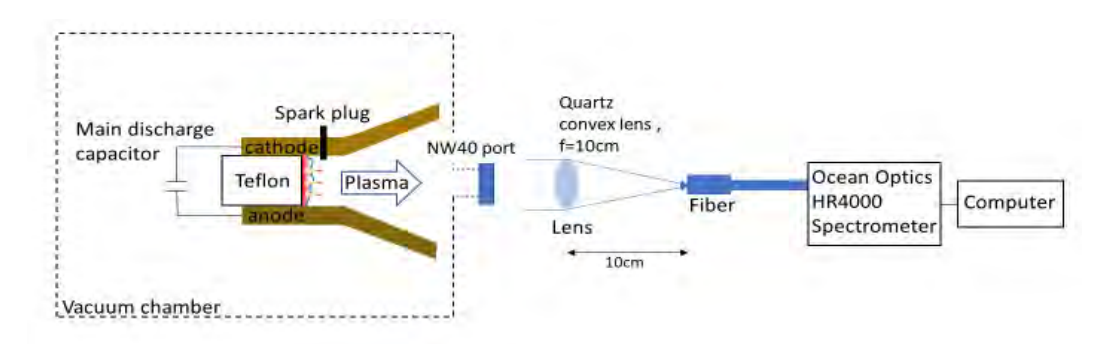


Figure 5.13: Setup of OES system.

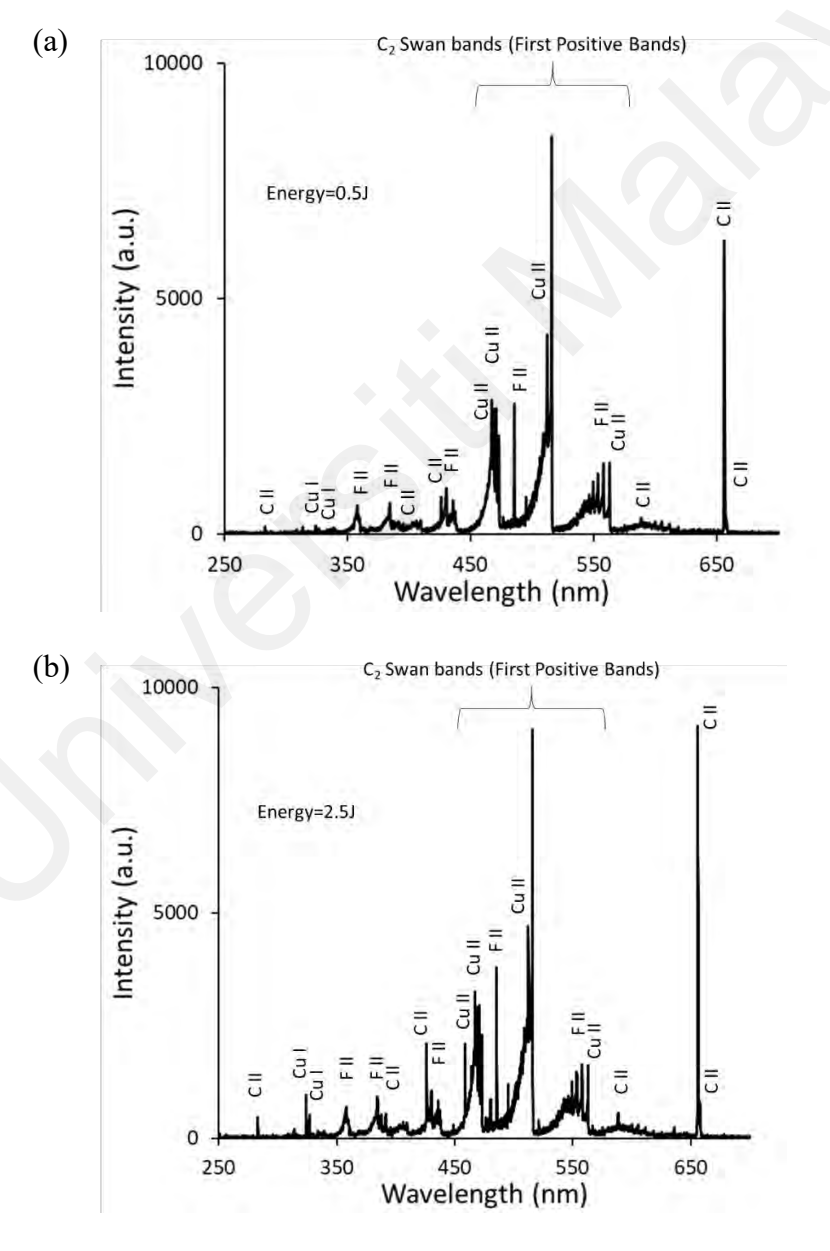


Figure 5.14: Emission spectral of plasma at discharge energy of (a) 0.5 J, and (b) 2.5 J.

Figure 5.13 shows the setup of the OES system and Figure 5.14 shows the emission spectra of the plasma at different energy. Most of the lines are carbon and fluorine lines as expected to be due to the decomposition of PTFE, with chemical formula of C₂F₄. Notably, the presence of copper lines in the spectra signifies the erosion of the copper electrode during the plasma discharge process. The molecular C₂ First positive bands are known to occur frequently in sources containing carbon and in high current density discharges (Markusic et al., 1997). Comparisons with the spectra reported in other PPT, as documented in the literature (Koizumi et al., 2007), reveal similarities in composition. Increase of discharge energy from 0.5 to 2.5 J leads to an increase of intensity as expected, but the composition of plasma remains the same, so no new peaks were found.

Under the partial LTE condition, the electron temperature $T_{\rm e}$ in the plasma can be determined by measuring the relative intensities of the ion spectral lines. If the energy level population is distributed according to the Boltzmann law, the relative intensity $I_{\rm mn}$ is given by (Markusic & Spores, 1997)

$$\ln \frac{I_{mn}\lambda_{mn}}{g_m A_{mn}} = \ln \frac{N}{Z} - \frac{E_m}{T_e}$$
 (5.1)

where

 I_{mn} = relative intensity

 λ_{mn} = wavelength

 g_m = degeneracy of the upper state

 A_{mn} = the transition probability from the upper state m to the lower state n

N = total number density

Z = partition function

 E_m = Energy of the upper state

Information on C II spectral lines is listed in table 5.1. A plot of the graph of $ln \frac{I_{mn}\lambda_{mn}}{g_m A_{mn}}$ vs. E_m has a gradient of $-\frac{1}{T_e}$. Therefore, T_e can be obtained without knowing the values of N and Z.

Table 5.1: C II spectral lines and the parameters.

λ_{mn} (nm)	$A_{mn} (S^{-1})$	E_m (eV)	g_m
391.898	6.36×10^{7}	19.49454	2
392.069	1.27×10^{8}	19.49454	2
426.726	2.38×10^{8}	20.95064	8
588.977	3.15×10^7	20.15048	4
657.805	3.63×10^{7}	16.33312	4
658.288	3.62×10^7	16.33174	2
723.132	3.52×10^7	18.04581	4
723.642	4.22×10^7	18.04599	6

The electron temperature $T_{\rm e}$ in the plasma can be determined by measuring the relative intensities of the Carbon II spectral lines. C II lines were chosen for Boltzmann plot because only C II exhibits sufficient distribution of upper state energy which is comparable to the ambient electron temperature. To further improve the accuracy of the calculation, the emission spectral lines were fitted by the Voigt profile (Figure 5.15).

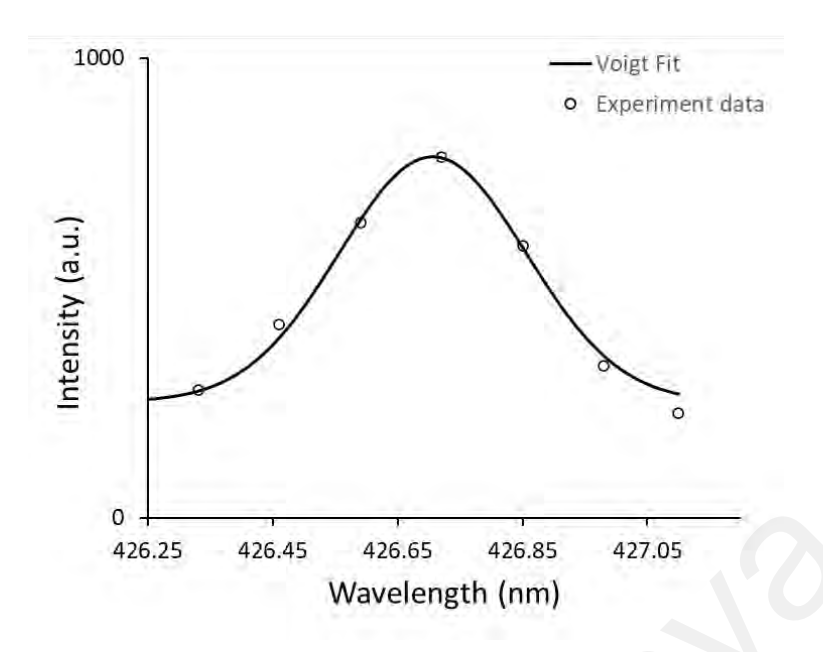


Figure 5.15: Voigt fit for C II 426.7nm line.

Figure 5.16 shows Boltzmann plot at discharge energy from 0.5 to 2.5 J. A line of best fit was drawn, and the electron temperature was estimated from the gradient. The assumption of LTE condition was valid as all the data points fall within the straight line.

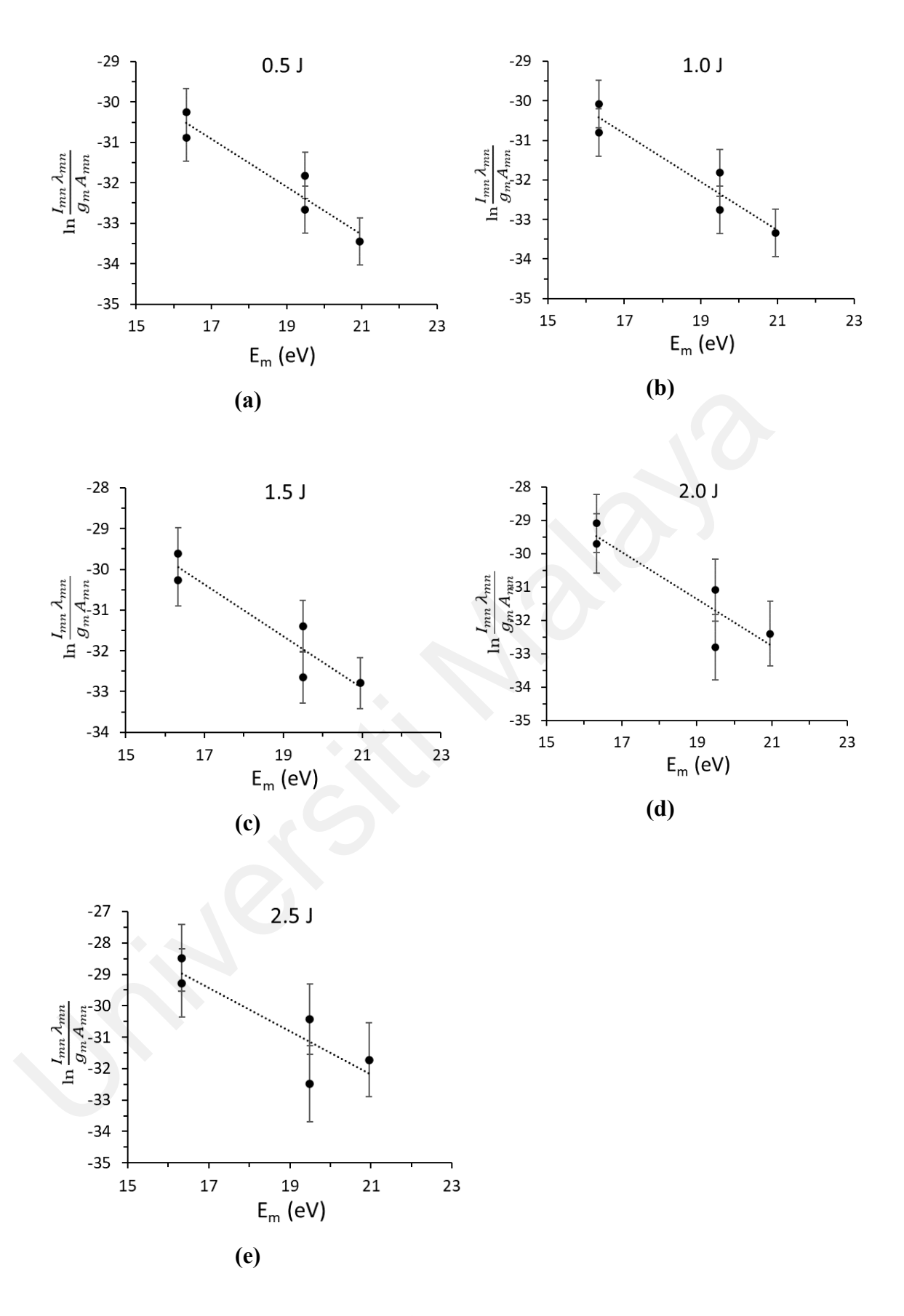


Figure 5.16: Boltzmann plot for C II lines at discharge energy of 0.5 - 2.5 J.

The electron temperature, T_e from discharge energy of 0.5 J and 2.5 J is shown in Figure 5.17. There is not much increase in electron temperature, the T_e was within the range from 1.5 to 1.7 eV. This aligns with findings from other published works that utilized a triple Langmuir probe for electron temperature measurements (Wang et al. 2013). Despite the increase in supplied energy to 2.5 J, there is a notable absence of higher ionization states, such as C III or F III lines, in the emission spectra. This absence indicates that the additional energy input is not resulting in a significant increase in ionization states. Instead, it is suggested that the increased energy is likely being converted into kinetic energy, as shown in Figure 4.16. This shift in energy distribution, where a substantial portion is converted to kinetic energy rather than higher ionization states, is consistent with the observed stability in electron temperature.

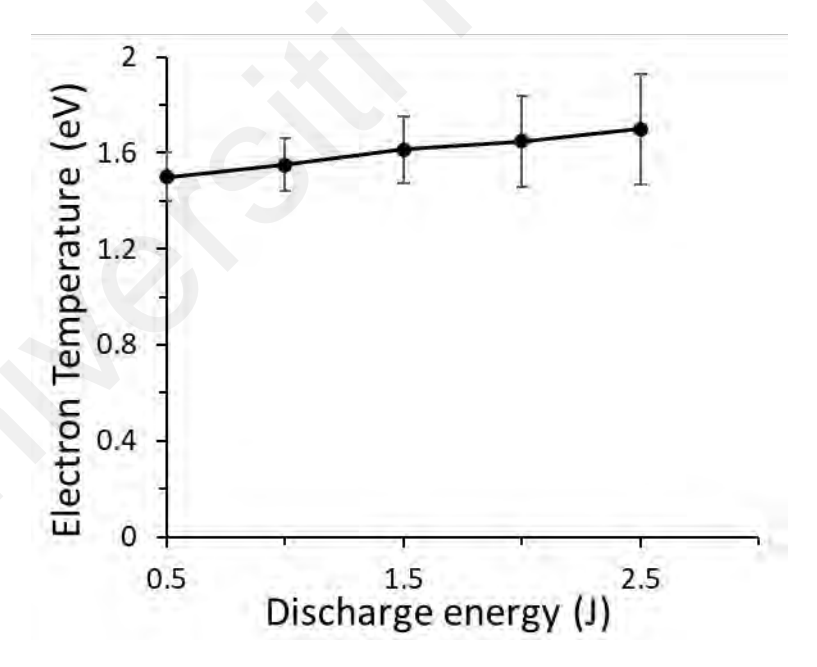


Figure 5.17: Electron temperature, T_e as a function of discharge energy.

5.5 Comparison to different plasma thruster

Table 5.3 compares the electron temperature and density from this work with published results from other PPT systems. The comparison is crucial for understanding how the plasma parameters in the present work align with those reported in the broader research community. Upon examination, the electron density values in this study fall within the ranges observed in other PPTs that have been operated across a wide range of energies (1-40 J) while the electron temperatures show many differences based on the probe measurement. Owing to differences in points of measurements (last column), only qualitative comparisons may be made. To illustrate, a specific comparison is made with the work of Eckman et al. (2002), where the probe measurements were conducted at 60mm during 5 J operation whereas, the measurements in this work were taken at distances from 25 to 75 mm. The electron densities and electron temperatures obtained are of the same order as Eckman et al.'s. Optical emission spectroscopy (OES) serves as a non-contact diagnostic method, but it faces limitations in achieving point-to-point measurements. When using OES, the collected optical signal integrates information across the depth direction, resulting in the loss of depth-specific details. Consequently, the electron temperature derived from OES tends to be lower compared to calculations based on probe measurements. This discrepancy arises because OES provides a more generalized assessment, lacking the depth resolution available in probe measurements. When we compare with the two OES measurements (Schönherr et al. 2013; Eeng Liu et al. 2008), the $T_{\rm e}$ values from this work are of the same magnitude. In short, these comparisons, while qualitative, serve to validate the plasma characteristics and expulsion dynamics observed in this low energy PPT.

Table 5.3: Comparison with other Pulsed Plasma Thrusters (PPTs).

Work by	Method	Discharge energy (J)	T _e (eV)	$n_{\rm e}~({ m m}^{-3})$	Point of measurement (mm)
Gatsonis	4-Probe	5	10	1.0×10^{20}	100
et al.		20	10.8	7.2×10^{20}	100
		40	13.5	1.3×10^{21}	100
Eckman	3-Probe	5	4.5	1.6×10^{20}	60
et al.		20	4.5	1.6×10^{21}	60
		40	4.5	1.8×10^{21}	60
Schönherr et al.	OES	68	2.25	$2.7 \sim 37.3 \times 10^{22}$	70
Eeng Liu et al.	OES	5	1.55	2.53×10^{22}	-
This work	3-Probe	2.5	7.34 3.53	$4.67 \times 10^{20} \\ 1.35 \times 10^{20}$	25 75
This work	OES	2.5	1.7	-	-

5.6 Summary

The discharge current increases with increasing discharge energy, from 4.07 kA at 0.5 J to 9.41 kA at 2.5 J. As expected, the electron temperature and density decrease as the plasma expands into the surrounding and cools down as it propagates downstream. For the parallel plane, the results from triple Langmuir probe show that acceleration mechanisms are almost uniform but for the perpendicular plane, the plasma is more confined and exhibit non-symmetric nature, the electron temperature and density show larger values near the cathode region.

In the OES result, most of the lines are carbon and fluorine lines as expected, due to the decomposition of PTFE of chemical formula $(C_2F_4)_n$. The presence of copper lines in the spectra signifies the erosion of the copper electrode during the discharge. The electron temperature obtained from OES is lower than the triple Langmuir Probe data because OES provides a more averaged evaluation, lacking the depth resolution.

CHAPTER 6: CONCLUSION

6.1 Conclusion

6.1.1 Thrust and propulsion

Within the low discharge energy (E_0) range of 0.5 - 2.5 J of a tongue-flared PPT, the impulse bit I_{bit} increased slower at a specific impulse bit of 17 μ Ns/J than that of PPTs at higher energies. The electromagnetic component ($I_{\text{bit-em}}$) that contributes to the I_{bit} was about 50 % for E_0 of 1–2.5 J when a higher change in inductance with position (L') with the tongue-flared electrodes was considered; and dropped to 33% at the 0.5 J. These values are higher than those reported in similar PPTs at 1.6-2 J. The derived values of specific impulse $I_{\rm sp}$ were 2-3 times higher especially at $E_0/A < 2~{\rm J/cm^2}$ than those predicted by a semi-empirical formula of Gessini-Paccani. This is possibly due to change in discharge mechanism at the lower discharge energy. Likewise, the mean exhaust velocity c_e as well as the thrust efficiency η , both derived using values of m_{bit} , also recorded a higher value especially at the low end of the discharge energy range albeit with large uncertainties (60% –70% at 0.5 J) and decrease with increasing discharge energy which is contrary to intuition. At discharge energy around 2 J, c_e and η were closer to values published in the references (Clark et al., 2011). Using another method (independent of the measured m_{bit}) that employed the triple Langmuir probe to determine the 'fastest' ion velocity at the downstream locations external to the PPT channel, this velocity increased with increasing discharge energies at the exit plane of the PPT channel which is to be expected. Although the 'fastest' ion velocity is not equal to the mean ion exhaust velocity and the mean exhaust velocity, the trend can still be representative of that in the mean exhaust velocity; and this seemingly contradicts the trend observed for $c_{\rm e}$. The increase of 'fastest' ion velocity with distance downstream indicates that the ions were accelerating outside the PPT channel, possibly to have been aided by ambipolar

diffusion. Analyzing the elemental component of charring on the propellant surface, the highest proportion was C (85 at%), trailed by F (13 at%) with traces of Cu from the electrodes. The globular structures and the EDX spectrum suggest that char was formed from carbon back flux from the plasma rather than incomplete decomposition of the propellant. Compared to published data (gathered from various PPTs of 1.8–8.5 J with tongue-flared, rectangular-flared and plane-parallel electrodes), a wider spread in values of I_{sp} and η at the low energy end could be seen, or in other words, higher inconsistency in some performance parameters of the PPTs is likely to occur here similar to our observation. This could be due to the weaker discharge that did not get distributed over the entire exposed surface of the propellant and relatively 'excess' charring that led to a smaller mass bit measured.

6.1.2 Plasma characterization

The maximum electron density and temperature near to the exit were determined to be $4.63\times10^{20} \,\mathrm{m}^{-3}$ and $7.34 \,\mathrm{eV}$ respectively for discharge energy of $2.5 \,\mathrm{J}$ and $2.60\times10^{20} \,\mathrm{m}^{-3}$ and $3.58 \,\mathrm{eV}$ respectively for discharge energy of $0.5 \,\mathrm{J}$. The plasma plume of PPT was observed to be canted towards the cathode, both $T_{\rm e}$ and $n_{\rm e}$ are larger nearer to cathode. The results from OES verified the decomposition of ablated PTFE and erosion of copper electrodes. These energized neutral particles and ions ejected from the discharge plasma are responsible for the thrust necessary for movement control of micro satellites. It is concluded that the side-fed, tongue-flared PPT design is working well. The agreement between these findings suggests a consistent behaviour in plasma characteristics, emphasizing the importance of considering the angle and distance dependencies in understanding the complex dynamics of plasma in this experimental setup. Such insights contribute significantly to the broader understanding of plasma physics and play a crucial role in optimizing the performance and efficiency of plasma-based systems.

6.2 Suggestions for further work

To enhance and improve the performance of pulsed plasma thruster at low discharge energy, the following suggestions are proposed:

- a) Lifetime testing. PPTs with low discharge energy may exhibit decent impulse bit and efficiency, a key concern arises regarding the potential charring effect and its impact on the thruster's lifespan. This aspect requires careful and thorough study to ensure the sustained effectiveness of the propulsion system.
- b) Triple Langmuir probe measurements with smaller distance between neighbouring points to capture variations on a smaller scale. This allows for a finer resolution in the spatial distribution, providing insights into localized variations in plasma parameters.
- c) Optimize electrode design. Evaluate and redesign of the electrode configuration to ensure efficient energy transfer during the discharge phase. Consider using materials with higher conductivity and durability to minimize energy losses and electrode erosion.
- d) Simulation and modelling. Utilize computational simulations and modeling tools to predict and understand the behavior of the PPT under different discharge energy conditions. Fine-tune the design parameters based on simulation results to achieve optimal performance.

By implementing these suggestions, it is anticipated that the performance of the pulsed plasma thruster can be significantly enhanced, particularly at lower discharge energy levels.

REFERENCES

- Anders, A., Brown, I. G., MacGill, R. A., & Dickinson, M. R. (1998). Triggerless' triggering of vacuum arcs. Journal of Physics D: Applied Physics, 31(5), 584.
- Antropov, N., Diakonov, G., Orlov, M., Popov, G. A., Tyutin, V., & Yakovlev, V. (2003, March). Development and refinement of highly efficient 150 J APPT. In International Electric Propulsion Conference Paper (pp. 03-061).
- Beiting, E. (1999). Impulse thrust stand for MEMS propulsion systems. 35th Joint Propulsion Conference and Exhibit (p. 2720). doi: 10.2514/6.1999-2720
- Berkery, J. W., & Choueiri, E. Y. (2003, March). Characterization of current sheet evolution in a pulsed electromagnetic accelerator. In 28th International Electric Propulsion Conference, Toulouse, France (pp. 2003-0307).
- Brady, M. E., & Aston, G. (1983). Pulsed plasma thruster ignitor plug ignition characteristics. Journal of Spacecraft and Rockets, 20(5), 450-451.
- Burton, R., Wilson, M., & Bushman, S. (1998, July). Energy balance and efficiency of the pulsed plasma thruster. 34th AIAA/ASME/SAE/ASEE Joint Propulsion Conference and Exhibit (p. 3808). doi: 10.2514/6.1998-3808
- Burton, R. L., & Turchi, P. J. (1998). Pulsed plasma thruster. Journal of Propulsion and Power, 14(5), 716-735.
- Cappelletti, C., & Robson, D. (2021). CubeSat missions and applications. In Cubesat Handbook (pp. 53-65). Academic Press.
- Chen, S. L., & Sekiguchi, T. (1965). Instantaneous direct-display system of plasma parameters by means of triple probe. Journal of applied physics, 36(8), 2363-2375.
- Ciaralli, S., Coletti, M., & Gabriel, S. B. (2016). Results of the qualification test campaign of a Pulsed Plasma Thruster for Cubesat Propulsion (PPTCUP). Acta Astronautica, 121, 314-322.
- Clark, C., Guarducci, F., Coletti, M., & Gabriel, S. (2011). An off-the-shelf electric propulsion system for cubesats.
- Coletti, M., Marques, R. I., & Gabriel, S. B. (2009, September). Design of a two-stage PPT for cubesat application. Paper presented at Proceedings of the 31st International Electric Propulsion Conference, Michigan, USA.
- D'Souza, B. C., & Ketsdever, A. D. (2005). Investigation of time-dependent forces on a nano-Newton-second impulse balance. Review of Scientific Instruments, 76(1).

- Eckman, R., Byrne, L., Gatsonis, N. A., & Pencil, E. J. (2001). Triple Langmuir probe measurements in the plume of a pulsed plasma thruster. Journal of Propulsion and Power, 17(4), 762-771.
- Emhoff, J., Simon, D., & Land, B. (2007, July). Progress in thrust measurements from micro pulsed plasma discharges. 43rd AIAA/ASME/SAE/ASEE Joint Propulsion Conference & Exhibit (p. 5299). doi: 10.2514/6.2007-5299
- Freeman, A. (2020). Exploring our solar system with CubeSats and SmallSats: the dawn of a new era. CEAS Space Journal, 12(4), 491-502.
- Gamero-Castano, M. (2003). A torsional balance for the characterization of microNewton thrusters. Review of scientific instruments, 74(10), 4509-4514.
- Gatsonis, N. A., Zwahlen, J., Wheelock, A., Pencil, E. J., & Kamhawi, H. (2004). Pulsed plasma thruster plume investigation using a current-mode quadruple probe method. Journal of propulsion and power, 20(2), 243-254.
- Gatsonis, N., Juric, D., Stechmann, D., & Byrne, L. (2007). Numerical analysis of Teflon ablation in pulsed plasma thrusters. In 43rd AIAA/ASME/SAE/ASEE Joint Propulsion Conference & Exhibit (p. 5227).
- Gessini, P., & Paccani, G. (2001, Oct). Ablative pulsed plasma thruster system optimization for microsatellites. Paper presented at 27th International Electric Propulsion Conference, California, United States.
- Glascock, M. S., Rovey, J. L., & Polzin, K. A. (2019). Electric solid propellant ablation in an arc discharge. Journal of Propulsion and Power, 35(5), 984-993.
- Glascock, M. S., Rovey, J. L., Williams, S., & Thrasher, J. (2017). Plume characterization of electric solid propellant pulsed microthrusters. Journal of Propulsion and Power, 33(4), 870-880.
- Guarducci, F., Coletti, M., & Gabriel, S. B. (2011, September). Design and testing of a micro pulsed plasma thruster for Cubesat application. In 32nd international electric propulsion conference (pp. 2011-239).
- Guman, W. (1975, March). Designing solid propellant pulsed plasma thrusters. 11th Electric Propulsion Conference (p. 410). doi: 10.2514/6.1975-410
- Guo, Z. L., Zhao. W. H. (1986). Arc and thermal plasma. Beijing: Science Press.
- Haag, T. W. (1997). Thrust stand for pulsed plasma thrusters. Review of Scientific Instruments, 68(5), 2060-2067.
- Hicks, F. M., Perna, L., COFFMAN, C. S., & Lozano, P. C. (2013). Characterization of a CubeSat compatible magnetically levitated thrust balance for electrospray propulsion

- systems. 49th AIAA/ASME/SAE/ASEE Joint PropulsionConference (p. 3879). doi: 10.2514/6.2013-3879
- Horneck, G. (2011). Space Vacuum Effects. Berlin, Heidelberg: Springer.
- Igarashi, M., Kumagai, N., Sato, K., Tamura, K., Takegahara, H., Okamoto, H., Wakizono, T., & Hashimoto, H. (2001, Oct). Performance improvement of pulsed plasma thruster for micro satellite. Paper presented at 27th International Electric Propulsion Conference, California, United States.
- Jianjun, W. U., Zhang, Y., Yang, O. U., & Zhang, H. (2020). Experimental investigation on the plasma morphology of ablative pulsed plasma thruster with tongue-shaped and flared electrodes. Plasma Science and Technology, 22(9), 094007.
- Jones, S., Paschalidis, N., Rodriguez, M., Sittler Jr, E. C., Chornay, D. J., Cameron, T., ... & Bellardo, J. (2015, December). ExoCube INMS with neutral hydrogen mode. In AGU Fall Meeting Abstracts (Vol. 2015, pp. SA32A-06).
- Kamhawi, H., & Pencil, E. (2002). High thrust-to-power parallel-rail pulsed plasma thruster design. In 38th AIAA/ASME/SAE/ASEE Joint Propulsion Conference & Exhibit (p. 3975).
- Keidar, M., & Beilis, I. (2013). Plasma engineering: applications from aerospace to bio and nanotechnology. Academic Press.
- Keidar, M., Boyd, I. D., Antonsen, E. L., Gulczinski III, F. S., & Spanjers, G. G. (2004). Propellant charring in pulsed plasma thrusters. Journal of Propulsion and Power, 20(6), 978-984.
- Keidar, M., Boyd, I. D., Antonsen, E., & Spanjers, G. G. (2004). Electromagnetic effects in the near field plume exhaust of a micro-pulsed-plasma thruster. Journal of propulsion and power, 20(6), 961-969.
- Keidar, M., Boyd, I. D., Antonsen, E. L., Burton, R., & Spanjers, G. G. (2006). Optimization issues for a micropulsed plasma thruster. Journal of propulsion and power, 22(1), 48-55.
- Kelly, A., & Jahn, R. (1990, July). The application of the triple probe method to MPD thruster plumes. 21st International Electric Propulsion Conference (p. 2667). doi: 10.2514/6.1990-2667
- Kimura, I. (1978). Preliminary experiments on pulsed plasma thrusters with applied magnetic fields. In 13th International Electric Propulsion Conference (p. 655).
- Koizumi, H., Kakami, A., Furuta, Y., Komurasaki, K., & Arakawa, Y. (2003, March). Liquid propellant pulsed plasma thruster. In Proceedings of 28th International Electric Propulsion Conference, Toulouse, France (No. 2003-87).

- Koizumi, H., Noji, R., Komurasaki, K., & Arakawa, Y. (2007). Plasma acceleration processes in an ablative pulsed plasma thruster. Physics of plasmas, 14(3).
- Kumagai, N., Sato, K., Tamura, K., Kawahara, K., Koide, T., Takegahara, H., ... & Hashimoto, H. (2003, March). Research and development status of low power pulsed plasma thruster system for μ-Lab Sat II. In 28th International Electric Propulsion Conference, Toulouse, France.
- Lam, J. K., Koay, S. C., Lim, C. H., & Cheah, K. H. (2019). A voice coil based electromagnetic system for calibration of a sub-micronewton torsional thrust stand. Measurement, 131, 597-604.
- Lee, H. C., Lim, C. H., Lau, Y. T., & Chin, O. H. (2021). Triple Langmuir probe measurements in a low-energy tongue-flared configuration plasma thruster. Vacuum, 187, 110135.
- Lee, H. C., Lim, C. H., Woo, H. J., Goh, B. T., CHIN, O. H., & Tou, T. Y. (2023). Performance of pulsed plasma thruster at low discharge energy. Plasma Science and Technology.
- Lee, H. C., Ng, Z. H., Lau, Y. T., Chin, O. H., Goh, B. T., & Lim, C. H. (2021, February). Study of a side-fed, tongue-flared configured pulsed plasma thruster. In AIP Conference Proceedings (Vol. 2319, No. 1). AIP Publishing.
- Leiweke, R., Turchi, P., Kamhawi, H., & Myers, R. (1995). Experiments with multi-material propellants in ablation-fed pulsed plasma thrusters. In 31st Joint Propulsion Conference and Exhibit (p. 2916).
- Levchenko, I., Keidar, M., Cantrell, J., Wu, Y. L., Kuninaka, H., Bazaka, K., & Xu, S. (2018). Explore space using swarms of tiny satellites.
- Li, Y. H., & Royer, C. (2019). Effect of voltage on second-stage electrodes of dual-stage solid propellant pulsed plasma thruster. Vacuum, 167, 103-112.
- Ling, W. Y. L., Schönherr, T., & Koizumi, H. (2017). Characteristics of a non-volatile liquid propellant in liquid-fed ablative pulsed plasma thrusters. Journal of Applied Physics, 121(7).
- Ling, W. Y. L., Zhang, Z., Tang, H., Liu, X., & Wang, N. (2018). In-plume acceleration of leading-edge ions from a pulsed plasma thruster. Plasma Sources Science and Technology, 27(10), 104002.
- Lobbia, R. B., & Beal, B. E. (2017). Recommended practice for use of Langmuir probes in electric propulsion testing. Journal of Propulsion and Power, 33(3), 566-581.
- Longmier, B. W., Bering, E. A., Carter, M. D., Cassady, L. D., Chancery, W. J., Díaz, F. R. C., ... & Squire, J. P. (2011). Ambipolar ion acceleration in an expanding magnetic nozzle. Plasma Sources Science and Technology, 20(1), 015007.

- Lun, J., & Law, C.H. (2015). Influence of Cathode Shape on Vacuum Arc Thruster Performance and Operation. IEEE Transactions on Plasma Science, 43, 198-208.
- Markusic, T., Spores, R., Markusic, T., & Spores, R. (1997, July). Spectroscopic emission measurements of a pulsed plasma thruster plume. In 33rd Joint Propulsion Conference and Exhibit (p. 2924).
- Markusic, T. E., Polzin, K. A., Choueiri, E. Y., Keidar, M., Boyd, I. D., & Lepsetz, N. (2005). Ablative Z-pinch pulsed plasma thruster. Journal of Propulsion and Power, 21(3), 392-400.
- Mashidori, H., Kakami, A., Muranaka, T., & Tachibana, T. (2006). A coaxial pulsed plasma thruster using chemical propellants. Vacuum, 80(11-12), 1229-1233.
- Mirczak, J. D. (2003). Milli-newton thrust stand for electric propulsion (Doctoral dissertation, Massachusetts Institute of Technology).
- Moeller, T., & Polzin, K. A. (2010). Thrust stand for vertically oriented electric propulsion performance evaluation. Review of Scientific Instruments, 81(11).
- Montag, C., Herdrich, G., & Schönherr, T. (2017, October). Modifications and experimental analysis towards an update of the pulsed plasma thruster PETRUS. In Proceedings of the 35th International Electric Propulsion Conference, Atlanta, GA, USA (pp. 8-12).
- Myers, R. M. (1993, September). Electromagnetic propulsion for spacecraft. In 1993 Aerospace Design Conference (No. NASA-CR-191186). NASA.
- Nawaz, A., Bauder, U., Bohrk, H. K., Herdrich, G., and Auweter-Kurtz, M., "Electrostatic probe and camera measurements for modeling the iMPD SIMP-LEX," Jet propulsion conference, AIAA, 2007.
- Nawaz, A., Albertoni, R., & Auweter-Kurtz, M. (2010). Thrust efficiency optimization of the pulsed plasma thruster SIMP-LEX. Acta Astronautica, 67(3-4), 440-448.
- Northway, P., Aubuchon, C., Mellema, H., Winglee, R., & Johnson, I. (2017). Pulsed plasma thruster gains in specific thrust for CubeSat propulsion. In 53rd AIAA/SAE/ASEE Joint Propulsion Conference (p. 5040).
- Northway, P., Aubuchon, C., Mellema, H., Winglee, R., & Johnson, I. (2017). Pulsed plasma thruster gains in specific thrust for CubeSat propulsion. In 53rd AIAA/SAE/ASEE Joint Propulsion Conference (p. 5040). doi: 10.2514/6.2017-5040
- Ou, Y., Wu, J., Du, X., Zhang, H., & He, Z. (2019). Experimental investigation on characteristics of pulsed plasma thrusters with the propellant samples of modified PTFE filled Si, Al and Al2O3. Vacuum, 165, 163-171.

- Palumbo, D. J., & Guman, W. J. (1976). Effects of propellant and electrode geometry on pulsed ablative plasma thruster performance. Journal of spacecraft and rockets, 13(3), 163-167.
- Pearse, R. W. B., Gaydon, A. G. (1976). The identification of molecular spectra (Vol. 297, p. 293). London: Chapman and Hall.
- Poghosyan, A., & Golkar, A. (2017). CubeSat evolution: Analyzing CubeSat capabilities for conducting science missions. Progress in Aerospace Sciences, 88, 59-83.
- Polat, H. C., Virgili-Llop, J., & Romano, M. (2016). Survey, statistical analysis and classification of launched CubeSat missions with emphasis on the attitude control method. Journal of small satellites, 5(3), 513-530.
- Pottinger, S. J., & Scharlemann, C. A. (2007, Sept). Micro pulsed plasma thruster development. Paper presented at Proceedings of the 30th International Electric Propulsion Conference, Florence, Italy.
- Pottinger, S. J., Krejci, D., & Scharlemann, C. A. (2011). Pulsed plasma thruster performance for miniaturised electrode configurations and low energy operation. Acta Astronautica, 68(11-12), 1996-2004.
- Scharlemann, C., & York, T. (2006, July). Mass flux measurements in the plume of a pulsed plasma thruster. 42nd AIAA/ASME/SAE/ASEE Joint Propulsion Conference & Exhibit (p. 4856). doi: 10.2514/6.2006-4856
- Schönherr, T., Komurasaki, K., & Herdrich, G. (2013). Propellant utilization efficiency in a pulsed plasma thruster. Journal of Propulsion and Power, 29(6), 1478-1487.
- Schönherr, T., Nawaz, A., Herdrich, G., Röser, H. P., & Auweter-Kurtz, M. (2009). Influence of electrode shape on performance of pulsed magnetoplasmadynamic thruster SIMP-LEX. Journal of propulsion and power, 25(2), 380-386.
- Schönherr, T., Nees, F., Arakawa, Y., Komurasaki, K., & Herdrich, G. (2013). Characteristics of plasma properties in an ablative pulsed plasma thruster. Physics of Plasmas, 20(3).
- Smith, M., Donner, A., Knapp, M., Pong, C., Smith, C., Luu, J., ... & Campuzano, B. (2018). On-orbit results and lessons learned from the ASTERIA space telescope mission.
- Solbes, A., Thomassen, K., & Vondra, R. J. (1970). Analysis of solid PTFE pulsed plasma thruster. Journal of Spacecraft and Rockets, 7(12), 1402-1406.
- Solbes, A., & Vondra, R. J. (1973). Performance study of a solid fuel-pulsed electric microthruster. Journal of Spacecraft and Rockets, 10(6), 406-410.

- Spanjers, G. G., Lotspeich, J. S., McFall, K. A., & Spores, R. A. (1998). Propellant losses because of particulate emission in a pulsed plasma thruster. Journal of Propulsion and Power, 14(4), 554-559.
- Tahara, H., Edamitsu, T., & Sugihara, H. (2007, Sept). Performance Characteristics of Electrothermal Pulsed Plasma Thrusters with Insulator-Rod-Arranged Cavities and PTFE-Alternative Propellants. Paper presented at Proceedings of the 30th International Electric Propulsion Conference, Florence, Italy.
- Takegahara, H., Igarashi, M., Kumagai, N., Sato, K., Tamura, K., & Sugiki, M. (2001). Evaluation of pulsed plasma thruster system for μ-lab sat II. 27th IEPC.
- Tang, H., Shi, C., Zhang, X. A., Zhang, Z., & Cheng, J. (2011). Pulsed thrust measurements using electromagnetic calibration techniques. Review of Scientific Instruments, 82(3).
- Thomassen, K. I., & Vondra, R. J. (1972). Exhaust velocity studies of a solid PTFE pulsed plasma thruster. Journal of Spacecraft and Rockets, 9(1), 61-64.
- Turchi, P., Leiweke, R., & Kamhawi, H. (1996). Design of an inductively-driven pulsed plasma thruster. In 32nd Joint Propulsion Conference and Exhibit (p. 2731).
- Wang, W., Liu, F., Wang, X., & Liang, R. (2013). Study on electron temperature in an ablative pulsed plasma thruster by optical emission spectroscopy. Europhysics Letters, 101(5), 55001.
- Wilson, M. J., Bushman, S. S., & Burton, R. L. (1997). A compact thrust stand for pulsed plasma thrusters. IEPC Paper, (97-122).
- Xu, K. G., & Walker, M. L. (2009). High-power, null-type, inverted pendulum thrust stand. Review of Scientific Instruments, 80(5).
- Yang, L., Liu, X., Guo, W., Wu, Z., & Wang, N. (2010, March). Simulation of parallel-plate pulsed plasma Teflon® thruster based on the electromechanical model. In 2010 2nd International Conference on Advanced Computer Control (Vol. 5, pp. 148-151). IEEE.
- Yang, L., Zeng, G., Tang, H., Huang, Y., & Liu, X. (2016). Numerical studies of wall–plasma interactions and ionization phenomena in an ablative pulsed plasma thruster. Physics of Plasmas, 23(7).
- Yang, Z., Ningfei, W., Xiangyang, L., Ling, W., Kan, X., & Zhiwen, W. U. (2020). Experimental investigation on the evolution of plasma properties in the discharge channel of a pulsed plasma thruster. Plasma Science and Technology, 22(6), 065504.
- Zhang, Z., Ren, J., Tang, H., Ling, W. Y. L., & York, T. M. (2017). An ablative pulsed plasma thruster with a segmented anode. Plasma Sources Science and Technology, 27(1), 015004.

- Zhang, S., Wu, Z., Huang, T., Hou, W., Fu, H., & Ling, W. Y. L. (2022). Performance of pulsed plasma thrusters with a non-volatile liquid propellant stored in porous ceramics with different pore diameters. Vacuum, 205, 111448.
- Zhou, Y., Liu, X., Zhang, X., Wu, Z., Xie, K., & Wang, N. (2017, October). Experimental investigation on the ablation mechanism of HTPB propellant PPT. In Proc. 35th Int. Electric Propulsion Conf.. AIAA.